Neuron

Article

Oligodendrocyte mechanotransduction channel TMEM63A regulates myelin sheath geometry

Graphical abstract

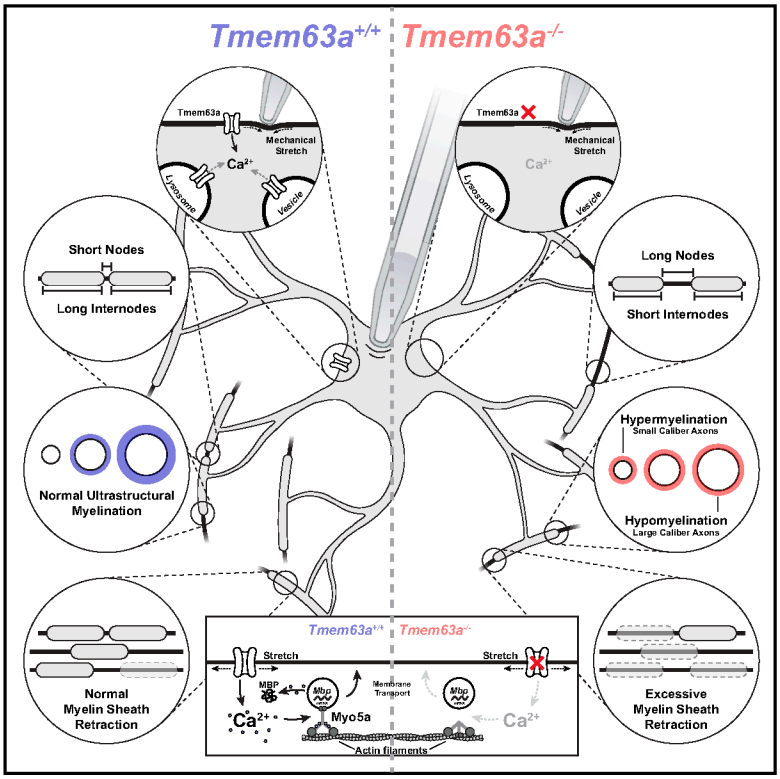

Highlights

- Oligodendrocytes are mechanosensitive via TMEM63A mechanochannels
- TMEM63A converts membrane stretch into Ca^{2+} signals required for myelination
- TMEM63A-mediated Ca^{2+} signaling controls *Mbp* mRNA transport to myelin sheaths
- TMEM63A loss causes hypomyelination, short internodes, and impaired axonal conduction

Authors

Ram R. Dereddi, Minou Djannatian, Frederic Fiore, ..., Stefan G. Lechner, Marc Freichel, Amit Agarwal

Correspondence

amit.agarwal@uni-heidelberg.de

In brief

Dereddi, Djannatian, and colleagues show that oligodendrocytes use mechanical cues to measure axon size. The stretch-activated channel TMEM63A converts membrane tension into calcium signals, which calibrate myelin sheath growth via MYO5A-dependent *Mbp* mRNA transport. Loss of TMEM63A causes mis-sizing of myelin sheaths and hypomyelination linked to transient infantile leukodystrophy.

Dereddi et al., 2026, Neuron *114*, 699–723
February 18, 2026
https://doi.org/10.1016/j.neuron.2025.11.009

CellPress

Neuron

CellPress
OPEN ACCESS

Article

Oligodendrocyte mechanotransduction channel TMEM63A regulates myelin sheath geometry

Ram R. Dereddi,[1,2,11] Minou Djannatian,[3,4,11] Frederic Fiore,[1,12] Darshana Kalita,[1,12] Clement Verkest,[5] Felipe Bodaleo Torres,[1] Wiebke Möbius,[6] Babak Khodaie,[7] Torben Ruhwedel,[6] Khaleel Alhalaseh,[1] Martina Schifferer,[4] Angela Wirth,[9,10] Anthony Hill,[2,8] Roger Ottenheijm,[9,10] Annarita Patrizi,[2,8] Oliver Kann,[2,7] Stefan G. Lechner,[5] Marc Freichel,[9,10] and Amit Agarwal[1,2,13,*]

[1]Chica and Heinz Schaller Research Group, Institute for Anatomy and Cell Biology, Heidelberg University, Heidelberg, Germany
[2]Interdisciplinary Center for Neurosciences, Heidelberg University, Heidelberg, Germany
[3]Department of Neurology, School of Medicine and Health, TUM University Hospital, Technical University of Munich, Munich, Germany
[4]German Center for Neurodegenerative Diseases (DZNE) and Munich Cluster of Systems Neurology (SyNergy), Munich, Germany
[5]Department of Anesthesiology, University Medical Center Hamburg-Eppendorf, Hamburg, Germany
[6]Department of Neurogenetics and Electron Microscopy Unit, Max Planck Institute for Multidisciplinary Sciences, City Campus, Göttingen, Germany
[7]Institute of Physiology and Pathophysiology, Heidelberg University, Heidelberg, Germany
[8]Schaller Research Group, German Cancer Research Center (DKFZ), Heidelberg, Germany
[9]Institute of Pharmacology, Heidelberg University, Heidelberg, Germany
[10]German Centre for Cardiovascular Research (DZHK), Heidelberg, Germany
[11]These authors contributed equally
[12]These authors contributed equally
[13]Lead contact
*Correspondence: amit.agarwal@uni-heidelberg.de
https://doi.org/10.1016/j.neuron.2025.11.009

SUMMARY

Oligodendrocytes, the myelinating cells of the central nervous system, precisely sculpt their insulating membranes to match axon size, ensuring fine-tuned action potential propagation. How oligodendrocytes estimate axon caliber to adapt myelin sheath geometry is unknown. The biochemical measure of axonal size provided by neuregulin 1 for Schwann cells is dispensable in oligodendrocytes, and we reasoned that biophysical cues might instead be required. By combining transcriptomics, *in vivo* optical imaging, and electron microscopy in mouse and zebrafish models, we identified TMEM63A as a key mechanosensitive channel in oligodendrocytes. TMEM63A enabled oligodendrocytes to sense membrane stretch and translate it into Ca^{2+} signals. In the absence of TMEM63A, developmental myelination was severely impaired with shorter and thinner myelin sheaths on large-diameter axons, ectopic myelination of very small-diameter axons, and increased sheath retractions. We propose MYO5A-dependent *Mbp* mRNA targeting to the nascent myelin sheaths as a mechanism linking stretch-activated Ca^{2+} signaling to myelin formation and sheath geometry refinement.

INTRODUCTION

Oligodendrocytes (OLs) are one of the major cells in the mammalian central nervous system (CNS), which electrically insulate the wire-like axonal projections of neurons by multilayered fat-rich membranous sheaths called myelin.[1] However, OLs do not ensheath all axons, and mostly axons larger than 0.2 μm in diameter are myelinated.[2–5] Apart from this size threshold, OLs even match the radial (thickness) and longitudinal (length) dimensions of the myelin sheath to the diameter of the axons they myelinate.[6–9] As a single OL extends several processes and, in turn, myelinates up to 60 axonal segments, where each segment could essentially be of a distinct caliber, the quest for an accurate estimation of axon caliber is magnified up to 60-fold.[10] An inaccurate axon diameter estimation could lead to an insufficient or failed myelination, resulting in improper nerve conduction velocities and neural circuit dysfunction.[2,11,12] Since an optimum wrapping of an axon requires a precise measurement of the geometries of one cell type (neurons) by another cell type (OL), such axon-OL interactions could be considered one of the most intricate cell-cell communications in mammals.

In the peripheral nervous system (PNS), nerves are ensheathed by a distinct myelinating glial cell type called Schwann cells (SCs). Similar to OLs, SCs follow a size threshold (larger than 1 μm in diameter) and match myelin sheath thickness to axonal caliber.[13,14] Evolutionarily, SCs have solved the "axon

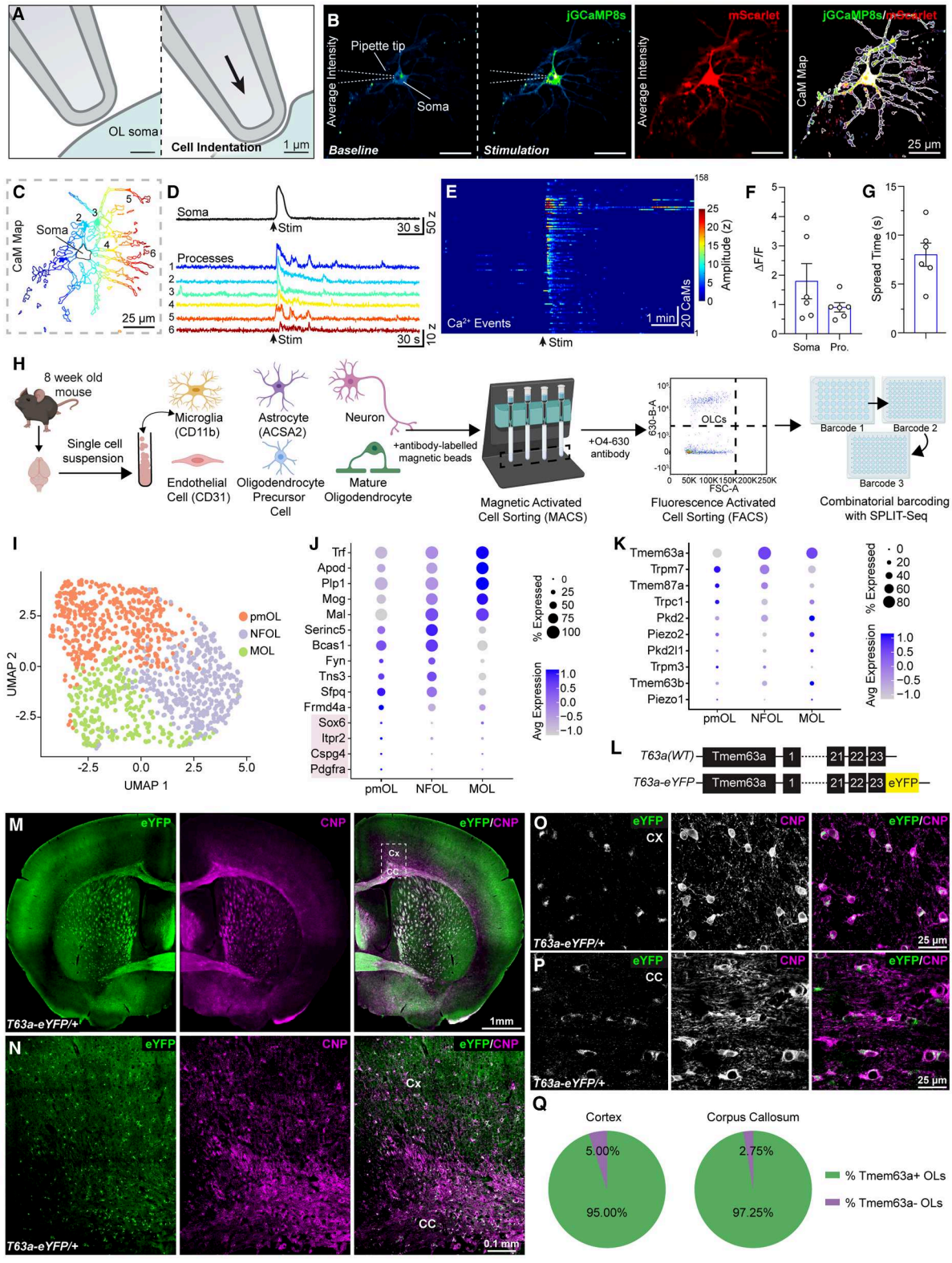

(legend on next page)

caliber size estimation problem'' by using the levels of NRG1-type III, a membrane-bound epidermal growth factor (EGF)-like growth factor, on axons as a biochemical measure.[15] Contrary to the belief, we have shown that NRG1 signaling is largely dispensable for myelination in OLs,[16] and the molecular and cellular basis of axon caliber estimation by OLs remains unknown.

OLs use mechanical cues to regulate several aspects of their development, including proliferation and differentiation. A pioneering study by Rosenberg and colleagues[17] showed that OL precursor cells (OPCs) in culture, when exposed to 20 μm diameter beads, induced their differentiation into mature OLs (MOLs). Remarkably, this effect was restricted to beads between 5 and 100 μm and thus, size-exclusive. Unlike SCs, OLs in culture have an inherent drive to generate membrane extensions[18] and can even wrap inert surfaces such as plastic fibers when they are larger than 0.4 μm.[4] Additionally, OLs in culture could sense the target caliber and deposit longer myelin sheaths on larger diameter fibers.[6] These studies suggest that OLs have an intrinsic machinery to sense the geometries of neighboring structures and might employ mechanical cues to regulate myelination. One study suggests that OL lineage cells (OLCs) could translate mechanical cues by physically linking the plasma membrane with the nuclear membrane through G-actin redistribution and engaging the linker of nucleoskeleton and cytoskeleton complex (LINC) to regulate OL differentiation.[19,20] Another possibility, which is little explored, is that mechanical cues in OLCs could directly activate mechanotransduction channels (MCs) and, in turn, engage a wide variety of signaling effectors ranging from Ca^{2+} signals to transcription factor activation.[21]

MCs are specialized membrane proteins that respond to mechanical forces such as pressure, stretch, or tension. They convert mechanical membrane deformation into biochemical or electrical signals, a process called mechanotransduction.[22] Often, depending on the channel type, the activation of MCs allows the selective passage of cations (Na^+, K^+, and Ca^{2+}) and anions (Cl^-). A recent study showed that MCs such as PIEZO1 and PIEZO2 are expressed in SCs, and cell-specific conditional deletion of *Piezo1/2* affects YAP/TAZ signaling pathways, which is crucial for SC development and myelination.[23,24] Among OLCs, PIEZO1 is expressed in OPCs and helps in sensing the stiffness of the extracellular matrix (ECM). An activation of PIEZO1 inhibits OPC proliferation and differentiation in stiff microenvironments, suggesting that mechanical cues guide progenitor behavior.[25,26] Other MCs that have been implicated in regulating functions of OLs and SCs are TRAAK (primarily localized at nodes of Ranvier),[27] TMEM63A (linked to transient hypomyelinating leukodystrophy in humans),[28] and TRPV4 and TRPM7 (SC differentiation).[29,30]

To date, it is unknown which are the most prominent MCs in OL, which cellular signals these transduce, and whether MCs enable OLs to sense axonal geometries and regulate radial and longitudinal myelin growth. Hence, in this systematic study, we explore whether MCs could be involved in fine-tuning OL myelination. Using a combination of transcriptomic analyses, electrophysiological and imaging studies in transgenic mouse lines, and a zebrafish line, we identified TMEM63A as one of the most prominent MCs expressed by OLs and found that mechanical stimulation of OLs induced its activation, leading to an influx of cations, including Ca^{2+}. In turn, this activation is crucial for axon caliber sensing and fine-tuning myelin sheath geometries. These findings helped to gain insights into the pathophysiology of transient hypomyelinating leukodystrophy-19 (HLD19) (OMIM: 618688) affecting individuals with a loss-of-function mutation in the *Tmem63a* gene.[28,31–34]

RESULTS

Mechanical stimulation of OLs induces Ca^{2+} signals

To probe whether mechanical stimulation of OLs can induce Ca^{2+} signals, we expressed our pseudo-ratiometric genetically encoded Ca^{2+} sensor jGCaMP8s-mScarlet[35] (Caprese) in primary cultures of cortical OLs and measured Ca^{2+} transients evoked by mechanical indentation of the cell soma using two-photon Ca^{2+} imaging (Figure 1A). Mechanical stimulation initiated a local increase in intracellular Ca^{2+} concentration $[Ca^{2+}]_i$ at the point of contact between the stimulation pipette and the soma, which later spread across the entire cell (Figures 1B–1E; Video S1). The amplitude of Ca^{2+} signals in the soma was about 1.8 times (1.79 ± 0.6 s) those in the processes (Figure 1F), and it took about 8 s (8.0 ± 1.19 s) for Ca^{2+} signals to spread from the cell body to the end of the processes (Figure 1G).

Figure 1. Mechanical activation evokes Ca^{2+} signals in OLs, with TMEM63A as a key MC

(A) Mechanical indentation applied to OL soma.

(B) (Left to right) Time-series projection of jGCaMP8s in a cultured OL at baseline and after mechanical stimulation, mScarlet co-expression, and map of calcium microdomains (CaM).

(C and D) Color-coded Ca^{2+} activity map (C) and intensity vs. time traces (D) of six CaMs in OL soma and CaMs.

(E) Duration and amplitude (as *Z* scores) of Ca^{2+} transients in 158 CaMs.

(F and G) Average amplitude (ΔF/F) of Ca^{2+} events (F) and time to spread from soma to distal processes (G). Pro., processes.

(H) Workflow of OL isolation by MACS and FACS and combinatorial barcoding of OLs.

(I) Cell clusters identified from scRNA-seq pre-myelinating OLs (pmOLs; 422 cells, orange), newly formed OLs (NFOLs; 375 cells, purple), and mature OLs (MOLs; 244 cells, green).

(J and K) Expression of key marker genes (J) and MCs (K) in pmOL, NFOL, and MOL. Dot size: percentage of cells expressing a gene; color code: average expression levels.

(L) Wild-type *Tmem63a* (*T63a*) and *Tmem63a-eYFP* knockin (*T63a-eYFP*) reporter allele, where eYFP cDNA was fused to exon 23.

(M–P) Coronal hemi-section of a *T63a-eYFP*/+ mouse brain at P35 immunostained for eYFP and CNP (M), higher magnification of motor cortex (Cx) and corpus callosum (CC) from boxed area (N), and further zoom-in of Cx (O) and CC (P) to show individual cells.

(Q) Proportion of CNP+ OLs co-labeled with eYFP+ cells in Cx and CC.

(D and E) Stim: time of stimulation. Data represent mean ± SEM (F and G) and mean % (Q).

See also Figures S1 and S2, Video S1, and Table S3 (sample sizes and statistical tests).

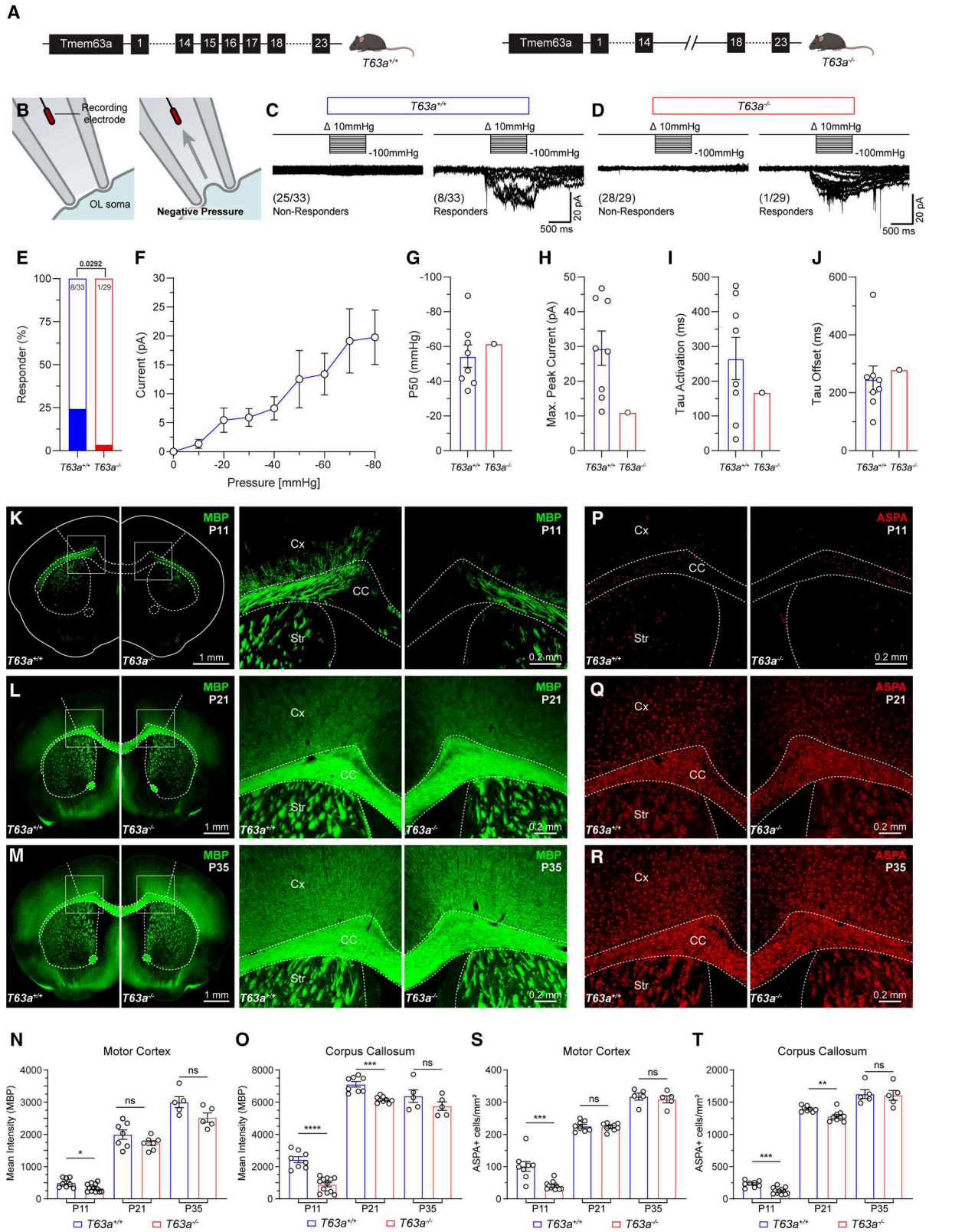

(legend on next page)

As OPCs have been shown to express PIEZO1, one of the best characterized MCs,[25] we reasoned that PIEZO1 activation might be required for the mechanically induced Ca^{2+} signals in OLs. We tested this using the selective PIEZO1 agonist Yoda1, which activates channel opening in the absence of mechanical stimulation. However, Ca^{2+} imaging on OLs with 10 μM bath-applied Yoda1 did not reveal any significant increase in Ca^{2+} transients above baseline (Figures S1A–S1G). We conclude that OLs are mechanically activatable cells, and membrane stretching by mechanical force induces Ca^{2+} signals in a PIEZO1-independent manner.

TMEM63A is the most abundant mechanochannel in OLs

To systematically identify the most abundant MCs expressed in OLs, we developed a magnetic-activated cell sorting (MACS)- and fluorescence-activated cell sorting (FACS)-based approach to isolate a pure population of cortical OLs from adult mouse brain (Figure 1H). Isolated OLs were used to perform SPLiT-seq-based single-cell RNA sequencing (scRNA-seq) in order to capture even low-abundant mRNA transcripts. As expected, almost 100% of the isolated cells could be classified into one of three distinct OLC stages—pre-myelinating OLs (pmOLs), newly formed OLs (NFOLs), and MOLs, while OPCs were practically absent (Figures 1I and 1J). Based on the gene expression analysis of the transcriptome dataset, we identified mechanically activated channels and receptors highly expressed by OLCs (Figures 1K and S1H). Among the top 5 MCs (*Tmem63a*, *Trpm7*, *Tpc1*, *Tmem87a*, and *Pdk2*), *Tmem63a* was the most abundant MC expressed in NFOLs and MOLs (Figure 1K). TMEM63A belongs to the family of mechano- and osmosensitive calcium-permeable cation channels.[36] Of the two other paralogs, *Tmem63b* was expressed at low levels in adult OLs, and *Tmem63c* could not be detected (Figures 1K and S1H). Consistent with the lack of Yoda1 sensitivity in Ca^{2+} imaging experiments, we did not find expression of *Piezo1* in OLs, and *Piezo2*, which is not activated by Yoda1, was only present at low levels in about 20% of OLs (Figure 1K).

To examine the expression of *Tmem63a* in the brain, we used a knockin mouse line, referred to as *T63a-eYFP*/+ in this manuscript (previously described as *OCaR1-eYFP*/+).[37] In this line, the C terminus of the Tmem63a gene is fused with yellow fluorescent protein (eYFP), resulting in endogenous TMEM63A protein tagged with eYFP. This design allowed us to visualize the cellular and subcellular localization of TMEM63A MCs (Figure 1L). Immunohistochemical analysis using an antibody against eYFP on coronal brain sections from 5-week-old *T63a-YFP*/+ mice showed that Tmem63a is abundantly expressed in both the gray and white matter across the entire brain (Figures 1M and 1N). Additional cell-type-specific markers revealed that Tmem63a is expressed by more than 95% of OLs in the gray (motor cortex [Cx]; 95.00% ± 0.8165%) and white (corpus callosum [CC]; 97.25% ± 0.9574%) matter (Figures 1O–1Q), with almost no expression in PDGFRα+ OPCs and premature OLs (BCAS1+/CNP−; Figures S1I–S1K). We found that Tmem63a expression first appeared in pmOLs once they had acquired the myelination fate (BCAS1+/CNP+; Figure S1I). Additionally, a sub-population of cortical Iba1+ microglial cells expressed low levels of TMEM63A (Figures S2A and S2B). However, we did not find any expression of TMEM63A in Sox9+ protoplasmic (cortex) and fibrous (CC) astrocytes or in neurons (NeuN+) (Figures S2C–S2E). Taken together, our data suggest that TMEM63A is one of the most abundant MCs expressed by OLs.

TMEM63A enables OLs to sense mechanical forces

We next asked whether TMEM63A conducts ions in OLs and endows them with mechanical sensitivity. To test this, we performed pressure-clamp recording on primary cortical OLs derived from the brains of Tmem63a null mutant[37] (*T63a*$^{-/-}$) and control (*T63a*$^{+/+}$) mice (Figure 2A). In this assay, mechanotransduction currents are recorded in the cell-attached mode and are evoked by applying negative pressure pulses to the membrane patch inside the patch pipette (Figure 2B).[38] We observed robust mechanically evoked inward currents in 8 of 33 recorded *T63a*$^{+/+}$ cells (∼25%), whereas only 1 of 29 *T63a*$^{-/-}$ cells responded to mechanical stimulation (Figures 2C–2E). The relatively low fraction of mechanosensitive OLs might be due to the composition of our primary cultures, which contained only ∼50% MOLs (Figures 1K, S1J, S1K, S3A, and S3B). In addition, the clustered and sparsely distributed localization of TMEM63A channels within the OL plasma membrane (Figure 6B), together with the restricted membrane area probed by the patch pipette (Figure 2B), implies that some recorded patches may not have contained TMEM63A and would therefore appear unresponsive to mechanical stimulation. A detailed

Figure 2. TMEM63A loss abolishes mechanosensitive currents in OLs and causes severe developmental hypomyelination

(A) Wild-type *Tmem63a* (left; *T63a*$^{+/+}$) and *Tmem63a* null allele with a genetic deletion of exons 15–17 (right; *T63a*$^{-/-}$).

(B) Cell-attached pressure clamp to record current in response to negative pressure on OL membrane.

(C and D) Example traces of currents in response to graded mechanical stimulation ramps (10 mmHg steps) in *T63a*$^{+/+}$ (C) and *T63a*$^{-/-}$ (D) non-responder and responder OLs.

(E) Proportion of *T63a*$^{+/+}$ vs. *T63a*$^{-/-}$ responder and non-responder OLs.

(F) Pressure vs. current relationship for *T63a*$^{+/+}$ responder OLs.

(G–J) Half-maximal activation pressure (G), maximum peak current amplitude (H), activation time constant (I), and inactivation time constants (J) of *T63a*$^{+/+}$ and *T63a*$^{-/-}$ responder OLs.

(K–M) Left: coronal hemi-section (left) and higher magnification of boxed area (right) of a *T63a*$^{+/+}$ (left hemi-section) and *T63a*$^{-/-}$ (right hemi-section) mouse brain immunostained for MBP at P11 (K), P21 (L), and P35 (M). Dotted line separates motor cortex (Cx), corpus callosum (CC), and striatum (Str).

(N and O) Mean fluorescence intensity of MBP in the Cx (N) and CC (O).

(P–R) High-magnification images of boxed areas in (K)–(M) (left) immunostained for ASPA.

(S and T) ASPA+ cells per mm^2 in the Cx (S) and CC (T).

Data represent mean ± SEM. ns, non-significant; $p > 0.05$, *$p < 0.05$, **$p < 0.01$, ***$p < 0.001$, ****$p < 0.0001$.

See also Figures S3 and S5 and Table S3 (sample sizes and statistical tests).

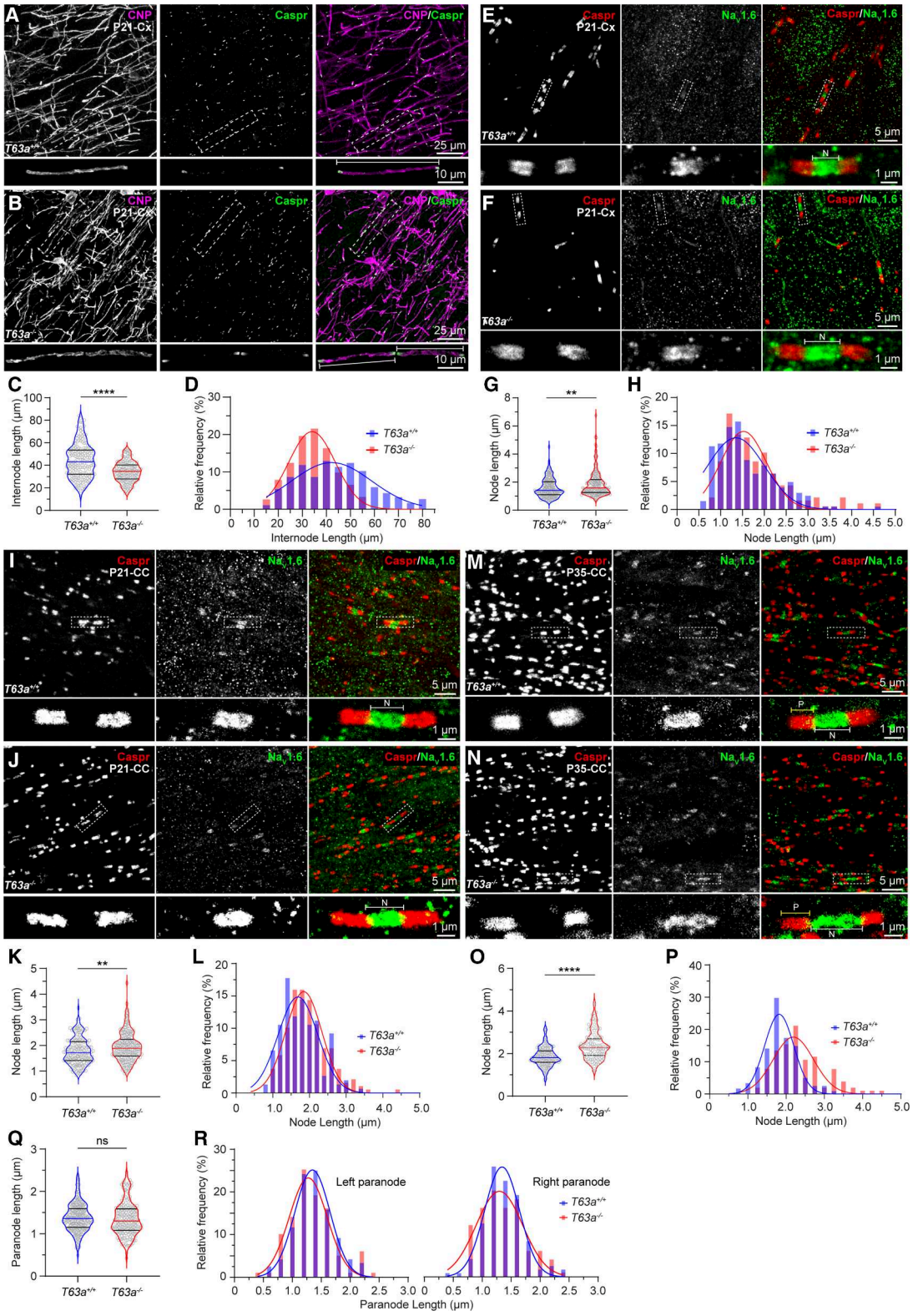

Figure 3. TMEM63A is required for fine-tuning lateral myelin sheath geometry

(A–D) Cx of *T63a*$^{+/+}$ (A) and *T63a*$^{-/-}$ (B) mouse brains at P21 immunostained for CNP and Caspr. Internode lengths in µm (C) and relative frequency distribution (D). (E–H) Cx of *T63a*$^{+/+}$ (E) and *T63a*$^{-/-}$ (F) mouse brains at P21 immunostained for $Na_v1.6$ and Caspr. Node lengths in µm (G) and relative frequency distribution (H).

(legend continued on next page)

characterization of the stretch-evoked currents in OLs revealed that their biophysical properties were similar to the previously reported properties of heterologously expressed TMEM63A,[36] with a mean P50 value of −54.43 ± 6.4 mmHg (i.e., the pressure required for half-maximal activation), maximal peak current amplitudes of 29.49 ± 4.94 pA, and activation and inactivation time constants of 265 ± 172 and 247.3 + 45.59 ms, respectively (Figures 2F–2J). These biophysical properties, together with the observation that OLs from *T63a*$^{-/-}$ mice did not respond to pressure-induced membrane stretch (Figures 2D and 2E), suggest that TMEM63A confers mechanosensitivity to MOLs.

TMEM63A regulates OL maturation and myelination during development

Mechanical stimulation of OLCs in culture has been shown to regulate proliferation and differentiation.[19] To investigate whether TMEM63A in OLs can regulate maturation and myelination, we performed an immunohistochemical analysis on coronal brain sections from *T63a*$^{-/-}$ mutants and *T63a*$^{+/+}$ control mice. We quantified myelination and OL numbers in gray (Cx) and white matter (CC) using antibodies against myelin basic protein (MBP) and aspartoacylase (ASPA) (a marker for MOLs), respectively. We performed analysis at different developmental time points, i.e., when myelination is initiated (postnatal day 11 [P11]) and during the peak period of developmental myelination in the Cx and CC (P21 and P35).[39] At P11, we found a severe hypomyelination in the brain across areas, with a 32% and 64% reduction in MBP intensities in Cx and CC of *T63a*$^{-/-}$ mutants compared with *T63a*$^{+/+}$ controls, respectively (Figures 2K, 2N, and 2O). Cortical myelination in *T63a*$^{-/-}$ mice had mostly recovered by P21, whereas myelin levels in the CC remained slightly reduced (by 13%) (Figures 2L, 2N, and 2O). By P35, both cortical and callosal myelination had fully recovered in *T63a*$^{-/-}$ mutant mice compared with littermate controls (Figures 2M–2O). Similar to myelination levels, the number of ASPA+ OLs in *T63a*$^{-/-}$ mutants at P11 was reduced by 60% in Cx and 47% in CC (Figures 2P, 2S, and 2T). OL numbers in *T63a*$^{-/-}$ mice had mostly recovered by P21 with only a small reduction (8%) in the CC (Figures 2Q, 2S, and 2T) and were indistinguishable from control mice by P35 (Figures 2R–2T).

To determine the cause of the significantly reduced OL numbers in *T63a*$^{-/-}$ mice at P11, we examined both OPC differentiation and cell death. The density of PDGFRα+ OPCs was unchanged, consistent with the lack of *Tmem63a* expression in these cells (Figures S3C–S3E). By contrast, we observed a 26% increase in BCAS1+ pmOLs, suggesting a delay in their maturation into myelinating OLs in the absence of TMEM63A (Figures S3F–S3H). Using caspase-3 immunohistochemistry, we detected no increase in cell death in both Cx and CC of *T63a*$^{-/-}$ mutant mice (Figures S3I–S3K). Together, these findings indicate that the reduced myelination in *T63a*$^{-/-}$ mice primarily results from a delayed maturation of pmOLs into myelinating OLs and that recovery of OL numbers with age progression was linked to myelin recovery.

OLs generate myelin internodes of uniform length in the absence of TMEM63A

While gross myelination recovers with age, subtle deficits in myelin sheath structure might still persist. Since myelin sheath thickness and internode length scale with axon caliber[8,9] and no OL-derived molecular signal has been identified to regulate this matching, we hypothesized that the instructive cue may instead be a mechanical one, with TMEM63A acting as a mechanosensor. To test this hypothesis, we first performed an in-depth analysis of myelin internode and node of Ranvier lengths. We immunostained coronal brain sections from 3-week-old *T63a*$^{+/+}$ control and *T63a*$^{-/-}$ mutant mice with antibodies against the myelin protein CNP (labeling the myelin internode), the axon-OL junction protein Caspr (labeling paranodes), and $Na_V1.6$ voltage-gated sodium channels (labeling nodes), and measured internode lengths as the distance between Caspr+ paranodes adjacent to CNP+ internodes (Figures 3A and 3B). *T63a*$^{-/-}$ OLs generated about 22% shorter internodes (34.35 ± 9.04 μm) than control OLs (44.19 ± 15.01 μm; Figure 3C). While myelin internodes in *T63a*$^{+/+}$ control mice ranged between 15 and 80 μm, and more than 28% of internodes were longer than 50 μm, *T63a*$^{-/-}$ OLs produced relatively uniformly sized internodes, with about 58% of internodes measuring between 30 and 40 μm and only 3% of internodes being longer than 50 μm (Figure 3D).

Next, we examined whether shorter internodes in *T63a*$^{-/-}$ mutants result in longer nodes of Ranvier. We measured the distance between two Caspr+ paranodes adjacent to $Na_V1.6$ sodium channel clusters (Figures 3E and 3F). *T63a*$^{-/-}$ mutants had an average node size of about 1.879 ± 0.90 μm, representing about 18% longer nodal gaps compared with control mice (1.596 ± 0.66 μm; Figure 3G). Furthermore, more than 9% of *T63a*$^{-/-}$ nodes were >3 μm (with 1% in controls), and nodes <1 μm were virtually absent (2% in *T63a*$^{-/-}$ vs. 13% in *T63*$^{+/+}$; Figure 3H). Due to an overcrowding of myelinated axons in CC by P21, we measured nodal lengths but not internode lengths (Figures 3I–3L). Similar to the Cx, we found that *T63a*$^{-/-}$ mutants had 10% longer nodal gaps in the CC (1.953 ± 0.56 μm in *T63a*$^{-/-}$ vs. 1.776 ± 0.51 μm in *T63*$^{+/+}$) and a greater proportion of nodes >3 μm in mutants (4% in *T63a*$^{-/-}$ vs. 0.7% in *T63*$^{+/+}$).

We next examined whether nodal architecture normalizes in parallel with myelin recovery. However, even at P35, nodes remained elongated in *T63a*$^{-/-}$ mice, with mutants exhibiting 28% longer nodal gaps compared with controls (2.373 ± 0.66 μm in *T63a*$^{-/-}$ vs. 1.86 ± 0.45 μm in *T63*$^{+/+}$; Figures 3M–3P). Thus, the

(I–L) CC of *T63a*$^{+/+}$ (I) and *T63a*$^{-/-}$ (J) mice at P21 immunostained for $Na_V1.6$ and Caspr. Node lengths in μm (K) and relative frequency distribution (L).
(M–R) CC of *T63a*$^{+/+}$ (M) and *T63a*$^{-/-}$ (N) mouse brains at P35 immunostained for $Na_V1.6$ and Caspr. Node lengths in μm (O) and relative frequency distribution (P). Paranode lengths in μm (Q) and relative frequency distribution (R).
Higher magnifications of boxed areas show CNP-labeled myelin internodes (A and B) and $Na_V1.6$-labeled nodes (E, F, I, J, M, and N) flanked by Caspr+ paranodes. N, node; P, paranode. Histograms fitted with a Gaussian function. Data represent median and interquartile range (C, G, K, O, and Q). ns, non-significant, $p > 0.05$ (including R), *$p < 0.05$ (including H), **$p < 0.01$ (including L), ****$p < 0.0001$ (including D and P).
See also Figure S5 and Table S3 (sample sizes and statistical tests).

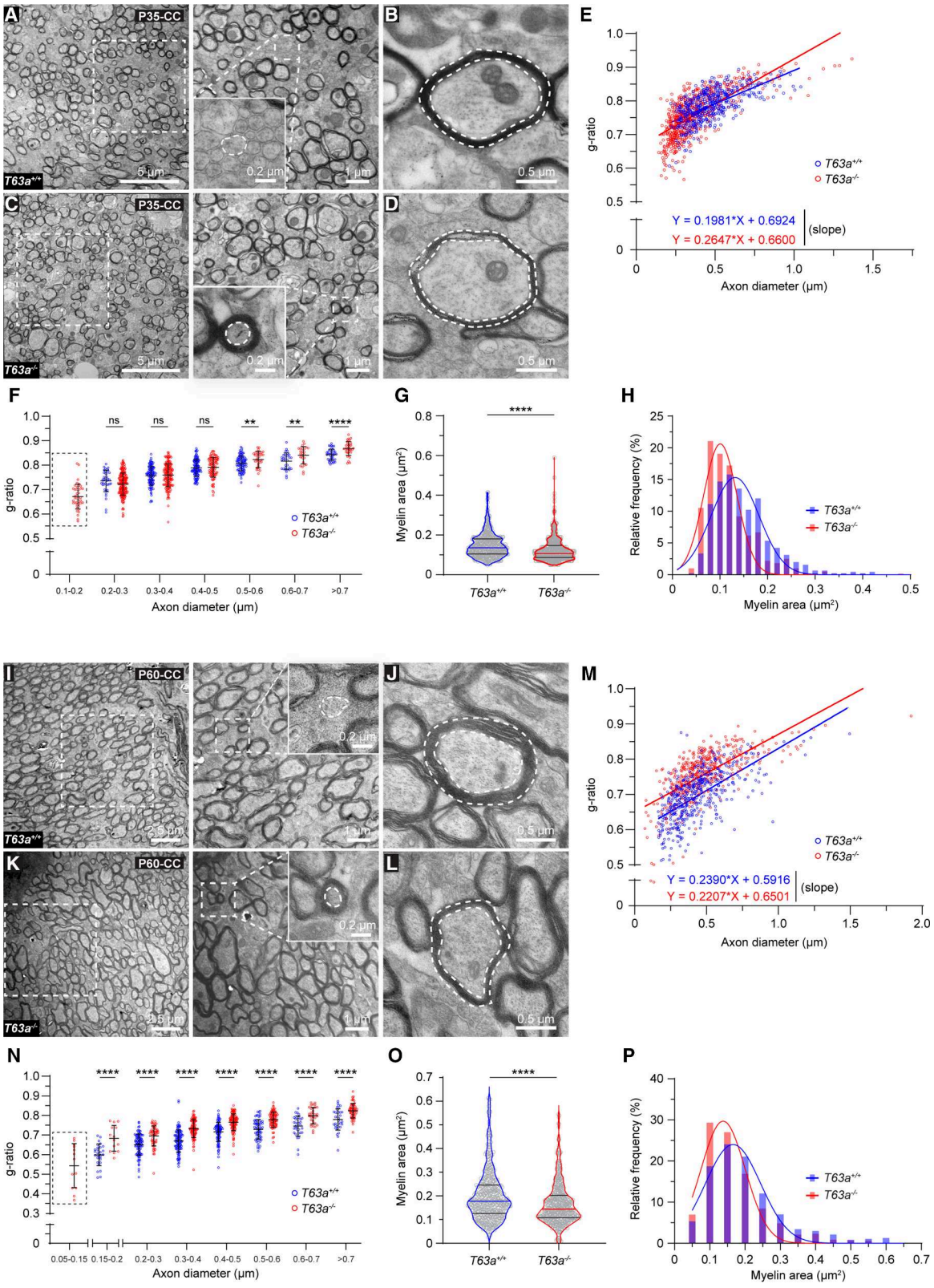

(legend on next page)

elongated nodes persist independently of the transient gross myelin deficit. To further investigate whether these longer nodal gaps in *T63a*$^{-/-}$ mutants were due to an altered paranodal structure, we quantified paranode size by measuring the lengths of Caspr+ segments in flanking paranodes and found no significant difference between *T63a*$^{-/-}$ mutants and *T63*$^{+/+}$ controls (Figures 3Q and 3R). Taken together, our measurements demonstrate that TMEM63A signaling in OLs regulates internodal length, thereby indirectly affecting the size of the nodes, without perturbing the paranodal length.

TMEM63A is required by OLs to match myelin sheath thickness to the axon caliber

To test whether mechanosensing via TMEM63A is also required to adapt the radial myelin sheath growth to the axon caliber, we performed transmission electron microscopy on rostral CC and Cx in 5-week-old *T63a*$^{-/-}$ mutant and *T63*$^{+/+}$ control mice (Figures 4A–4D and S4A–S4D). By this age, myelination and OL numbers had completely recovered in *T63a*$^{-/-}$ mutants (Figures 2K–2T). To study the relationship between axon diameter (D_A) and myelinated fiber diameter, including myelin (D_{A+M}), we determined the ratio of D_A/D_{A+M}, commonly referred to as the g ratio. The g-ratio distribution relative to axon diameter revealed that large-diameter axons ($D_A > 0.5$ μm) had thinner myelin sheaths (g ratio > 0.86) in the CC of *T63a*$^{-/-}$ mice. Conversely, small-diameter axons ($D_A < 0.2$ μm), which normally remain unmyelinated, were myelinated with even thicker myelin sheaths than expected (g ratio < 0.67) (Figures 4E and 4F). Notably, mid-sized axons in mutants and controls (D_A = 0.2–0.5 μm) had no difference in myelin sheath thickness (g ratio 0.76, which is optimum for CC, Figure 4F).

Based on this dichotomous myelination pattern by OLs lacking TMEM63A, i.e., hypomyelination of larger caliber and hypermyelination of small-caliber axons, we hypothesized that *T63a*$^{-/-}$ OLs deposit similar amounts of myelin independent of axon size because they cannot optimally sense axon calibers. Therefore, we quantified the myelin area (i.e., the cross-sectional area of the myelinated fiber minus the area of the axon, delineated by dotted lines) for each axon (Figures 4B and 4D). As expected, control OLs generated myelin sheaths of variable sizes (0.05–0.50 μm^2), whereas *T63a*$^{-/-}$ OLs deposited a relatively uniform amount of myelin (0.05–0.125 μm^2 for 74% of the axons) (Figure 4G). Additionally, controls had twice more axons with a myelin sheath thicker than 0.18 μm^2 (16% in *T63a*$^{-/-}$ vs. 31% in *T63*$^{+/+}$; Figures 4G and 4H). We observed a similar phenotype with ectopic myelination of small-diameter axons (DA < 0.2 μm) and a more uniform myelin in the Cx of *T63a*$^{-/-}$ mice (Figures S4A–S4H).

Furthermore, we extended the g-ratio analysis in the CC of 8-week-old adult mice (Figures 4I–4L), a stage when myelination is mostly complete. In the CC of *T63a*$^{-/-}$ mice, all myelinated axons displayed abnormally thin myelin sheaths, reflected by increased g ratios (>0.73) (Figures 4M and 4N). Again, axons of very small diameter (DA < 0.15 μm) were not only ensheathed but exhibited disproportionately thick myelin (g ratio < 0.55). In addition, myelin deposition by *T63a*$^{-/-}$ OLs appeared less finely tuned to axon caliber, and more than 80% of myelinated axons fell within a narrow myelin area range (0.05–0.2 μm^2; Figures 4O and 4P). Lastly, electron microscopic analysis in the CC at both P35 and P60 revealed no overt structural abnormalities of myelin sheaths or signs of axonal degeneration in *T63a*$^{-/-}$ mutants, suggesting that the aberrant myelination of small-caliber axons is not detrimental to axonal health.

Since small-diameter axons in myelinated regions (CC and Cx) became ectopically myelinated in *T63a*$^{-/-}$ mutants, we asked whether axons in regions that never undergo myelination could get myelinated as well. We focused on cerebellar parallel fibers, thin axons of granule cells that reside in the molecular layer and are permanently unmyelinated.[5] Our histological analyses with axonal (SMI31) and myelin/OL (CNP) markers revealed neither MOLs nor myelin profiles in the cerebellar molecular layer of *T63a*$^{-/-}$ mice, indicating that the loss of TMEM63A does not trigger *de novo* oligodendrogenesis and myelination in normally unmyelinated regions (Figures S4I and S4J). Taken together, these findings identify TMEM63A-dependent mechanosensation as a key determinant of proper scaling of myelin sheath thickness to axon caliber.

TMEM63A regulation of OL maturation and myelination is cell autonomous

To further ensure the cell-autonomous role of TMEM63A in OLs, we performed a few key experiments on mice lacking TMEM63A specifically in OLs. We therefore generated *Tmem63a* floxed mice and crossbred them with OL-specific *MOGi-Cre*[40] mice (*MOGi-Cre;Tmem63afl/fl*; referred to as *OL-T63a*$^{fl/fl}$; Figures S5A–S5D). Although *OL-T63a*$^{fl/fl}$ mice express a red

Figure 4. TMEM63A is required for fine-tuning radial myelin sheath geometry

(A–D) Electron micrographs of CC from *T63a*$^{+/+}$ (A) and *T63a*$^{-/-}$ (C) mice at P35, with higher magnifications of boxed areas to the right. Insets, unmyelinated *T63a*$^{+/+}$ and myelinated *T63a*$^{-/-}$ small-diameter axons (<0.2 μm; white outline). Note the normally myelinated *T63a*$^{+/+}$ (B) vs. hypomyelinated *T63a*$^{-/-}$ large-diameter axons (D). Dashed lines demarcate myelin area.

(E and F) g ratios of individual myelinated axons as a function of axon diameter (E) and binned axon diameter (F, in μm) in the CC at P35. Slopes, $p < 0.0001$ (E). Boxed area (F) indicates the absence of 0.1–0.2 μm myelinated axons in controls.

(G and H) Myelin area of individual myelinated axons (G, in μm^2) and relative frequency distribution (with Gaussian fit, H) in the CC at P35.

(I–L) Electron micrographs of CC from *T63a*$^{+/+}$ (I) and *T63a*$^{-/-}$ (K) mice at P60, with higher magnifications of boxed areas to the right. Insets, unmyelinated *T63a*$^{+/+}$ and myelinated *T63a*$^{-/-}$ small-diameter axons (<0.15 μm; white outline). Note the normally myelinated *T63a*$^{+/+}$ (J) vs. hypomyelinated *T63a*$^{-/-}$ large-diameter axons (L). Dashed lines demarcate myelin area.

(M and N) g ratios of individual myelinated axons as a function of axon diameter (M) and binned axon diameter (N, in μm) in the CC at P60. Slopes, $p = 0.3025$; intercepts, $p < 0.0001$ (M). Boxed area (N) indicates the absence of 0.05–0.15 μm myelinated axons in controls.

(O and P) Myelin area of individual myelinated axons (O, in μm^2) and relative frequency distribution (with Gaussian fit, P) in the CC at P60.

Data represent mean ± SD (F and N) and median with interquartile range (G and O). $^{**}p < 0.01$, $^{****}p < 0.0001$ (including H and P).

See also Figure S4 and Table S3 (sample sizes and statistical tests).

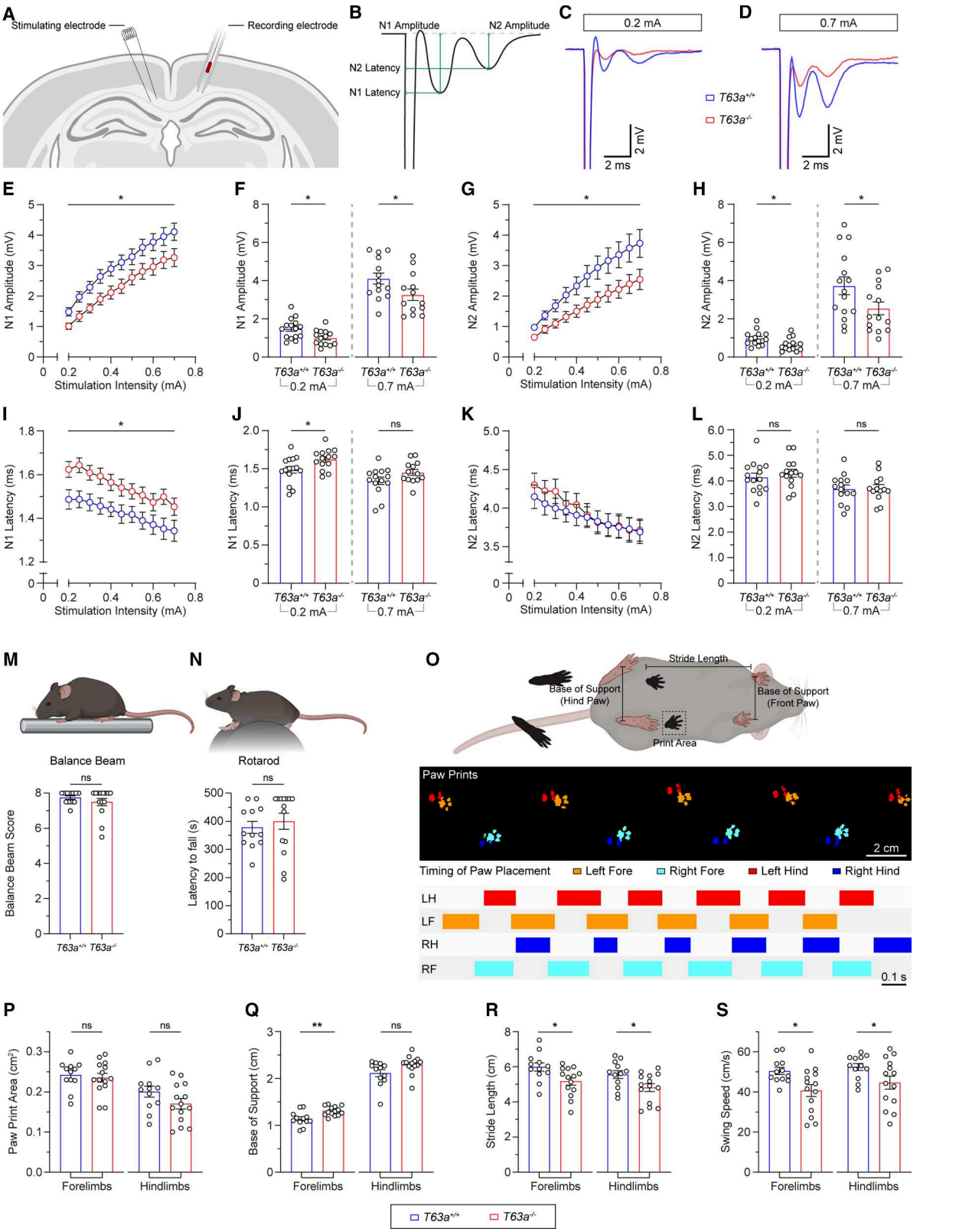

(legend on next page)

fluorescent reporter, tdTomato, in OLs, we did not use it for this study (Figure S5E). Similar to our observation in *T63a*$^{-/-}$ mutants, we found an 11% reduction in OLs in the CC but not in the Cx of 3-week-old *OL-T63a*$^{fl/fl}$ mutant mice (Figures S5F–5H). Additionally, cortical OLs in *OL-T63a*$^{fl/fl}$ mutant mice generated internodes that were 25% shorter (30.77 ± 9.48 μm in *OL-T63a*$^{fl/fl}$ vs. 41.13 ± 14.17 μm in controls) and uniform in size (Figures S5I–S5L). These experiments further support that TMEM63A is a key MC in OLs, and its function directly guides their maturation and shaping of myelin sheath geometry.

Absence of TMEM63A slows down axonal conduction velocity

An ideal organization of myelin geometry—including internodal length, nodal gap, and myelin sheath thickness—is essential for an optimum axonal conduction velocity.[2,11] To test whether structural myelin abnormalities impaired conduction velocity in *T63a*$^{-/-}$ mice, we measured axonal conduction properties. We recorded electrical stimulus-evoked compound action potentials (CAPs) from midline-crossing corpus callosal fibers in acute brain slices of 8-week-old *T63a*$^{-/-}$ mutant and *T63a*$^{+/+}$ control mice (Figure 5A). Biphasic CAP waveforms were observed in all recordings, reflecting fast-conducting myelinated axons (N1) and slower unmyelinated axons (N2).[41] For both components, we quantified peak amplitude and latency to peak in response to graded stimulation (0.2–0.7 mA; Figure 5B). In *T63a*$^{-/-}$ slices, the N1 amplitude was significantly reduced by ∼31.8% at low (0.2 mA) and ∼20.6% at high (0.7 mA) stimulus intensities compared with controls (Figures 5C–5F). Similarly, the N2 amplitude was reduced by ∼33.5% and ∼31.7% at low and high stimulation, respectively (Figures 5G and 5H). Regarding conduction speed, N1 latencies were prolonged by ∼9.2% at low intensity, indicating a slower propagation in myelinated fibers; however, no latency difference was detected at high intensity (Figures 5I and 5J). As expected, N2 latencies of unmyelinated fibers remained unchanged under both stimulus conditions (Figures 5K and 5L). Taken together, these findings suggest distinct mechanisms for the reduced CAP amplitudes in *T63a*$^{-/-}$ mice. For myelinated fibers (N1), a reduced amplitude coupled with an increased latency at low intensities likely reflects a combination of conduction failure in some axons, possibly due to widened nodal gaps and slowed action potential conduction in those fibers that still propagate successfully. For unmyelinated fibers (N2), a reduced amplitude without latency changes may indicate an increased temporal dispersion, consistent with a reduced synchrony across the population. Such dispersion could potentially arise from partial ectopic myelination of normally unmyelinated axons, leading to heterogeneous conduction properties and impaired summation at the population level.

Absence of TMEM63A results in gait and fine motoric impairments

Axons with an impaired myelin geometry and slowed conduction are predicted to exhibit disrupted action potential timing and synchrony,[42] which could lead to deficits in motor coordination.[4,11] We therefore performed a battery of motor behavior tests on adult *T63a*$^{-/-}$ mutant and *T63a*$^{+/+}$ control mice. At first, we performed a beam balance test to evaluate motor coordination and balance. *T63a*$^{-/-}$ mutants (7.5 ± 0.80 score) and controls (7.75 ± 0.33 score) performed this test at similar proficiency (Figure 5M). Next, we performed the rotarod test, and both *T63a*$^{-/-}$ mutants (400.1 ± 106.8 s) and controls (378.3 ± 74.35 s) had a similar latency to fall (i.e., time spent on the rotarod), further suggesting that mutant mice do not have major impairments and can actively engage in motor coordination and balance (Figure 5N). Finally, we performed gait analysis, i.e., description of fine motoric phenotypes including changes in the locomotion characteristics, using the CatWalk system. We analyzed spatial (base of support), temporal (swing speed), and interlimbic coordination (stride length) parameters (Figure 5O). Again, we did not observe deficits in locomotion in *T63a*$^{-/-}$ mutants when we analyzed the paw print area (Figure 5P). However, fine locomotor function analysis revealed a significantly affected gait symmetry (base of support for forelimbs: 1.30 ± 0.09 cm in *T63*$^{-/-}$ vs. 1.13 ± 0.15 cm in *T63*$^{+/+}$), locomotor efficiency (stride length for forelimbs: 5.17 ± 0.82 cm in *T63*$^{-/-}$ vs. 5.98 ± 0.81 cm in *T63*$^{+/+}$ and hind limbs: 4.81 ± 0.83 cm in *T63*$^{-/-}$ vs. 5.55 ± 0.77 cm in *T63*$^{+/+}$), and limbic mobility (swing speed for forelimbs: 44.62 ± 12.03 cm/s in *T63*$^{-/-}$ vs. 52.41 ± 5.98 cm/s in *T63*$^{+/+}$ and hind limbs: 40.65 ± 11.17 cm/s in *T63*$^{-/-}$ vs. 50.41 ± 6.14 cm/s in *T63*$^{+/+}$) in *T63a*$^{-/-}$ mutants compared with littermate controls (Figures 5Q–5S). In summary, the sub-optimal myelin sheath geometry in *T63a*$^{-/-}$ mutant mice is associated with impairments in gait and fine locomotor functions.

Mechanical stimulation of TMEM63A induces Ca^{2+} signals in OLs

To gain a deeper mechanistic insight into how TMEM63A contributes to OL maturation and the regulation of myelin geometry, we examined its subcellular localization and associated Ca^{2+} signaling properties. For this purpose, we analyzed coronal brain

Figure 5. TMEM63A deficiency slows axonal conduction and impairs fine motor behavior

(A) Axonal conduction measurements setup in the CC.

(B) Typical callosal compound action potential (CAP) trace (black) with analyzed CAP parameters (green).

(C and D) CAPs in 8-week-old *T63a*$^{+/+}$ and *T63a*$^{-/-}$ mice in response to a 0.2 mA (C) and 0.7 mA (D) stimulus.

(E–L) N1 (E) and N2 (G) amplitudes and N1 (I) and N2 (K) latencies in response to stimulation intensities between 0.2 and 0.7 mA in *T63a*$^{+/+}$ (blue) and *T63a*$^{-/-}$ (red) mice. N1 (F) and N2 (H) amplitudes and N1 (J) and N2 latencies (L) in response to 0.2 mA (left) and 0.7 mA (right) stimulation.

(M and N) Balance beam test with scores (1: worst and 8: best, M) and rotarod with latency to fall (N) in 2-month-old *T63a*$^{+/+}$ and *T63a*$^{-/-}$ mice.

(O) Features of gait parameters (stride length, base of support, and print area) on the CatWalk test (top) and sequence of right and left paw placements (bottom). Left hind (LH), left front (LF), right hind (RH), and right front (RF) paws. Colored lines, duration of paw placements.

(P–S) Analysis of paw print area (P), base of support (Q), stride length (R), and swing speed (S) of fore- and hindlimbs.

Data represent mean ± SEM. ns, non-significant; $p > 0.05$, $^{*}p < 0.05$, $^{**}p < 0.01$.

See also Table S3 (sample sizes and statistical tests).

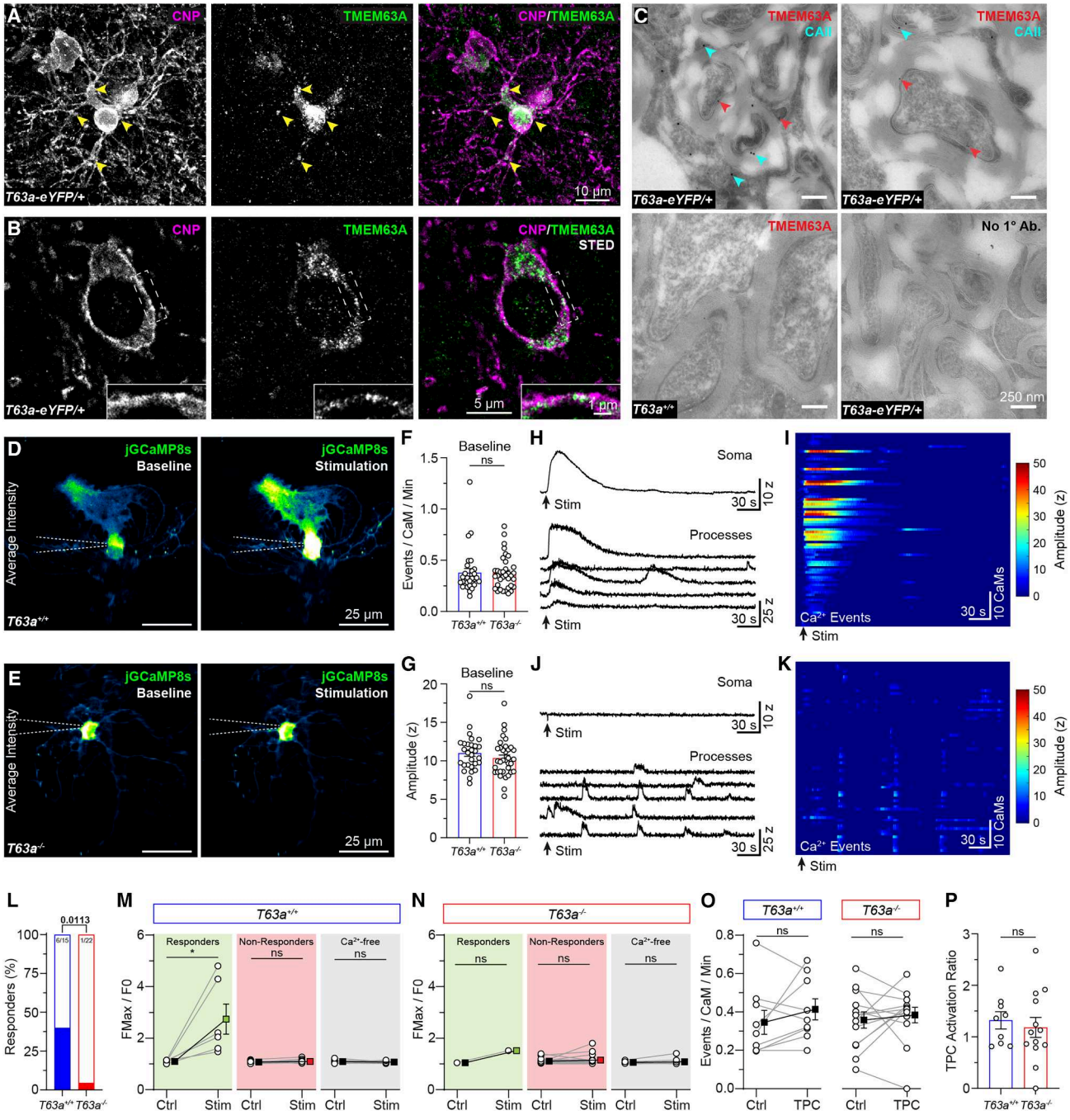

Figure 6. TMEM63A distribution and function in stretch-activated Ca^{2+} signaling in OLs

(A and B) Maximum intensity-projected confocal z stack (A) and single-plane STED (B) image of an OL in *T63a-eYFP*/+ Cx immunostained for CNP (magenta) and eYFP (green). Arrowheads: TMEM63A puncta in the soma and processes. Higher magnification of boxed area in (B) shows TMEM63A puncta on the OL somatic membrane. Note intracellular pool of TMEM63A.

(C) Electron micrographs of optic nerves from *T63a-eYFP*/+ mice (top row). Arrowheads show anti-GFP (TMEM63A, 10 nm gold particles; red) and anti-carbonic anhydrase II (CAII, 15 nm gold particles; cyan) labeling. Primary antibody (anti-GFP, bottom left) and no primary antibody (bottom right) control sections from *T63a*$^{+/+}$ mice.

(D and E) Time-series projection of jGCaMP8s signals in cultured *T63a*$^{+/+}$ (D) and *T63a*$^{-/-}$ (E) OLs at baseline and after mechanical stimulation.

(F and G) Frequency of Ca^{2+} events in each CaM (F) and average amplitude (*Z* score) of Ca^{2+} (G) at baseline.

(H–K) Intensity vs. time traces for soma and five CaMs (H and J) and duration and intensity (*Z* scores) of Ca^{2+} transients in all CaMs (I and K) in *T63a*$^{+/+}$ (H and I) and *T63a*$^{-/-}$ (J and K) mice. Stim, time of stimulation. Note, no response to Stim in *T63a*$^{-/-}$, but baseline Ca^{2+} transients remain intact.

(L) Proportion of *T63a*$^{+/+}$ vs. *T63a*$^{-/-}$ responder and non-responder OLs.

(legend continued on next page)

sections from *T63a-eYFP*/+ reporter mice (Figure 1L) and visualized endogenous TMEM63A stained with anti-eYFP nanobodies by confocal and super-resolution stimulated emission depletion (STED) microscopy. TMEM63A indeed localized at the plasma membrane of the OL soma and primary processes as well as to intracellular compartments (Figures 6A and 6B). Higher-resolution STED imaging further demonstrated that TMEM63A distribution at the plasma membrane is not uniform. Instead, the protein appears in discrete clusters with locally increased density (Figure 6B). To define its localization within the myelin sheath, we performed double immunogold electron microscopy on optic nerve sections from *T63a-eYFP*/+ mice, using antibodies against the OL marker carbonic anhydrase II (CAII) and anti-eYFP. These analyses showed that TMEM63A is enriched at the myelin sheath facing axons and at the outer myelin tongue (Figure 6C, top), while mice lacking eYFP-tagged TMEM63A showed no labeling (Figure 6C, bottom).

Recent studies suggest that an intracellular pool of TMEM63A localizes on secretory vesicles, where it regulates baseline cytosolic Ca^{2+} homeostasis, and that lysosomal TMEM63A can act as an organellar mechanochannel.[37,43] First, to study whether TMEM63A regulates both baseline and mechanical stretch-evoked Ca^{2+} signals in OLs, we expressed jGCaMP8s-mScarlet Ca^{2+} sensors in cultured primary cortical OLs derived from *T63a*$^{-/-}$ mutants and littermate controls and recorded intracellular Ca^{2+} signals using two-photon microscopy (Figures 6D and 6E). We imaged baseline Ca^{2+} signals in OLs for 10 min and rarely saw any somatic Ca^{2+} transients, while most of the Ca^{2+} activity occurred in the processes and was restricted to Ca^{2+} microdomains (CaMs). We did not find any difference in the frequency and amplitude of baseline Ca^{2+} events between *T63a*$^{-/-}$ and *T63a*$^{+/+}$ OLs (Figures 6F and 6G). However, mechanical stimulation (see Figure 1A) induced a robust Ca^{2+} increase in the soma and processes of control but not mutant OLs (Figures 6H–6K). On quantification, we found 40% of *T63a*$^{+/+}$ OLs (6 out of 15), but almost none of the *T63a*$^{-/-}$ OLs (1 out of 22) responded to mechanical stimulation (Figures 6L–6N; Videos S2 and S3). Second, to identify the source of stimulus-induced Ca^{2+} signals (extracellular Ca^{2+} influx vs. release from internal Ca^{2+} stores such as lysosomes), we performed Ca^{2+} imaging in the absence of extracellular Ca^{2+}. In these experiments, mechanical stimulation did not induce any increase in Ca^{2+} transients in control and *T63a*$^{-/-}$ OLs (Figures 6M and 6N), which suggests that mechanical stimulation mediates an influx of Ca^{2+} from outside the cell via TMEM63A MCs at the plasma membrane. Third, to study the role of lysosomal TMEM63A in regulating cytosolic Ca^{2+} signals in OLs, we imaged Ca^{2+} transients while bath-applying TPC2-A1-N (10 μM), which activates the NAADP site of two-pore-channels (TPCs) and induces lysosomal Ca^{2+} release.[44] We did not observe any significant changes in the frequency and amplitude of Ca^{2+} signals in either control or mutant OLs on activation by TPC2-A1-N (Figures 6O and 6P), suggesting that TPC2-mediated Ca^{2+} signaling is not a critical source of lysosomal Ca^{2+} signals in OLs. Thus, we conclude that TMEM63A does not regulate baseline cytosolic Ca^{2+} signals but instead endows OLs with the capability to translate mechanical stretches into Ca^{2+} signals.

TMEM63A fine-tunes myelin sheath growth

As local Ca^{2+} transients in OLs regulate sheath growth and retractions,[45,46] we reasoned TMEM63A-mediated Ca^{2+} signaling might as well participate in fine-tuning myelin dynamics. To follow myelin sheath dynamics, we performed experiments in the optically transparent larval zebrafish model that allows long-term intravital imaging. We generated a Tmem63a null mutant (*T63a*$^{-/-}$) zebrafish line using a CRISPR-Cas9-mediated gene targeting strategy (Figures 7A and S6A) and confirmed the successful generation of *T63a*$^{-/-}$ zebrafish with quantitative real-time PCR on mRNA extracted from whole larvae (Figure S6B). To test whether Tmem63a deficiency in zebrafish recapitulates the delayed myelination seen in mice, we quantified the white-matter volume in the dorsal and ventral spinal cord using mbp:EGFP-CAAX reporter expression and saw a 52% reduction in mutant fish at 3 days post-fertilization (3 dpf) (*T63a*$^{+/+}$: 4,787 ± 2,545 μm^3, *T63a*$^{-/-}$: 2,288 ± 2,142 μm^3; Figures 7B and 7C). A detailed analysis revealed that OLs lacking TMEM63A formed about 44% fewer internodes than control OLs (*T63a*$^{+/+}$: 18.94 ± 3.67 internodes per OL, *T63a*$^{-/-}$: 10.58 ± 4.28 internodes per OL; Figures 7D and 7E). Additionally, we observed shorter internodes in *T63a*$^{+/+}$ compared with *T63a*$^{-/-}$ fish (*T63a*$^{+/+}$: 21.99 ± 11.49 μm, *T63a*$^{-/-}$: 18.95 ± 11.08 μm; Figures 7F–7H). Together, these findings explain why the white matter is reduced in *T63a*$^{-/-}$ zebrafish.

To assess whether Ca^{2+} signaling in OLs is altered *in vivo* during active myelination, we imaged Ca^{2+} activity using GCaMP6s (myrf:KalTA4;UAS:GCaMP6s) in nascent myelin sheaths and in parallel tracked sheath dynamics by sox10:mRFP expression in *T63a*$^{-/-}$ and *T63a*$^{+/+}$ zebrafish at 3–4 dpf. We performed imaging at 0.4 Hz over 20 min in the spinal cord and analyzed the Ca^{2+} events with our machine-learning algorithm CaSCaDe, which automatically detects and quantifies microdomain Ca^{2+} signals.[47] We found that Ca^{2+} transients mainly localized to small subdomains within myelin sheaths (referred to as CaMs). Ca^{2+} events were detected in 78% of *T63a*$^{+/+}$ fish (25/32) but only 50% of *T63a*$^{-/-}$ fish (14/28) during 20 min acquisitions (Figures 7I–7K), and the frequency of these events was strikingly reduced in mutants (#events/500 μm^2—*T63a*$^{+/+}$: 17.14 ± 36.64; *T63a*$^{-/-}$: 0.96 ± 1.87; Figure 7L; Video S4). Additionally, Ca^{2+} event duration was shorter in mutants (*T63a*$^{+/+}$: 57.07 ± 46.75 s, *T63a*$^{-/-}$: 41.90 ± 51.22 s; Figure 7M), whereas

(M and N) Normalized maximum Ca^{2+} amplitude at baseline (Ctrl) and after stimulation (Stim) in *T63a*$^{+/+}$ (M) and *T63a*$^{-/-}$ (N) OLs. Green: responders, red: non-responders, and gray: response in Ca^{2+}-free extracellular recording solution.

(O and P) Frequency of Ca^{2+} events in each CaM before (Ctrl) or after bath application of TPC2-A1-N (TPC, 10 μM, O) and activation ratio (ratio between event frequencies before and after application (P).

Data represent mean ± SEM. ns, non-significant, $p > 0.05$, $^*p < 0.05$.

See also Videos S2 and S3 and Table S3 (sample sizes and statistical tests).

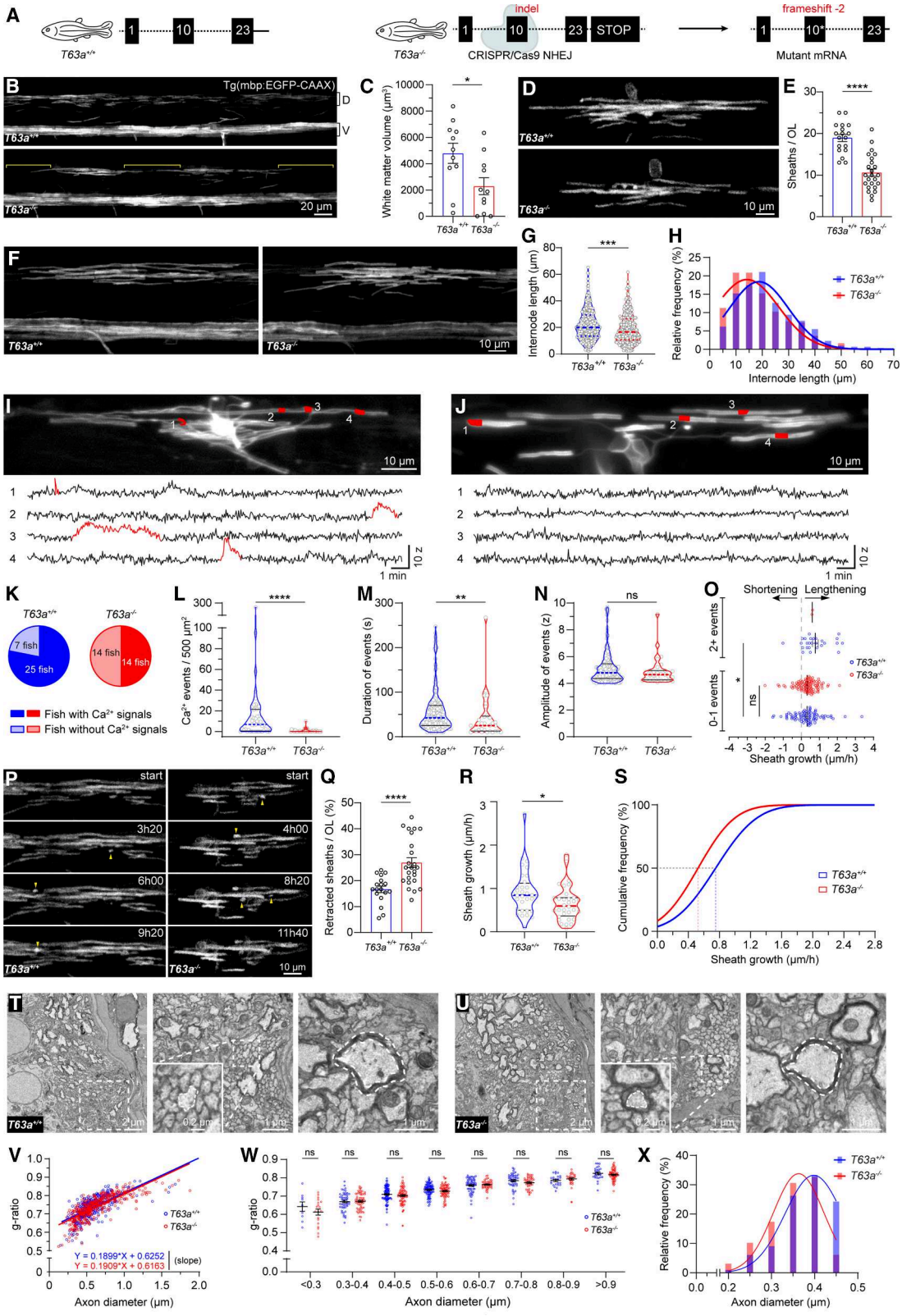

(legend on next page)

amplitude remained unchanged (Figure 7N). These data indicate that TMEM63A mechanochannels make a significant contribution to the occurrence of myelin Ca^{2+} events *in vivo*.

To relate Ca^{2+} activity to growth, internode length was measured from dual-color GCaMP6s and mRFP images acquired immediately before and 3–12 h after Ca^{2+} imaging. The growth dynamics of sheaths with 0–1 Ca^{2+} events over a 20 min period were similar between controls and mutants (*T63a*$^{+/+}$: 0.32 ± 0.79 μm/h; *T63a*$^{-/-}$: 0.33 ± 0.60 μm/h) (Figure 7O). Remarkably, most of the sheaths (92%) with multiple Ca^{2+} events (>2) showed lengthening in *T63a*$^{+/+}$ controls (0.77 ± 0.79 μm/h), whereas such multiple events were rarely observed in *T63a*$^{-/-}$ mutants (Figure 7O). Thus, we conclude that a lower frequency of Ca^{2+} events/sheath in *T63a*$^{-/-}$ fish was associated with fewer fast-growing sheaths and an increased likelihood of shortening/retraction, consistent with prior links between myelin Ca^{2+} signaling and sheath elongation *in vivo*.

To precisely quantify stability and elongation over longer intervals, we imaged myelin sheath dynamics at frequent intervals for >12 h at 3 dpf. *T63a*$^{-/-}$ OLs retracted 62% more sheaths than controls (*T63a*$^{+/+}$: 16.63 ± 5.31; *T63a*$^{-/-}$: 26.95% ± 9.33% retracted sheaths/OL; Figures 7P and 7Q; Videos S5 and S6). In mutants, sheath growth was ∼28% slower (*T63a*$^{-/-}$: 0.66 ± 0.40 μm/h vs. *T63a*$^{+/+}$: 0.92 ± 0.51 μm/h; Figures 7R and 7S; Videos S5 and S6). In addition, OLs lacking TMEM63A more frequently engaged in ectopic ensheathments and wrapped neighboring neuronal soma (64% of *T63a*$^{-/-}$ fish [7/11] vs. 18% of *T63a*$^{+/+}$ [2/11]; Figures S6C–S6F; Video S6). In a nutshell, these observations support a model in which reduced TMEM63A-dependent Ca^{2+} signaling in *T63a*$^{-/-}$ mutants lowers Ca^{2+} event incidence and duration, shifting sheath fate toward shortening and retraction, and reducing net elongation rates during developmental myelination.

Lastly, we studied how Tmem63a deficiency affects myelination when development progresses. At 10 dpf, a late time point during developmental myelination still amenable to intravital imaging, the gross hypomyelination in *T63a*$^{-/-}$ mutants had partially recovered, with white-matter volume still reduced by 33% (*T63a*$^{+/+}$: 85,806 ± 27,322 μm^3, *T63a*$^{-/-}$: 57,542 ± 12,766 μm^3; Figures S6G and S6H). Additionally, *T63a*$^{-/-}$ internodes were on average 12% shorter than *T63a*$^{+/+}$ internodes (*T63a*$^{+/+}$: 23.51 ± 10.52 μm, *T63a*$^{-/-}$: 20.65 ± 10.96 μm; Figures S6I–S6K). To study how the loss of Tmem63a affects myelin ultrastructure, we performed scanning electron microscopy on the spinal cord at 10 dpf. We analyzed the distribution of g ratios in relation to the axon diameter and did not observe a difference in the myelin sheath thickness between control and mutant fish (Figures 7T–7W). Notably, we found that several small-diameter axons (<0.4 μm) in the spinal cord, once thought to be unmyelinated, were myelinated in both *T63a*$^{+/+}$ and *T63a*$^{-/-}$ fish. However, when we analyzed the diameters of the 100 smallest myelinated axons, we found that significantly more axons <0.4 μm were myelinated in *T63a*$^{-/-}$ mutant compared with *T63a*$^{+/+}$ control fish (*T63a*$^{+/+}$: 61.2% vs. *T63a*$^{-/-}$: 42.4%; Figure 7X). These features in part mirror myelination of very small-caliber axons seen in mice lacking TMEM63A (Figures 4F and 4N), reinforcing a conserved role for mechanosensitive Ca^{2+} signaling in growth, targeting, and sheath stability during active myelination.

TMEM63A regulates vesicular transport pathways in OLs

Next, we set out to decipher the molecular pathways regulated by TMEM63A-mediated mechanical force-sensing in OLs. We compared and contrasted the gene expression changes in

Figure 7. TMEM63A-mediated Ca^{2+} signaling in OLs regulates stable myelin deposition and targeted sheath growth in zebrafish

(A) *Tmem63a* wild-type (left; *T63a*$^{+/+}$) and *Tmem63a* zebrafish mutant alleles (middle; *T63a*$^{-/-}$) with resulting mutant mRNA. * Represents premature stop codon in exon 10.

(B) *T63a*$^{+/+}$ and *T63a*$^{-/-}$ zebrafish spinal cords at 3 days post-fertilization (3 dpf) expressing a transgenic myelin reporter. Lateral views with anterior to the left. Yellow brackets indicate hypomyelination in *T63a*$^{-/-}$. D, dorsal; V, ventral white matter.

(C) Ventral and dorsal white-matter volume in ∼640 μm long *T63a*$^{+/+}$ (left) and *T63a*$^{-/-}$ hemi-spinal cords at 3 dpf.

(D) Individual myelinating OL with all their sheaths.

(E) Number of stabilized sheaths per OL.

(F) Internodes in *T63a*$^{+/+}$ and *T63a*$^{-/-}$ spinal cords at 4 dpf.

(G and H) Internode length in μm (G) and relative frequency distribution (H).

(I and J) Time-series projection of GCaMP6s signals and intensity vs. time traces of four CaMs *T63a*$^{+/+}$ (I) and *T63a*$^{-/-}$ (J) OLs during 20 min time-lapse acquisitions at 2.5 s/frame at 3–4 dpf. Region of interests (ROIs) (red) and corresponding traces, with Ca^{2+} events highlighted in red (I). No Ca^{2+} events detected in (J).

(K) Proportion of *T63a*$^{+/+}$ and *T63a*$^{-/-}$ fish exhibiting Ca^{2+} events during 20 min.

(L–N) Number (L), duration (M), and amplitude (N) of Ca^{2+} events per 500 μm^2 myelinated area during 20 min.

(O) Myelin sheath growth binned by 0–1 Ca^{2+} events vs. multiple Ca^{2+} events during 20 min, displayed as shortening (negative growth) and lengthening (positive growth).

(P) *T63a*$^{+/+}$ and *T63a*$^{-/-}$ OLs retracting individual myelin sheaths during an 18-h time-lapse acquisition.

(Q) Number of retracted sheaths.

(R and S) Growth of individual myelin sheaths in μm/h (R) and cumulative Gaussian distribution (S).

(T and U) Electron micrographs of *T63a*$^{+/+}$ (T) and *T63a*$^{-/-}$ (U) zebrafish spinal cords at 10 dpf. Overview images (left) and higher magnification images of small-diameter (middle) and large-diameter axons (right). Insets, small-diameter axons (0.2–0.3 μm; white outline).

(V and W) g ratios of individual myelinated axons as a function of axon diameter (V) and binned axon diameter (W) in *T63a*$^{+/+}$ and *T63a*$^{-/-}$ spinal cords at 10 dpf. Slopes, non-significant; intercepts, $^{**}p < 0.01$ (V).

(X) Relative frequency distribution of axon diameters of the 100 smallest myelinated axons.

Data represent mean ± SEM (C, E, Q, and W) and median with interquartile range (G, L–N, and R). ns, non-significant; $^{*}p < 0.05$ (including S); $^{**}p < 0.01$ (including X), $^{***}p < 0.001$ (including H), $^{****}p < 0.0001$.

See also Figure S6, Videos S4, S5, and S6, and Table S3 (sample sizes and statistical tests).

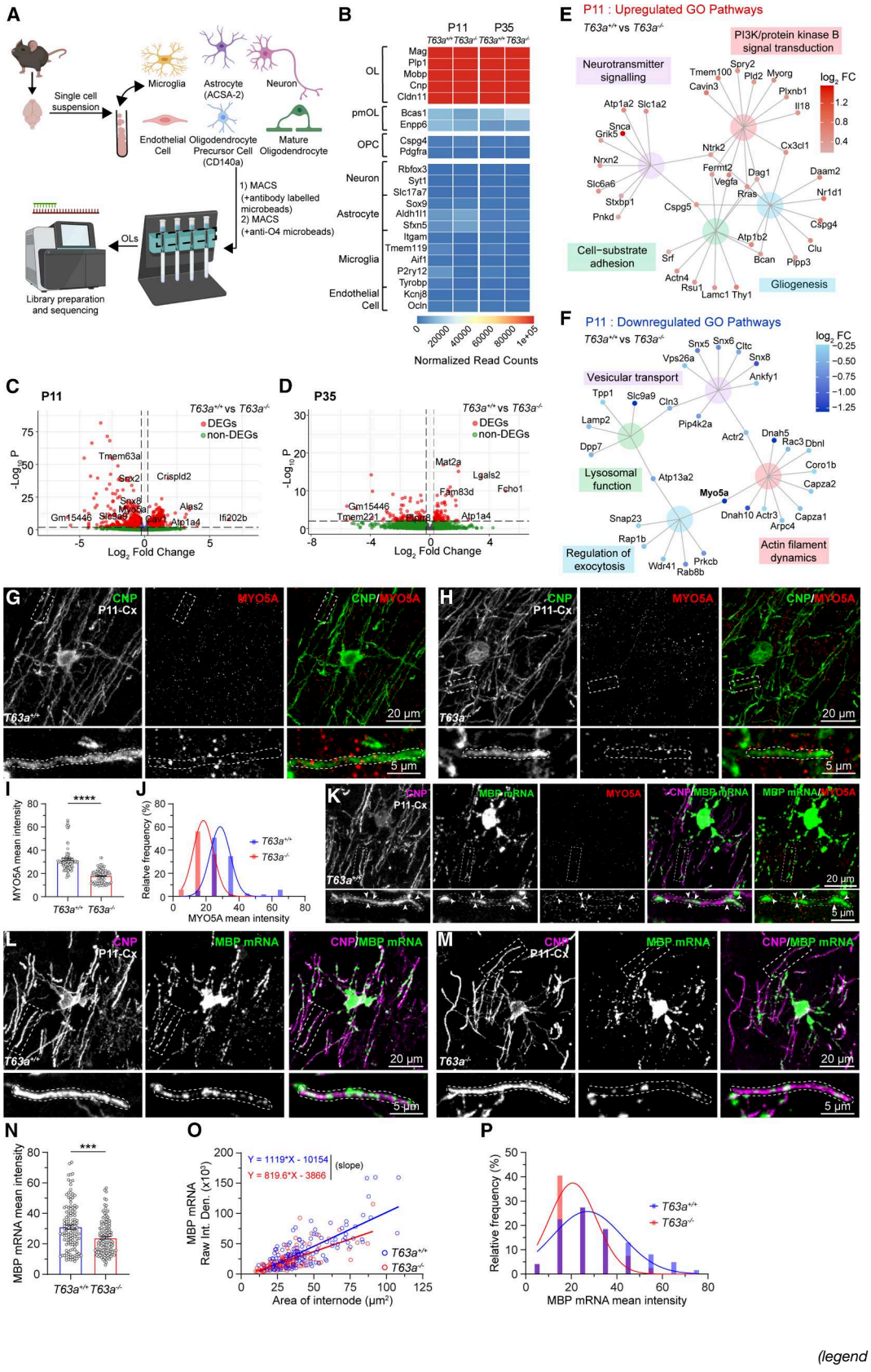

(legend on next page)

mice at two distinct developmental stages—P11, where we had observed hypomyelination, and P35, where gross myelination had recovered in *T63a*$^{-/-}$ mutants (Figure 2). To isolate cortical OLs, we used a MACS-based cell isolation protocol similar to the one in Figure 1, but with minor changes. We performed bulk RNA-seq on total mRNA (for quality controls, see Figure S7) of isolated cells from *T63a*$^{-/-}$ mutant and control mice (Figure 8A). The gene enrichment analysis confirmed that we highly enriched for MOLs, with a small fraction of pmOLs and almost no OPCs, whereas other neural cells, such as neurons, astrocytes, microglial cells, and endothelial cells were practically absent (Figure 8B). As expected, *Tmem63a* transcripts were significantly downregulated in *T63a*$^{-/-}$ OLs at P11 (by 6-fold) and P35 (by 3-fold) (Figures S7H and S7I). While the majority of MCs expressed by OLs remained unchanged, a small number of MCs (KCNKs, belonging to the two-pore-forming potassium channel family) were differentially expressed between *T63a*$^{-/-}$ mutants and controls (Figures S7G–S7I). A detailed bioinformatics analysis of the transcriptomes showed 369 differentially expressed genes (DEGs) at P11, while only 48 DEGs were found between *T63a*$^{-/-}$ mutants and *T63a*$^{+/+}$ controls at P35, with less than a dozen common DEGs between P11 and P35 (Figures 8C and 8D). We sorted the up- and downregulated genes at each developmental stage (P11 and P35) and identified the common cellular pathways regulated by DEGs (Figures 8E, 8F, and S8A–S8D). At P11, most significant DEGs were involved in pathways related to vesicular transport, actin dynamics, regulation of exocytosis, and lysosomal function (Figures 8F and S8B). In contrast to P11, most DEGs at P35 were primarily involved in fatty acid metabolism and cellular catabolic processes (Figures S8C and S8D).

Since most of the DEGs were present at P11, we performed detailed analysis on this age (Figures 8E, 8F, S8A, and S8B). In *T63a*$^{-/-}$ OLs, pathways related to OL development (gliogenesis and phosphatidylinositol 3-kinase [PI3K] signaling), neurotransmitter signaling, and cell adhesion were significantly upregulated. Some of the most prominent upregulated genes included *Bcan*, *Cx3cl1*, *Cspg4*, *Fermt2*, *Lamc1*, *Tmem100*, *Nrxn2*, *Snca*, and *Slc1a2* (Figures 8E, S8A, and S8E). Among these genes, an approximately 25% upregulation of cell adhesion molecules such as *Fermt2* and *Lamc1* could affect axon-OL interactions and myelin sheath formation dynamics, and a 3-fold upregulation of *Snca* (α-synuclein) might impair OL maturation (Figure S8E). To investigate whether TMEM63A deficiency in OLs might cause cellular stress and potentially induce apoptosis, we examined a set of ∼2,000 genes related to "*cellular response to stress*" in OLs at P11 and P35. However, only a small number of genes were slightly up- or downregulated (about 2% at P11 and 0.5% at P35) (Figures S8G–S8J), and none of the DEGs were related to *bona fide* cell stress pathways, indicating that OLs lacking TMEM63A are not under existential stress. Subsequently, we focused on proteins whose activity is regulated by Ca^{2+} signals and identified *Myo5a*, *Cltc*, and *Slc9a9* as the most differentially expressed targets (Figures 8F and S8F). *Myo5a* in particular caught our attention, not only because it is one of the most downregulated genes (by 60%) in *T63a*$^{-/-}$ mutants (Figure S8F) but also because its transport activity is directly regulated by Ca^{2+} and it has previously been implicated in myelination-relevant transport processes.[48,49]

We characterized the expression and localization of MYO5A motor protein in myelinating OLs by immunostaining for MYO5A and CNP (to label individual OLs) (Figures 8G and 8H). We found that MYO5A localized to OL processes and at the internodes, and *T63a*$^{-/-}$ mutants exhibited a 42% reduction in the levels of MYO5A motors (Figure 8I). Approximately 56% of internodes in *T63a*$^{-/-}$ mutants exhibited very low to no detectable MYO5A, defined as mean intensities below 15 (Figure 8J). Since MYO5A has been reported to transport mRNA granules, we examined whether MYO5A could participate in the transport of *Mbp* mRNA to nascent sheaths. MBP is a major myelin protein absolutely required for myelin formation that is locally translated and has recently been shown to regulate myelin sheath length.[50] To test for colocalization, we combined single-molecule fluorescent *in situ* hybridization (smFISH/RNAScope) of *Mbp* mRNA with immunohistochemical labeling of MYO5A motor proteins. We found that, indeed, *Mbp* mRNA clustered and co-localized with MYO5A motors at CNP+ myelin internodes (Figure 8K), implying that MYO5A could possibly transport *Mbp* mRNA during myelination. Lastly, we characterized the distribution of *Mbp* mRNA at *T63a*$^{-/-}$ mutant and *T63a*$^{+/+}$ control internodes by smFISH (Figures 8L and 8M) and found a 23% reduction in *Mbp* mRNA at mutant myelin sheaths (Figure 8N). Furthermore, we observed a linear relationship between the internode area and *Mbp* mRNA and found that larger internodes had the most

Figure 8. Loss of TMEM63A reduces MYO5A levels and disrupts *Mbp* mRNA transport in OLs

(A) OL isolation workflow by MACS and subsequent bulk RNA-seq from mouse cortex.

(B) Cell type-specific marker gene expression in *T63a*$^{+/+}$ and *T63a*$^{-/-}$ cells at P11 and P35.

(C and D) Differentially expressed genes (DEGs) between *T63a*$^{+/+}$ and *T63a*$^{-/-}$ OLs at P11 (C) and P35 (D). An adjusted p value of <0.01 was considered significant.

(E and F) Upregulated (E) and downregulated (F) biological processes associated with selected DEGs in *T63a*$^{-/-}$ OLs at P11. DEGs are grouped by biological processes. Node colors represent $\log_2$ fold expression changes in *T63a*$^{-/-}$ vs. *T63a*$^{+/+}$ OLs.

(G and H) Cortical OL at P11 immunostained for CNP (internodes, green) and MYO5A (red) in *T63a*$^{+/+}$ (G) and *T63a*$^{-/-}$ (H) mice. Insets (dashed boxes) show internodes in higher magnification.

(I and J) Mean MYO5A protein fluorescence intensity (I) and relative frequency distribution (with Gaussian fit, J) across CNP+ internodes.

(K) Cortical *T63a*$^{+/+}$ OL at P11, with *Mbp* mRNA (green) in the vicinity of MYO5A protein (red) in internodes marked with anti-CNP antibody (magenta).

(L and M) Internodes marked with anti-CNP antibody (magenta) and *Mbp* mRNA (green). Insets (dashed boxes) show internodes in higher magnification.

(N–P) Mean *Mbp* mRNA fluorescence intensity across CNP+ internodes (N) and relative frequency distribution (with Gaussian fit, P). Mbp mRNA raw integrated density values (Raw Int Den) vs. internode area (O). Slope, *p < 0.05 (P).

Data represent mean ± SEM (I and N). **p < 0.01 (including P), ***p < 0.001, ****p < 0.0001 (including J).

See also Figures S7 and S8 and Table S3 (sample sizes and statistical tests).

reduction in *Mbp* mRNA expression (Figure 8O), with a narrower range of *Mbp* mRNA intensities in *T63a*$^{-/-}$ mutants (Figure 8P). In conclusion, these results indicate that OLs lacking TMEM63A potentially have an impaired MYO5A-mediated transport of *Mbp* mRNA, which in turn could result in a sub-optimal lateral and radial growth of myelin sheaths.

DISCUSSION

TMEM63A confers mechanosensitivity to OL by coupling membrane stretch to Ca^{2+} signaling that refines myelin architecture. Its loss induces transient but marked developmental hypomyelination, characterized by shortened internodes, thin myelin on large axons, and slowed axonal conduction. We found that TMEM63A-dependent Ca^{2+} transients regulate *Mbp* mRNA delivery to nascent sheaths, ensuring spatially precise myelination.

Mechanically activated channels in OLs

Mechanotransduction has been proposed to play a pivotal role in OPC differentiation and myelin sheath formation. OLs prefer substrates mimicking the physical properties of brain tissue (Young's modulus of 0.1–1 kPa), with substrates beyond this range inhibiting OL differentiation and myelin formation.[20,51] However, little is known about the identity of MCs and their downstream effector signaling pathways. In contrast to its role in SC development and myelination[23] and OPC function,[25,26] our study did not find that PIEZO1 contributes to mechanosensing by OLs. We instead discovered *Tmem63a* as one of the highest expressed MCs in OLs across all developmental stages (young, juvenile, and adult) (Figures 1, S1, and S7).

TMEM63A (also called organellar calcium regulator 1 [OCaR1]) is a highly conserved orthologue of the OSCA (osmotically gated calcium conductance) protein family of ion channels in *Arabidopsis thaliana*.[52] The TMEM63 family is conserved across all animal species, including drosophila, zebrafish, mice, and humans.[28,36] TMEM63A forms a high-threshold, stretch-activated cation channel that can be activated at the plasma membrane or the membrane of intracellular organelles (such as lysosomes and secretory vesicles) by changes in membrane tension or osmotic stress.[36,37,43,53,54] We found that in OLs, TMEM63A localized both at the plasma membrane and on intracellular organelles and formed bona fide mechanosensitive, stretch-activated cation channels. Unlike in pancreatic acinar cells, where a lack of TMEM63A leads to a large increase in cytosolic Ca^{2+} transients,[37] TMEM63A is not required for setting the baseline cytosolic Ca^{2+} homeostasis in OLs (Figures 1, 2, and 6).

Conserved role of TMEM63A in OL maturation and myelination

Mutations in the human *Tmem63a* gene associated with a loss of function in the channel's mechanosensitivity have been causally linked to a hypomyelinating leukodystrophy, clinically referred to as transient infantile hypomyelinating leukodystrophy-19 (HLD19). Children bearing point mutations in *Tmem63a* have severe myelin deficiency as seen on serial magnetic resonance imaging (MRI) scans and exhibit gait deficits, impaired motor function (e.g., ataxia and spasticity), abnormal auditory brainstem evoked potentials, and congenital nystagmus in their first year of life,[28,31–34] initially resembling a severe form of infantile leukodystrophy called Pelizaeus-Merzbacher disease (PMD).[28] However, the later development until adolescence is characterized by an extraordinary recovery of gross myelination in MRI scans and significant improvements in motor deficits, signifying the transient nature of HLD19.

In our study, *T63a*$^{-/-}$ mutant mice carrying loss-of-function *Tmem63a* alleles exhibit a remarkable structural (myelin), electrophysiological (nerve conduction speed), and functional (motor behavior) correlation with HLD19. *T63a*$^{-/-}$ mutant mice showed severe hypomyelination across all brain areas at an early developmental stage (P11), with a significant improvement in both gray and white-matter myelination by P21 and nearly complete recovery by P35 (an age equivalent to adolescence in humans) (Figure 2). Electrophysiological and motor behavior analysis on 8-week-old (age equivalent to young adult human) *T63a*$^{-/-}$ mice showed a reduction in axonal conduction velocity, as well as gait deficits and fine motoric defects as seen in HLD19 individuals (Figure 5). Importantly, gross myelin recovery in *T63a*$^{-/-}$ mutants was not due to a functional compensation by other Tmem63 isoforms (Figures S7G–S7I), as we did not see any compensatory upregulation in Tmem63b and Tmem63c expression in *T63a*$^{-/-}$ OLs. Instead, our data suggest that transient hypomyelination could be primarily due to slower maturation of pmOLs into myelinating OLs. We did not find any evidence for the alternative explanation that *T63a*$^{-/-}$ OLs are under cellular stress, including a lack of activation of canonical endoplasmic reticulum (ER) stress pathways, or undergo apoptosis.[55,56] Instead, our stress-related profiling data revealed a mild boost in adaptive metabolism, with modest increases in genes supporting energy use, lipid synthesis, and survival (*Srebf1*, *Vdac1*, *Lpcat3*, and *Cav1*) (Figures S3 and S8). This suggests that *T63a*$^{-/-}$ OLs rather slow down their maturation and switch to a protective metabolic program, allowing for robust myelination at later stages of development. Our comparative analysis in zebrafish revealed that TMEM63A function in early developmental myelination was conserved even in simple vertebrates (Figures 7 and S6).

Functional consequences of altered myelin sheath geometry

While gross myelination recovers in humans and mice carrying loss-of-function Tmem63a alleles, it remains unclear why fine motor deficits persist. Histological, ultrastructural, and electrophysiological analysis of myelin sheath geometries in *T63a*$^{-/-}$ mice provides a reasonable explanation (Figures 3, 4, and 5). Both the radial and longitudinal dimensions of the myelin sheath were affected in *T63a*$^{-/-}$ mutants, with a reduced myelin thickness of large-diameter axons and shorter myelin sheaths resulting in significantly larger nodal gaps on the axon. Other than gross myelination, these finer deficits in myelin geometry persisted into adulthood in *T63a*$^{-/-}$ mice (Figures 4 and 5). This phenotype was recapitulated in OL-specific null mutant mice, *OL-T63a*$^{fl/fl}$, underscoring a cell-autonomous role of TMEM63A in OLs (Figure S5). What are the functional consequences of this altered sheath geometry? Our data provide strong evidence that longer nodal gaps decrease the efficiency of saltatory

conduction, and a reduced myelin thickness leads to an increased capacitance and decreased resistance, which together slows down action potential propagation in mutants.[2,8,57] Thus, an altered myelin sheath dimension affects the speed and efficiency of neuronal signal transmission and contributes to fine motoric defects as seen in humans[28,31–34] and mice with *Tmem63a* loss of function (Figure 5).

OLs precisely match the length and thickness of individual myelin sheaths to the caliber of the target, even when they encounter plastic fibers, suggesting that they have a cell-autonomous mechanism to sense target diameter.[6] In our study, we found that internodes were more uniform in length and thickness in the absence of TMEM63A, suggesting that myelin sheath geometry was uncoupled from axon diameter (Figures 3 and 4). We suggest that mechanosensation via TMEM63A provides OLs an autonomy to precisely estimate axon caliber. Unlike in mice, the radial component of myelin sheath geometry, i.e., myelin thickness, was unaffected in zebrafish. This is not surprising given that in zebrafish, myelin sheath growth follows axonal growth dynamics rather than absolute size, and myelin is less compact than in mammals.[58] In the mammals, MBP is crucial for myelin sheath stacking and compaction in the CNS, but in the PNS, myelin protein zero (MPZ/P0) substitutes MBP to support compact myelin.[59] As zebrafish CNS myelin contains both MPZ/P0 (∼12%) and MBP (∼8%),[60] such molecular differences suggest that certain TMEM63A-dependent mechanisms involved in mammalian myelin sheath regulation might not entirely operate in zebrafish.

Regulation of myelin targeting

OLs do not require an axonal signal to initiate myelination, and they have an inherent drive to ensheath any target larger than 0.3 μm, including plastic fibers,[4] if they do not encounter any repulsive signals provided by blood vessels, neuronal soma, and dendrites.[61] Therefore, our attention was caught by the ectopic ensheathment of small-caliber axons below 0.2 μm in *T63a*$^{-/-}$ mice and the higher proportion of myelinated small-diameter axons (0.2–0.4 μm) in *T63a*$^{-/-}$ zebrafish, suggesting a reduced axon-size selectivity of *T63a*$^{-/-}$ OLs (Figures 4, 7, and S4). Of note, ectopic ensheathment occurred in the myelinated brain areas (cortex and CC) of *T63a*$^{-/-}$ mutants and not in regions normally devoid of myelin, such as the cerebellar molecular layer. Which factors could be involved in the ectopic ensheathment of small-caliber axons? Our transcriptomic data indicate that loss of *Tmem63a* leads to an upregulation of the adhesion molecules laminin-γ1 (*Lamc1*) and Kindlin2 (*Fermt2*), which enhance OL-axon interactions and promote myelin wrapping through integrin signaling.[62–64] Alternatively, TMEM63A itself might prevent the stabilization of an OL contact with its target if it is activated below threshold. In the absence of TMEM63A, myelination might be initiated in a less specific manner, leading to an ectopic ensheathment. We postulate that once ensheathment is initiated, repulsive signals at the target might enable a later correction, as seen for the transiently ensheathed neuronal somas in zebrafish (Video S5). However, if axons smaller than 0.2 μm lack such repulsive signals, ectopic myelination could be maintained (Figure 4).

Ca^{2+} signaling in myelin sheath regulation

Myelin geometry, including internode length and myelin thickness, can be regulated by several factors, including axon caliber and neuronal activity.[65–71] The underlying cellular processes include cytoskeleton dynamics, exocytosis of myelin protein and lipids, cell adhesion molecules, and transport of RNA granules to the site of myelin sheath formation and expansion.[72–76] Ca^{2+} signaling could be a unifying force that can orchestrate the activity of all these cellular processes during the formation and remodeling of individual myelin sheaths.[35,77,78] Two landmark studies in zebrafish demonstrated that Ca^{2+} signaling at the nascent myelin sheath could regulate myelination dynamics, including the longitudinal growth of myelin and sheath stability.[45,46] One of these studies concluded that a threshold rate of sheath Ca^{2+} transient is required to maintain sheath length.[46] In mice as well, Ca^{2+} transients stabilize the myelin sheath and mediate its compaction during early internode remodeling.[79] Two modes of Ca^{2+} signaling have been proposed to occur during sheath growth—one dependent on neuronal activity and another cell autonomous one generated by the activation of TRPA1[46] and opening of mitochondrial transition pores.[79] A third possibility is that local Ca^{2+} transient could be induced in OLs during membrane stretches while OLs wrap myelin sheaths around axons, a mechanism that remained unexplored until now. We found that mechanical stretch of OL membranes evokes TMEM63A-dependent microdomain Ca^{2+} transients in the soma and processes (Figure 6). Additionally, TMEM63A-mediated Ca^{2+} transients shape myelin growth and sheath stability and contribute to target selection *in vivo*, as seen in the zebrafish spinal cord (Figures 7 and S6). Thereby, our study provides a fundamental mechanism by which mechanosensitive Ca^{2+} signaling regulates myelin dynamics.

Downstream effectors of Ca^{2+} signaling in myelin sheath formation

What could be the downstream effectors of such mechanosensitive Ca^{2+} signaling? TMEM63A-mediated Ca^{2+} signals in pancreatic acinar cells promote exocytosis of zymogen granules.[37] Similarly, in alveolar type 2 lung epithelial cells, a mechanically evoked, TMEM63A- and TMEM63B-mediated cytosolic Ca^{2+} rise is essential for the secretion of surfactant.[53] In the CNS, the addition of myelin membrane requires exocytosis driven by the Ca^{2+}-dependent vesicular SNARE proteins VAMP2/3.[80] VAMP2/3 vesicles transport axon-myelin adhesion proteins to the growing myelin sheath, which promotes membrane wrapping and sheath elongation. Of note, clamping of intracellular Ca^{2+} to low levels by an OL-specific expression plasma membrane Ca^{2+} extrusion pump (CalEx)[77] as well as the OL-specific deletion of VAMP2/3[80] result in a similar deficit in myelin sheath fine-tuning (i.e., short internodes) as the deletion of Tmem63a in OLs. Essentially, TMEM63A activation could be a vital link between Ca^{2+} signaling and vesicular exocytosis during myelination. Indeed, our transcriptomics analysis pulled out three highly downregulated genes—*Myo5a* (myosin-5a), *Cltc1* (clathrin heavy chain), and *Slc9a9* (sodium/hydrogen exchanger 9), which can regulate various aspects of protein sorting, vesicular secretion, and transport pathways in a Ca^{2+}-dependent manner (Figures 8 and S8).[77,81,82] Dysregulation of these vesicle

transport pathways may disrupt signaling cascades that control and fine-tune myelination.

Mechanistically, we investigated MYO5A, an actin-based motor protein involved in intracellular transport, since it is expressed in OLs at all stages of maturation and localizes to microtubules and at the myelin sheath edges.[83] Similar to *T63a*$^{-/-}$ mice, *Myo5a* null mutant mice exhibit hypomyelination at P15 across the entire CNS, including the optic nerve and CC.[83] MYO5A-deficient OLs exhibit shorter processes with reduced branching,[83] similar to our findings in TMEM63A-deficient zebrafish. In humans, loss of MYO5A function associated with Griscelli syndrome type 1 (GS1) leads to diffuse white matter and cerebellar atrophy.[83] MYO5A associates with mRNA in ribonucleoprotein particles present in myelinated peripheral and central axons.[84] Remarkably, MYO5A is involved in a swift localization of RNA granules (within 30 min) after synthesis.[85,86] Thus, one potential mechanism by which MYO5A could regulate myelination is through the transport of mRNA granules for the local synthesis of myelin proteins.[87] Among the major myelin proteins (e.g., PLP1, MBP, CNP, MOG, CLDN11, MOBP, and MAG), which together constitute more than 76% of total myelin protein,[88] MBP is transported as mRNA and locally translated into protein at the site of myelination.[76] We found that MYO5A co-localizes with *Mbp* mRNA, and *Mbp* mRNA at the myelin internodes is significantly reduced in *T63a*$^{-/-}$ mice (Figure 8). We propose that MYO5A might aid in the transport of *Mbp* mRNA granules to the internode and that this process is impaired in the absence of TMEM63A, resulting in a sub-optimal sheath geometry with shorter and thinner myelin sheaths. Moreover, TMEM63A-dependent Ca^{2+} signaling may directly modulate molecular pathways that regulate *Mbp* mRNA translation. These Ca^{2+}-MYO5A-*Mbp* mRNA mechanistic links align with recent findings that MBP levels act as a determinant of myelin sheath length.[50] Alternatively, MYO5A might indirectly affect *Mbp* mRNA localization or translation through the transport of regulatory proteins or vesicles needed for *Mbp* mRNA processing.[48,76]

Model for mechanotransduction in tuning myelin geometry

By integrating our findings, we propose that TMEM63A exerts a dual role in CNS myelination. The intracellular pool of TMEM63A may contribute to OL maturation, consistent with our observation that genes associated with lysosomal acidification and endocytic trafficking (e.g., *Dpp7*, *Lamp2*, *Tpp1*, *Slc9a9*, *Cln3*, *Atp13a2*, and *Cltc*) are transiently downregulated around P11. A reduced activity of these pathways could transiently slow down OL maturation but subsequently allow recovery of gross myelination (Figures 2, 8, and S8). By contrast, TMEM63A localized at the plasma membrane of OLs is crucial for axon caliber sensing and tuning of myelin sheath geometry to axonal size. We propose a model by which membrane stretches perceived by the growing nascent myelin sheath could be stably integrated to fine-tune myelin geometry (Graphical Abstract). When an OL process contacts an axon exceeding 0.3 μm in diameter, mechanotransduction through TMEM63A MCs triggers localized Ca^{2+} influx. Sustained TMEM63A activity maintains Ca^{2+} signals at the growing myelin sheath, which coordinate vesicular trafficking and *Mbp* mRNA recruitment to the wrapping site. This Ca^{2+}-dependent coupling aligns membrane growth with axon caliber, ensuring correct sheath thickness, longitudinal extension, and long-term stability (Graphical Abstract).

Our work identified TMEM63A as a conserved mechanosensor that enables OLs to detect axon caliber and local physical cues essential for myelin growth. *T63a*$^{-/-}$ mice recapitulate defining aspects of human hypomyelinating leukodystrophies and hence provide a robust model to investigate both the cellular mechanisms of myelination failure and the long-term neurological consequences of TMEM63A loss. Defining the molecular pathways downstream of TMEM63A and evaluating early therapeutic interventions to restore myelination during critical developmental windows may offer new avenues for the treatment of these devastating neurological disorders.

RESOURCE AVAILABILITY

Lead contact

Dr. Amit Agarwal (amit.agarwal@uni-heidelberg.de) is the lead contact for reagent and resource sharing.

Materials availability

All published reagents will be made available without restriction upon reasonable request to the lead contact.

Data and code availability

No new code was generated in this study.

ACKNOWLEDGMENTS

We thank Dr. Claudia Pitzer (Interdisciplinary Neurobehavioral Core), support of the mouse behavioral experiments; Drs. Bianka Berki and David Ibberson (Deep Sequencing Core Facility) and NGS core facility at German Cancer Research Center, help in library preparation and RNA sequencing; Dr. Florian Wünnemann, help with single-cell transcriptomics data analysis; Carolin Wüst, Anna von Bachmann, and Irena Dikic, key preliminary experiments and setup of histological data analysis; Dr. Elisa D'Este (Max Planck Institute for Medical Research), help in STED microscopy imaging and data analysis; Dr. Bettina Schmid (German Center for Neurodegenerative Diseases, DZNE), support with zebrafish husbandry; Agata Rhomberg, technical support; Cornelia Niemann and Fereniki Moschogiannaki, support with EM in zebrafish; Dr. David Lyons (University of Edinburgh), sharing knowledge regarding zebrafish Ca^{2+} imaging; and Dr. Ulrich Kriebs, Stefanie Buchholz, and Christin Richter, obtaining floxed Tmem63a mice. We thank Dr. Mikael Simons (Technical University of Munich and DZNE) and Dr. Klaus-Armin Nave (MPI for Multidisciplinary Sciences, Göttingen) for providing generous institutional support for fish and mouse electron microscopy experiments, respectively. We thank Dr. Thomas Kuner, Institute for Anatomy and Cell Biology, for the institutional support. We acknowledge the data storage service SDS@hd supported by the Ministry of Science, Research, and the Arts; Baden-Württemberg; and the German Research Foundation (DFG) through grants INST 35/1314-1FUGG and INST 35/1503-1 FUGG. We acknowledge the following financial support: M.D., DFG (Munich Cluster for Systems Neurology, EXC 2145 SyNergy—ID 390857198); M.F., DFG (TRR152 P21, SFB1328 A21, and FOR5705 P03); S.G.L., DFG (SFB1158 A09); and A.A., Chica and Heinz Schaller Research Foundation, Alliance + Program grant of Health + Life Science Alliance Heidelberg and Mannheim, DFG (FOR2289P8; AG 287/1-1), and SFB1158,A09.

AUTHOR CONTRIBUTIONS

R.R.D. performed all histological experiments, developed the OL isolation protocol, prepared libraries for the bulk RNA sequencing, performed behavior experiments, and analyzed mouse EM data. M.D. generated Tmem63a null mutant zebrafish lines, performed *in vivo* structural and Ca^{2+} imaging, and

analyzed experimental data related to the zebrafish model. F.F. performed mechanical stimulation and Ca^{2+} imaging experiments and contributed to electrophysiology and related data analysis. D.K. prepared SPLiT-seq libraries for the single-cell sequencing and analyzed single-cell and bulk transcriptomics data. C.V. and S.G.L. performed patch-clamp electrophysiology experiments and analysis. B.K. and O.K. performed axonal conduction velocity experiments. F.B.T. contributed to OL culture experiments. K.A. contributed to the analysis of Ca^{2+} imaging data. W.M. and T.R. did sample processing and EM for g-ratio analysis and the immuno-gold labeling EM. M.S. contributed to the sample processing and scanning EM on zebrafish. A.H. and A.P. contributed to the cDNA library preparation and data analysis for bulk RNA sequencing experiments. M.F., R.O., and A.W. provided the Tmem63a null mutant, Tmem63a floxed, and Tmem63a-eYFP mouse lines. A.A. conceived the project, designed the experiments, contributed to the data analysis and interpretation, acquired the funding, and supervised every aspect of the project. A.A. wrote the manuscript with help from the other authors. All authors have read and approved the manuscript.

DECLARATION OF INTERESTS

The authors declare no competing interests.

STAR★METHODS

Detailed methods are provided in the online version of this paper and include the following:

- KEY RESOURCES TABLE
- EXPERIMENTAL MODEL DETAILS
  - Mouse husbandry
  - Transgenic mice
  - Generation of Tmem63a flox mice
  - Zebrafish husbandry
- METHOD DETAILS
  - Generation of Tmem63a knockout zebrafish line
  - Zebrafish RNA isolation and mRNA expression analysis by quantitative PCR
  - Primary oligodendrocyte culture
  - Mechanical stimulation of cultured oligodendrocytes
  - Pharmacological manipulations of cultured oligodendrocytes
  - Calcium imaging and analysis in cultured oligodendrocytes
  - Pressure-clamp electrophysiology
  - Compound action potential recordings and analysis
  - Immunohistochemistry on mouse tissue
  - Epifluorescence and confocal microscopy on fixed tissue
  - Stimulated Emission Depletion (STED) microscopy
  - Single molecule fluorescent in-situ hybridization (smFISH) with immunohistochemistry
  - Zebrafish *in vivo* confocal microscopy
  - Calcium imaging in zebrafish
  - Oligodendrocyte isolation and single-cell library preparation
  - Bulk RNA sequencing of oligodendrocytes
  - Transmission electron microscopy (TEM)
  - Immunoelectron microscopy
  - Scanning electron microscopy
  - Mouse motor behavioral phenotyping
- QUANTIFICATION AND STATISTICAL ANALYSIS
  - Cell number and myelin geometry quantification
  - Myelin g-ratio analysis
  - Analysis of myelin sheath growth and dynamics
  - Analysis of Ca^{2+} imaging in zebrafish
  - Sc-RNA sequencing bioinformatic analysis
  - Bulk RNA-seq bioinformatic analysis
  - Statistical Analysis
  - Data presentation

SUPPLEMENTAL INFORMATION

Supplemental information can be found online at https://doi.org/10.1016/j.neuron.2025.11.009.

Received: February 6, 2025
Revised: September 23, 2025
Accepted: November 10, 2025
Published: January 2, 2026

REFERENCES

1. Nave, K.-A., and Werner, H.B. (2014). Myelination of the Nervous System: Mechanisms and Functions. Annu. Rev. Cell Dev. Biol. *30*, 503–533. https://doi.org/10.1146/annurev-cellbio-100913-013101.
2. Waxman, S.G., and Bennett, M.V.L. (1972). Relative Conduction Velocities of Small Myelinated and Non-myelinated Fibres in the Central Nervous System. Nat. New Biol. *238*, 217–219. https://doi.org/10.1038/newbio238217a0.
3. Remahl, S., and Hildebrand, C. (1982). Changing relation between onset of myelination and axon diameter range in developing feline white matter. J. Neurol. Sci. *54*, 33–45. https://doi.org/10.1016/0022-510x(82)90216-7.
4. Lee, S., Leach, M.K., Redmond, S.A., Chong, S.Y.C., Mellon, S.H., Tuck, S.J., Feng, Z.-Q., Corey, J.M., and Chan, J.R. (2012). A culture system to study oligodendrocyte myelination processes using engineered nanofibers. Nat. Methods *9*, 917–922. https://doi.org/10.1038/nmeth.2105.
5. Goebbels, S., Wieser, G.L., Pieper, A., Spitzer, S., Weege, B., Yan, K., Edgar, J.M., Yagensky, O., Wichert, S.P., Agarwal, A., et al. (2017). A neuronal PI(3,4,5)P3-dependent program of oligodendrocyte precursor recruitment and myelination. Nat. Neurosci. *20*, 10–15. https://doi.org/10.1038/nn.4425.
6. Bechler, M.E., Byrne, L., and ffrench-Constant, C. (2015). CNS Myelin Sheath Lengths Are an Intrinsic Property of Oligodendrocytes. Curr. Biol. *25*, 2411–2416. https://doi.org/10.1016/j.cub.2015.07.056.
7. Murray, J.A., and Blakemore, W.F. (1980). The relationship between internodal length and fibre diameter in the spinal cord of the cat. J. Neurol. Sci. *45*, 29–41. https://doi.org/10.1016/s0022-510x(80)80004-9.
8. Friede, R.L. (1986). Relation between myelin sheath thickness, internode geometry, and sheath resistance. Exp. Neurol. *92*, 234–247. https://doi.org/10.1016/0014-4886(86)90137-8.
9. Fraher, J., and Dockery, P. (1998). A strong myelin thickness-axon size correlation emerges in developing nerves despite independent growth of both parameters. J. Anat. *193*, 195–201. https://doi.org/10.1046/j.1469-7580.1998.19320195.x.
10. Chong, S.Y.C., Rosenberg, S.S., Fancy, S.P.J., Zhao, C., Shen, Y.-A.A., Hahn, A.T., McGee, A.W., Xu, X., Zheng, B., Zhang, L.I., et al. (2012). Neurite outgrowth inhibitor Nogo-A establishes spatial segregation and extent of oligodendrocyte myelination. Proc. Natl. Acad. Sci. USA *109*, 1299–1304. https://doi.org/10.1073/pnas.1113540109.
11. Poggi, G., Boretius, S., Möbius, W., Moschny, N., Baudewig, J., Ruhwedel, T., Hassouna, I., Wieser, G.L., Werner, H.B., Goebbels, S., et al. (2016). Cortical network dysfunction caused by a subtle defect of myelination. Glia *64*, 2025–2040. https://doi.org/10.1002/glia.23039.
12. Bin, J.M., Suminaite, D., Benito-Kwiecinski, S.K., Kegel, L., Rubio-Brotons, M., Early, J.J., Soong, D., Livesey, M.R., Poole, R.J., and Lyons, D.A. (2024). Importin 13-dependent axon diameter growth regulates conduction speeds along myelinated CNS axons. Nat. Commun. *15*, 1790. https://doi.org/10.1038/s41467-024-45908-6.
13. Rushton, W.A.H. (1951). A theory of the effects of fibre size in medullated nerve. J. Physiol. *115*, 101–122. https://doi.org/10.1113/jphysiol.1951.sp004655.
14. Matthews, M.A. (1968). An electron microscopic study of the relationship between axon diameter and the initiation of myelin production in the

peripheral nervous system. Anat. Rec. *161*, 337–351. https://doi.org/10.1002/ar.1091610306.

15. Michailov, G.V., Sereda, M.W., Brinkmann, B.G., Fischer, T.M., Haug, B., Birchmeier, C., Role, L., Lai, C., Schwab, M.H., and Nave, K.-A. (2004). Axonal Neuregulin-1 Regulates Myelin Sheath Thickness. Science *304*, 700–703. https://doi.org/10.1126/science.1095862.
16. Brinkmann, B.G., Agarwal, A., Sereda, M.W., Garratt, A.N., Müller, T., Wende, H., Stassart, R.M., Nawaz, S., Humml, C., Velanac, V., et al. (2008). Neuregulin-1/ErbB Signaling Serves Distinct Functions in Myelination of the Peripheral and Central Nervous System. Neuron *59*, 581–595. https://doi.org/10.1016/j.neuron.2008.06.028.
17. Rosenberg, S.S., Kelland, E.E., Tokar, E., De la Torre, A.R.D.L., and Chan, J.R. (2008). The geometric and spatial constraints of the microenvironment induce oligodendrocyte differentiation. Proc. Natl. Acad. Sci. USA *105*, 14662–14667. https://doi.org/10.1073/pnas.0805640105.
18. Kippert, A., Fitzner, D., Helenius, J., and Simons, M. (2009). Actomyosin contractility controls cell surface area of oligodendrocytes. BMC Cell Biol. *10*, 71. https://doi.org/10.1186/1471-2121-10-71.
19. Hernandez, M., Patzig, J., Mayoral, S.R., Costa, K.D., Chan, J.R., and Casaccia, P. (2016). Mechanostimulation Promotes Nuclear and Epigenetic Changes in Oligodendrocytes. J. Neurosci. *36*, 806–813. https://doi.org/10.1523/jneurosci.2873-15.2016.
20. Jagielska, A., Norman, A.L., Whyte, G., Vliet, K.J.V., Guck, J., and Franklin, R.J.M. (2012). Mechanical Environment Modulates Biological Properties of Oligodendrocyte Progenitor Cells. Stem Cells Dev. *21*, 2905–2914. https://doi.org/10.1089/scd.2012.0189.
21. Pillai, E.K., and Franze, K. (2024). Mechanics in the nervous system: From development to disease. Neuron *112*, 342–361. https://doi.org/10.1016/j.neuron.2023.10.005.
22. Ranade, S.S., Syeda, R., and Patapoutian, A. (2015). Mechanically Activated Ion Channels. Neuron *87*, 1162–1179. https://doi.org/10.1016/j.neuron.2015.08.032.
23. Acheta, J., Bhatia, U., Haley, J., Hong, J., Rich, K., Close, R., Bechler, M.E., Belin, S., and Poitelon, Y. (2022). Piezo channels contribute to the regulation of myelination in Schwann cells. Glia *70*, 2276–2289. https://doi.org/10.1002/glia.24251.
24. Poitelon, Y., Lopez-Anido, C., Catignas, K., Berti, C., Palmisano, M., Williamson, C., Ameroso, D., Abiko, K., Hwang, Y., Gregorieff, A., et al. (2016). YAP and TAZ control peripheral myelination and the expression of laminin receptors in Schwann cells. Nat. Neurosci. *19*, 879–887. https://doi.org/10.1038/nn.4316.
25. Segel, M., Neumann, B., Hill, M.F.E., Weber, I.P., Viscomi, C., Zhao, C., Young, A., Agley, C.C., Thompson, A.J., Gonzalez, G.A., et al. (2019). Niche stiffness underlies the ageing of central nervous system progenitor cells. Nature *573*, 130–134. https://doi.org/10.1038/s41586-019-1484-9.
26. Velasco-Estevez, M., Koch, N., Klejbor, I., Caratis, F., and Rutkowska, A. (2022). Mechanoreceptor Piezo1 Is Downregulated in Multiple Sclerosis Brain and Is Involved in the Maturation and Migration of Oligodendrocytes in vitro. Front. Cell. Neurosci. *16*, 914985. https://doi.org/10.3389/fncel.2022.914985.
27. Brohawn, S.G., Wang, W., Handler, A., Campbell, E.B., Schwarz, J.R., and MacKinnon, R. (2019). The mechanosensitive ion channel TRAAK is localized to the mammalian node of Ranvier. eLife *8*, e50403. https://doi.org/10.7554/elife.50403.
28. Yan, H., Helman, G., Murthy, S.E., Ji, H., Crawford, J., Kubisiak, T., Bent, S.J., Xiao, J., Taft, R.J., Coombs, A., et al. (2019). Heterozygous Variants in the Mechanosensitive Ion Channel TMEM63A Result in Transient Hypomyelination during Infancy. Am. J. Hum. Genet. *105*, 996–1004. https://doi.org/10.1016/j.ajhg.2019.09.011.
29. Feng, X., Takayama, Y., Ohno, N., Kanda, H., Dai, Y., Sokabe, T., and Tominaga, M. (2020). Increased TRPV4 expression in non-myelinating Schwann cells is associated with demyelination after sciatic nerve injury. Commun. Biol. *3*, 716. https://doi.org/10.1038/s42003-020-01444-9.
30. Kim, Y.H., Lee, S., Yang, H., Chun, Y.L., Kim, D., Yeo, S.G., Park, C., Jung, J., and Huh, Y. (2020). Inhibition of transient receptor potential melastatin 7 (TRPM7) protects against Schwann cell trans-dedifferentiation and proliferation during Wallerian degeneration. Anim. Cells Syst. (Seoul) *24*, 189–196. https://doi.org/10.1080/19768354.2020.1804445.
31. Tonduti, D., Mura, E., Masnada, S., Bertini, E., Aiello, C., Zini, D., Parmeggiani, L., Cantalupo, G., Talenti, G., Veggiotti, P., et al. (2021). Spinal cord involvement and paroxysmal events in "Infantile Onset Transient Hypomyelination" due to TMEM63A mutation. J. Hum. Genet. *66*, 1035–1037. https://doi.org/10.1038/s10038-021-00921-1.
32. Fukumura, S., Hiraide, T., Yamamoto, A., Tsuchida, K., Aoto, K., Nakashima, M., and Saitsu, H. (2022). A novel de novo TMEM63A variant in a patient with severe hypomyelination and global developmental delay. Brain Dev. *44*, 178–183. https://doi.org/10.1016/j.braindev.2021.09.006.
33. Yoneno, S., Yamamoto, K., Tabata, K., Shimizu-Motohashi, Y., Tomita, A., Hayashi, T., Maki, H., Sato, N., Inoue, K., Saitsu, H., et al. (2024). A novel heterozygous TMEM63A variant in a familial case with early onset nystagmus, severe hypomyelination, and a favorable adult prognosis. J. Hum. Genet. *69*, 607–611. https://doi.org/10.1038/s10038-024-01268-z.
34. Siori, D., Vlachakis, D., Makrythanasis, P., Traeger-Synodinos, J., Veltra, D., Kampouraki, A., and Chrousos, G.P. (2024). A TMEM63A Nonsense Heterozygous Variant Linked to Infantile Transient Hypomyelinating Leukodystrophy Type 19? Genes *15*, 525. https://doi.org/10.3390/genes15050525.
35. Fiore, F., Alhalaseh, K., Dereddi, R.R., Bodaleo Torres, F.B., Çoban, I., Harb, A., and Agarwal, A. (2023). Norepinephrine regulates calcium signals and fate of oligodendrocyte precursor cells in the mouse cerebral cortex. Nat. Commun. *14*, 8122. https://doi.org/10.1038/s41467-023-43920-w.
36. Murthy, S.E., Dubin, A.E., Whitwam, T., Jojoa-Cruz, S., Cahalan, S.M., Mousavi, S.A.R., Ward, A.B., and Patapoutian, A. (2018). OSCA/TMEM63 are an evolutionarily conserved family of mechanically activated ion channels. eLife *7*, e41844. https://doi.org/10.7554/elife.41844.
37. Tsvilovskyy, V., Ottenheijm, R., Kriebs, U., Schütz, A., Diakopoulos, K.N., Jha, A., Bildl, W., Wirth, A., Böck, J., Jaślan, D., et al. (2024). OCaR1 endows exocytic vesicles with autoregulatory competence by preventing uncontrolled Ca2+ release, exocytosis, and pancreatic tissue damage. J. Clin. Investig. *134*, e169428. https://doi.org/10.1172/jci169428.
38. Verkest, C., Schaefer, I., Nees, T.A., Wang, N., Jegelka, J.M., Taberner, F.J., and Lechner, S.G. (2022). Intrinsically disordered intracellular domains control key features of the mechanically-gated ion channel PIEZO2. Nat. Commun. *13*, 1365. https://doi.org/10.1038/s41467-022-28974-6.
39. Sturrock, R.R. (1980). Myelination of the mouse corpus callosum. Neuropathol. Appl. Neurobiol. *6*, 415–420. https://doi.org/10.1111/j.1365-2990.1980.tb00219.x.
40. Hövelmeyer, N., Hao, Z., Kranidioti, K., Kassiotis, G., Buch, T., Frommer, F., von Hoch, L., Kramer, D., Minichiello, L., Kollias, G., et al. (2005). Apoptosis of oligodendrocytes via Fas and TNF-R1 is a key event in the induction of experimental autoimmune encephalomyelitis. J. Immunol. *175*, 5875–5884. https://doi.org/10.4049/jimmunol.175.9.5875.
41. Colley, B.S., Phillips, L.L., and Reeves, T.M. (2010). The effects of cyclosporin-A on axonal conduction deficits following traumatic brain injury in adult rats. Exp. Neurol. *224*, 241–251. https://doi.org/10.1016/j.expneurol.2010.03.026.
42. Arancibia-Cárcamo, I.L., Ford, M.C., Cossell, L., Ishida, K., Tohyama, K., and Attwell, D. (2017). Node of Ranvier length as a potential regulator of myelinated axon conduction speed. eLife *6*, e23329. https://doi.org/10.7554/elife.23329.
43. Li, K., Guo, Y., Wang, Y., Zhu, R., Chen, W., Cheng, T., Zhang, X., Jia, Y., Liu, T., Zhang, W., et al. (2024). Drosophila TMEM63 and mouse

TMEM63A are lysosomal mechanosensory ion channels. Nat. Cell Biol. *26*, 393–403. https://doi.org/10.1038/s41556-024-01353-7.

44. Gerndt, S., Chen, C.-C., Chao, Y.-K., Yuan, Y., Burgstaller, S., Scotto Rosato, A.S., Krogsaeter, E., Urban, N., Jacob, K., Nguyen, O.N.P., et al. (2020). Agonist-mediated switching of ion selectivity in TPC2 differentially promotes lysosomal function. eLife *9*, e54712. https://doi.org/10.7554/elife.54712.

45. Baraban, M., Koudelka, S., and Lyons, D.A. (2018). Ca^{2+} activity signatures of myelin sheath formation and growth in vivo. Nat. Neurosci. *21*, 19–23. https://doi.org/10.1038/s41593-017-0040-x.

46. Krasnow, A.M., Ford, M.C., Valdivia, L.E., Wilson, S.W., and Attwell, D. (2018). Regulation of developing myelin sheath elongation by oligodendrocyte calcium transients in vivo. Nat. Neurosci. *21*, 24–28. https://doi.org/10.1038/s41593-017-0031-y.

47. Agarwal, A., Wu, P.-H., Hughes, E.G., Fukaya, M., Tischfield, M.A., Langseth, A.J., Wirtz, D., and Bergles, D.E. (2017). Transient Opening of the Mitochondrial Permeability Transition Pore Induces Microdomain Calcium Transients in Astrocyte Processes. Neuron *93*, 587–605.e7. https://doi.org/10.1016/j.neuron.2016.12.034.

48. White, R., Gonsior, C., Krämer-Albers, E.-M., Stöhr, N., Hüttelmaier, S., and Trotter, J. (2008). Activation of oligodendroglial Fyn kinase enhances translation of mRNAs transported in hnRNP A2–dependent RNA granules. J. Cell Biol. *181*, 579–586. https://doi.org/10.1083/jcb.200706164.

49. Shen, M., Zhang, N., Zheng, S., Zhang, W.-B., Zhang, H.-M., Lu, Z., Su, Q.P., Sun, Y., Ye, K., and Li, X.-D. (2016). Calmodulin in complex with the first IQ motif of myosin-5a functions as an intact calcium sensor. Proc. Natl. Acad. Sci. USA *113*, E5812–E5820. https://doi.org/10.1073/pnas.1607702113.

50. Bagheri, H., Friedman, H., Hadwen, A., Jarweh, C., Cooper, E., Oprea, L., Guerrier, C., Khadra, A., Collin, A., Cohen-Adad, J., et al. (2024). Myelin basic protein mRNA levels affect myelin sheath dimensions, architecture, plasticity, and density of resident glial cells. Glia *72*, 1893–1914. https://doi.org/10.1002/glia.24589.

51. Jagielska, A., Lowe, A.L., Makhija, E., Wroblewska, L., Guck, J., Franklin, R.J.M., Shivashankar, G.V., and Van Vliet, K.J.V. (2017). Mechanical Strain Promotes Oligodendrocyte Differentiation by Global Changes of Gene Expression. Front. Cell. Neurosci. *11*, 93. https://doi.org/10.3389/fncel.2017.00093.

52. Freichel, M., Tsvilovskyy, V., Philippaert, K., Schulte, U., and Ottenheijm, R. (2024). The many facets of TMEM63/OCaR proteins as mechanosensitive channels in lysosomes, NAADP signaling and beyond. Cell Calcium *123*, 102942. https://doi.org/10.1016/j.ceca.2024.102942.

53. Chen, G.-L., Li, J.-Y., Chen, X., Liu, J.-W., Zhang, Q., Liu, J.-Y., Wen, J., Wang, N., Lei, M., Wei, J.-P., et al. (2024). Mechanosensitive channels TMEM63A and TMEM63B mediate lung inflation-induced surfactant secretion. J. Clin. Investig. *134*, e174508. https://doi.org/10.1172/jci174508.

54. Zhao, X., Yan, X., Liu, Y., Zhang, P., and Ni, X. (2016). Co-expression of mouse TMEM63A, TMEM63B and TMEM63C confers hyperosmolarity activated ion currents in HEK293 cells. Cell Biochem. Funct. *34*, 238–241. https://doi.org/10.1002/cbf.3185.

55. Walter, P., and Ron, D. (2011). The Unfolded Protein Response: From Stress Pathway to Homeostatic Regulation. Science *334*, 1081–1086. https://doi.org/10.1126/science.1209038.

56. Hetz, C., Zhang, K., and Kaufman, R.J. (2020). Mechanisms, regulation and functions of the unfolded protein response. Nat. Rev. Mol. Cell Biol. *21*, 421–438. https://doi.org/10.1038/s41580-020-0250-z.

57. Cullen, C.L., Pepper, R.E., Clutterbuck, M.T., Pitman, K.A., Oorschot, V., Auderset, L., Tang, A.D., Ramm, G., Emery, B., Rodger, J., et al. (2021). Periaxonal and nodal plasticities modulate action potential conduction in the adult mouse brain. Cell Rep. *34*, 108641. https://doi.org/10.1016/j.celrep.2020.108641.

58. Buckley, C.E., Marguerie, A., Alderton, W.K., and Franklin, R.J.M. (2010). Temporal dynamics of myelination in the zebrafish spinal cord. Glia *58*, 802–812. https://doi.org/10.1002/glia.20964.

59. Raasakka, A., and Kursula, P. (2020). How Does Protein Zero Assemble Compact Myelin? Cells *9*, 1832. https://doi.org/10.3390/cells9081832.

60. Siems, S.B., Jahn, O., Hoodless, L.J., Jung, R.B., Hesse, D., Möbius, W., Czopka, T., and Werner, H.B. (2021). Proteome Profile of Myelin in the Zebrafish Brain. Front. Cell Dev. Biol. *9*, 640169. https://doi.org/10.3389/fcell.2021.640169.

61. Osso, L.A., and Chan, J.R. (2017). Architecting the myelin landscape. Curr. Opin. Neurobiol. *47*, 1–7. https://doi.org/10.1016/j.conb.2017.06.005.

62. Kang, M., and Yao, Y. (2024). Oligodendrocyte-derived laminin-γ1 regulates the blood-brain barrier and CNS myelination in mice. Cell Rep. *43*, 114123. https://doi.org/10.1016/j.celrep.2024.114123.

63. Theodosiou, M., Widmaier, M., Böttcher, R.T., Rognoni, E., Veelders, M., Bharadwaj, M., Lambacher, A., Austen, K., Müller, D.J., Zent, R., et al. (2016). Kindlin-2 cooperates with talin to activate integrins and induces cell spreading by directly binding paxillin. eLife *5*, e10130. https://doi.org/10.7554/elife.10130.

64. Larjava, H., Plow, E.F., and Wu, C. (2008). Kindlins: essential regulators of integrin signalling and cell–matrix adhesion. EMBO Rep. *9*, 1203–1208. https://doi.org/10.1038/embor.2008.202.

65. Almeida, R.G. (2018). The Rules of Attraction in Central Nervous System Myelination. Front. Cell. Neurosci. *12*, 367. https://doi.org/10.3389/fncel.2018.00367.

66. Xin, W., and Chan, J.R. (2020). Myelin plasticity: sculpting circuits in learning and memory. Nat. Rev. Neurosci. *21*, 682–694. https://doi.org/10.1038/s41583-020-00379-8.

67. Gibson, E.M., Purger, D., Mount, C.W., Goldstein, A.K., Lin, G.L., Wood, L.S., Inema, I., Miller, S.E., Bieri, G., Zuchero, J.B., et al. (2014). Neuronal Activity Promotes Oligodendrogenesis and Adaptive Myelination in the Mammalian Brain. Science *344*, 1252304. https://doi.org/10.1126/science.1252304.

68. Ford, M.C., Alexandrova, O., Cossell, L., Stange-Marten, A., Sinclair, J., Kopp-Scheinpflug, C., Pecka, M., Attwell, D., and Grothe, B. (2015). Tuning of Ranvier node and internode properties in myelinated axons to adjust action potential timing. Nat. Commun. *6*, 8073. https://doi.org/10.1038/ncomms9073.

69. Etxeberria, A., Hokanson, K.C., Dao, D.Q., Mayoral, S.R., Mei, F., Redmond, S.A., Ullian, E.M., and Chan, J.R. (2016). Dynamic Modulation of Myelination in Response to Visual Stimuli Alters Optic Nerve Conduction Velocity. J. Neurosci. *36*, 6937–6948. https://doi.org/10.1523/jneurosci.0908-16.2016.

70. Makinodan, M., Rosen, K.M., Ito, S., and Corfas, G. (2012). A Critical Period for Social Experience–Dependent Oligodendrocyte Maturation and Myelination. Science *337*, 1357–1360. https://doi.org/10.1126/science.1220845.

71. Liu, J., Dietz, K., DeLoyht, J.M., Pedre, X., Kelkar, D., Kaur, J., Vialou, V., Lobo, M.K., Dietz, D.M., Nestler, E.J., et al. (2012). Impaired adult myelination in the prefrontal cortex of socially isolated mice. Nat. Neurosci. *15*, 1621–1623. https://doi.org/10.1038/nn.3263.

72. Djannatian, M., Timmler, S., Arends, M., Luckner, M., Weil, M.-T., Alexopoulos, I., Snaidero, N., Schmid, B., Misgeld, T., Möbius, W., et al. (2019). Two adhesive systems cooperatively regulate axon ensheathment and myelin growth in the CNS. Nat. Commun. *10*, 4794. https://doi.org/10.1038/s41467-019-12789-z.

73. Nawaz, S., Kippert, A., Saab, A.S., Werner, H.B., Lang, T., Nave, K.-A., and Simons, M. (2009). Phosphatidylinositol 4,5-Bisphosphate-Dependent Interaction of Myelin Basic Protein with the Plasma Membrane in Oligodendroglial Cells and Its Rapid Perturbation by Elevated Calcium. J. Neurosci. *29*, 4794–4807. https://doi.org/10.1523/jneurosci.3955-08.2009.

74. Zuchero, J.B., Fu, M.-M., Sloan, S.A., Ibrahim, A., Olson, A., Zaremba, A., Dugas, J.C., Wienbar, S., Caprariello, A.V., Kantor, C., et al. (2015). CNS Myelin Wrapping Is Driven by Actin Disassembly. Dev. Cell *34*, 152–167. https://doi.org/10.1016/j.devcel.2015.06.011.

75. Fu, M.-M., McAlear, T.S., Nguyen, H., Oses-Prieto, J.A., Valenzuela, A., Shi, R.D., Perrino, J.J., Huang, T.-T., Burlingame, A.L., Bechstedt, S., et al. (2019). The Golgi Outpost Protein TPPP Nucleates Microtubules and Is Critical for Myelination. Cell *179*, 132–146.e14. https://doi.org/10.1016/j.cell.2019.08.025.

76. Müller, C., Bauer, N.M., Schäfer, I., and White, R. (2013). Making myelin basic protein -from mRNA transport to localized translation. Front. Cell. Neurosci. *7*, 169. https://doi.org/10.3389/fncel.2013.00169.

77. Iyer, M., Kantarci, H., Cooper, M.H., Ambiel, N., Novak, S.W., Andrade, L.R., Lam, M., Jones, G., Münch, A.E., Yu, X., et al. (2024). Oligodendrocyte calcium signaling promotes actin-dependent myelin sheath extension. Nat. Commun. *15*, 265. https://doi.org/10.1038/s41467-023-44238-3.

78. Lu, T.-Y., Hanumaihgari, P., Hsu, E.T., Agarwal, A., Kawaguchi, R., Calabresi, P.A., and Bergles, D.E. (2023). Norepinephrine modulates calcium dynamics in cortical oligodendrocyte precursor cells promoting proliferation during arousal in mice. Nat. Neurosci. *26*, 1739–1750. https://doi.org/10.1038/s41593-023-01426-0.

79. Battefeld, A., Popovic, M.A., de Vries, S.I., and Kole, M.H.P. (2019). High-Frequency Microdomain Ca2+ Transients and Waves during Early Myelin Internode Remodeling. Cell Rep. *26*, 182–191.e5. https://doi.org/10.1016/j.celrep.2018.12.039.

80. Lam, M., Takeo, K., Almeida, R.G., Cooper, M.H., Wu, K., Iyer, M., Kantarci, H., and Zuchero, J.B. (2022). CNS myelination requires VAMP2/3-mediated membrane expansion in oligodendrocytes. Nat. Commun. *13*, 5583. https://doi.org/10.1038/s41467-022-33200-4.

81. Siems, S. (2024). Role of clathrin-mediated endocytosis in myelinating oligodendrocytes. PhD thesis (Georg-August-University Göttingen). https://doi.org/10.53846/goediss-10475.

82. Kondapalli, K.C., Llongueras, J.P., Capilla-González, V., Prasad, H., Hack, A., Smith, C., Guerrero-Cázares, H., Quiñones-Hinojosa, A., and Rao, R. (2015). A leak pathway for luminal protons in endosomes drives oncogenic signalling in glioblastoma. Nat. Commun. *6*, 6289. https://doi.org/10.1038/ncomms7289.

83. Sloane, J.A., and Vartanian, T.K. (2007). Myosin Va Controls Oligodendrocyte Morphogenesis and Myelination. J. Neurosci. *27*, 11366–11375. https://doi.org/10.1523/jneurosci.2326-07.2007.

84. Calliari, A., Farías, J., Puppo, A., Canclini, L., Mercer, J.A., Munroe, D., Sotelo, J.R., and Sotelo-Silveira, J.R. (2014). Myosin Va associates with mRNA in ribonucleoprotein particles present in myelinated peripheral axons and in the central nervous system. Dev. Neurobiol. *74*, 382–396. https://doi.org/10.1002/dneu.22155.

85. Salerno, V.P., Calliari, A., Provance, D.W., Sotelo-Silveira, J.R., Sotelo, J.R., and Mercer, J.A. (2008). Myosin-Va mediates RNA distribution in primary fibroblasts from multiple organs. Cell Motil. Cytoskelet. *65*, 422–433. https://doi.org/10.1002/cm.20272.

86. McCaffrey, M.W., and Lindsay, A.J. (2012). Roles for myosin Va in RNA transport and turnover. Biochem. Soc. Trans. *40*, 1416–1420. https://doi.org/10.1042/bst20120172.

87. Thakurela, S., Garding, A., Jung, R.B., Müller, C., Goebbels, S., White, R., Werner, H.B., and Tiwari, V.K. (2016). The transcriptome of mouse central nervous system myelin. Sci. Rep. *6*, 25828. https://doi.org/10.1038/srep25828.

88. Jahn, O., Siems, S.B., Kusch, K., Hesse, D., Jung, R.B., Liepold, T., Uecker, M., Sun, T., and Werner, H.B. (2020). The CNS Myelin Proteome: Deep Profile and Persistence After Post-mortem Delay. Front. Cell. Neurosci. *14*, 239. https://doi.org/10.3389/fncel.2020.00239.

89. Almeida, R.G., Czopka, T., ffrench-Constant, C., and Lyons, D.A. (2011). Individual axons regulate the myelinating potential of single oligodendrocytes in vivo. Development *138*, 4443–4450. https://doi.org/10.1242/dev.071001.

90. Kirby, B.B., Takada, N., Latimer, A.J., Shin, J., Carney, T.J., Kelsh, R.N., and Appel, B. (2006). In vivo time-lapse imaging shows dynamic oligodendrocyte progenitor behavior during zebrafish development. Nat. Neurosci. *9*, 1506–1511. https://doi.org/10.1038/nn1803.

91. Kemmler, C.L., Moran, H.R., Murray, B.F., Scoresby, A., Klem, J.R., Eckert, R.L., Lepovsky, E., Bertho, S., Nieuwenhuize, S., Burger, S., et al. (2023). Next-generation plasmids for transgenesis in zebrafish and beyond. Development *150*, dev201531. https://doi.org/10.1242/dev.201531.

92. Kawakami, K. (2007). Tol2: a versatile gene transfer vector in vertebrates. Genome Biol. *8*, S7. https://doi.org/10.1186/gb-2007-8-s1-s7.

93. Schindelin, J., Arganda-Carreras, I., Frise, E., Kaynig, V., Longair, M., Pietzsch, T., Preibisch, S., Rueden, C., Saalfeld, S., Schmid, B., et al. (2012). Fiji: an open-source platform for biological-image analysis. Nat. Methods *9*, 676–682. https://doi.org/10.1038/nmeth.2019.

94. Schneider, C.A., Rasband, W.S., and Eliceiri, K.W. (2012). NIH Image to ImageJ: 25 years of image analysis. Nat. Methods *9*, 671–675. https://doi.org/10.1038/nmeth.2089.

95. Liao, Y., Smyth, G.K., and Shi, W. (2019). The R package Rsubread is easier, faster, cheaper and better for alignment and quantification of RNA sequencing reads. Nucleic Acids Res. *47*, e47. https://doi.org/10.1093/nar/gkz114.

96. Love, M.I., Huber, W., and Anders, S. (2014). Moderated estimation of fold change and dispersion for RNA-seq data with DESeq2. Genome Biol. *15*, 550. https://doi.org/10.1186/s13059-014-0550-8.

97. Hao, Y., Stuart, T., Kowalski, M.H., Choudhary, S., Hoffman, P., Hartman, A., Srivastava, A., Molla, G., Madad, S., Fernandez-Granda, C., et al. (2024). Dictionary learning for integrative, multimodal and scalable single-cell analysis. Nat. Biotechnol. *42*, 293–304. https://doi.org/10.1038/s41587-023-01767-y.

98. Yu, G., Wang, L.-G., Han, Y., and He, Q.-Y. (2012). clusterProfiler: an R Package for Comparing Biological Themes Among Gene Clusters. OMICS *16*, 284–287. https://doi.org/10.1089/omi.2011.0118.

99. Shen, M.W., Arbab, M., Hsu, J.Y., Worstell, D., Culbertson, S.J., Krabbe, O., Cassa, C.A., Liu, D.R., Gifford, D.K., and Sherwood, R.I. (2018). Predictable and precise template-free CRISPR editing of pathogenic variants. Nature *563*, 646–651. https://doi.org/10.1038/s41586-018-0686-x.

100. Concordet, J.-P., and Haeussler, M. (2018). CRISPOR: intuitive guide selection for CRISPR/Cas9 genome editing experiments and screens. Nucleic Acids Res. *46*, W242–W245. https://doi.org/10.1093/nar/gky354.

101. Wu, H., Luo, J., Yu, H., Rattner, A., Mo, A., Wang, Y., Smallwood, P.M., Erlanger, B., Wheelan, S.J., and Nathans, J. (2014). Cellular Resolution Maps of X Chromosome Inactivation: Implications for Neural Development, Function, and Disease. Neuron *81*, 103–119. https://doi.org/10.1016/j.neuron.2013.10.051.

102. Lakso, M., Pichel, J.G., Gorman, J.R., Sauer, B., Okamoto, Y., Lee, E., Alt, F.W., and Westphal, H. (1996). Efficient in vivo manipulation of mouse genomic sequences at the zygote stage. Proc. Natl. Acad. Sci. USA *93*, 5860–5865. https://doi.org/10.1073/pnas.93.12.5860.

103. Hruscha, A., and Schmid, B. (2015). Generation of zebrafish models by CRISPR /Cas9 genome editing. In Neuronal Cell Death. Methods in Molecular Biology, *1254*, L. Lossi and A. Merighi, eds. (Humana Press), pp. 341–350. https://doi.org/10.1007/978-1-4939-2152-2_24.

104. Flotho, P., Nomura, S., Kuhn, B., and Strauss, D.J. (2022). Software for non-parametric image registration of 2-photon imaging data. J. Biophotonics *15*, e202100330. https://doi.org/10.1002/jbio.202100330.

105. Reeves, T.M., Phillips, L.L., and Povlishock, J.T. (2005). Myelinated and unmyelinated axons of the corpus callosum differ in vulnerability and

functional recovery following traumatic brain injury. Exp. Neurol. *196*, 126–137. https://doi.org/10.1016/j.expneurol.2005.07.014.

106. Chen, T.-W., Wardill, T.J., Sun, Y., Pulver, S.R., Renninger, S.L., Baohan, A., Schreiter, E.R., Kerr, R.A., Orger, M.B., Jayaraman, V., et al. (2013). Ultrasensitive fluorescent proteins for imaging neuronal activity. Nature *499*, 295–300. https://doi.org/10.1038/nature12354.

107. Weil, M.-T., Ruhwedel, T., Meschkat, M., Sadowski, B., and Möbius, W. (2019). Transmission Electron Microscopy of Oligodendrocytes and Myelin. In Oligodendrocytes. Methods in Molecular Biology, *1936*, D. Lyons and L. Kegel, eds. (Humana Press), pp. 343–375. https://doi.org/10.1007/978-1-4939-9072-6_20.

108. Hua, Y., Laserstein, P., and Helmstaedter, M. (2015). Large-volume en-bloc staining for electron microscopy-based connectomics. Nat. Commun. *6*, 7923. https://doi.org/10.1038/ncomms8923.

109. Cardona, A., Saalfeld, S., Schindelin, J., Arganda-Carreras, I., Preibisch, S., Longair, M., Tomancak, P., Hartenstein, V., and Douglas, R.J. (2012). TrakEM2 Software for Neural Circuit Reconstruction. PLoS One *7*, e38011. https://doi.org/10.1371/journal.pone.0038011.

110. Pitzer, C., Kurpiers, B., and Eltokhi, A. (2021). Gait performance of adolescent mice assessed by the CatWalk XT depends on age, strain and sex and correlates with speed and body weight. Sci. Rep. *11*, 21372. https://doi.org/10.1038/s41598-021-00625-8.

111. Arshadi, C., Günther, U., Eddison, M., Harrington, K.I.S., and Ferreira, T.A. (2021). SNT: a unifying toolbox for quantification of neuronal anatomy. Nat. Methods *18*, 374–377. https://doi.org/10.1038/s41592-021-01105-7.

112. Zhang, F., Tang, X., Tong, A., Wang, B., and Wang, J. (2020). An Automatic Baseline Correction Method Based on the Penalized Least Squares Method. Sensors (Basel) *20*, 2015. https://doi.org/10.3390/s20072015.

113. Stuart, T., Butler, A., Hoffman, P., Hafemeister, C., Papalexi, E., Mauck, W.M., Hao, Y., Stoeckius, M., Smibert, P., and Satija, R. (2019). Comprehensive Integration of Single-Cell Data. Cell *177*, 1888–1902.e21. https://doi.org/10.1016/j.cell.2019.05.031.

114. Satija, R., Farrell, J.A., Gennert, D., Schier, A.F., and Regev, A. (2015). Spatial reconstruction of single-cell gene expression data. Nat. Biotechnol. *33*, 495–502. https://doi.org/10.1038/nbt.3192.

115. Butler, A., Hoffman, P., Smibert, P., Papalexi, E., and Satija, R. (2018). Integrating single-cell transcriptomic data across different conditions, technologies, and species. Nat. Biotechnol. *36*, 411–420. https://doi.org/10.1038/nbt.4096.

116. Zhang, Y., Chen, K., Sloan, S.A., Bennett, M.L., Scholze, A.R., O'Keeffe, S., Phatnani, H.P., Guarnieri, P., Caneda, C., Ruderisch, N., et al. (2014). An RNA-Sequencing Transcriptome and Splicing Database of Glia, Neurons, and Vascular Cells of the Cerebral Cortex. J. Neurosci. *34*, 11929–11947. https://doi.org/10.1523/jneurosci.1860-14.2014.

117. Marques, S., Zeisel, A., Codeluppi, S., van Bruggen, D., Mendanha Falcão, A.M., Xiao, L., Li, H., Häring, M., Hochgerner, H., Romanov, R.A., et al. (2016). Oligodendrocyte heterogeneity in the mouse juvenile and adult central nervous system. Science *352*, 1326–1329. https://doi.org/10.1126/science.aaf6463.

118. Wu, T., Hu, E., Xu, S., Chen, M., Guo, P., Dai, Z., Feng, T., Zhou, L., Tang, W., Zhan, L., et al. (2021). clusterProfiler 4.0: A universal enrichment tool for interpreting omics data. Innovation (Camb) *2*, 100141. https://doi.org/10.1016/j.xinn.2021.100141.

STAR★METHODS

KEY RESOURCES TABLE

REAGENT or RESOURCE	SOURCE	IDENTIFIER
Antibodies		
Rabbit anti-Aspartoacylase (ASPA)	Biozol	Cat# GTX113389-100; RRID: AB_2036283
Rabbit anti-Bcas1	Synaptic Systems	Cat# 445003; RRID: AB_2864793
Mouse anti-Caspr	DSHB	Cat# K65/35-s; RRID: AB_2877274
Guinea pig anti-CNP1	Synaptic Systems	Cat# 355 004; RRID: AB_2620113
Rabbit anti-Cathepsin D	Abcam	Cat# ab75852; RRID: AB_1523267
Goat anti-GFP	Sicgen	Cat# AB0020-200; RRID: AB_2333100
Rabbit anti-GFP	Invitrogen	Cat# A-11122; RRID: AB_221569
Rabbit anti-Iba1	Wako	Cat# 019-19741; RRID: AB_839504
Mouse anti-MBP	BioLegend	Cat# 808401; RRID: AB_2314771
Mouse anti-NeuN	Millipore	Cat# MAB377; RRID: AB_2298772
Rabbit anti-Nav1.6	Alomone labs	Cat# ASC-009; RRID: AB_2040202
Rabbit anti-Olig2	Millipore	Cat# AB9610; RRID: AB_570666
Rabbit anti-Sox9	Abcam	Cat# ab185966; RRID: AB_2728660
Rabbit anti-PDGFRα	Cell Signaling Technology	Cat# 3174; RRID AB_2162345
Donkey anti-Goat Alexa 488	Jackson ImmunoResearch	Cat# 705-546-147; RRID: AB_2340430
Donkey anti-Guinea Pig Alexa 488	Jackson ImmunoResearch	Cat# 706-546-148; RRID: AB_2340473
Donkey anti-Guinea Pig Cy3	Jackson ImmunoResearch	Cat# 706-166-148; RRID: AB_2340461
Donkey anti-Guinea Pig Alexa 647	Jackson ImmunoResearch	Cat# 706-606-148; RRID: AB_2340477
Donkey anti-Mouse Alexa 488	Jackson ImmunoResearch	Cat# 715-546-150; RRID: AB_2340849
Donkey anti-Mouse Cy3	Jackson ImmunoResearch	Cat# 715-166-150; RRID: AB_2340816
Donkey anti-Mouse Alexa 647	Jackson ImmunoResearch	Cat# 715-606-150; RRID: AB_2340865
Donkey anti-Rabbit Alexa 488	Jackson ImmunoResearch	Cat# 711-546-152; RRID: AB_2340619
Donkey anti-Rabbit Cy3	Jackson ImmunoResearch	Cat# 711-166-152; RRID: AB_2313568
Donkey anti-Rabbit Alexa 647	Jackson ImmunoResearch	Cat# 711-605-152; RRID: AB_2492288
Mouse anti-human/mouse/rat, O4-APC	Miltenyi Biotec	Cat# 130-118-978; RRID: AB_2751598
FluoTag-X4 anti-GFP, Abberior Star RED	NanoTag Biotechnologies	Cat# N0304-ABRED; RRID: AB_3678869
Chemicals, peptides, and recombinant proteins		
TPC2-A1-N	MedChemExpress	HY-131614
Yoda1	Sigma-aldrich	Cat# SML1558
Mivacurium chloride	Abcam	Cat# ab143667
Normal Donkey Serum	Histo prime	Cat# END9010
Bovine Serum Albumin (BSA)	Miltenyi Biotec	Cat# 130-091-376
Dulbecco's PBS	Sigma-Aldrich	Cat# D8537
Paraformaldehyde	Sigma-Aldrich	Cat# 158127
Glutaraldehyde EM grade	Sigma-Aldrich	Cat# G5882-50ML
Osmium tetroxide (crystalline) 1g	Science Services	Cat# E19100
Potassium ferrocyanide	Sigma-Aldrich	Cat# P3289-5G
Uranyl acetate (crystalline)	Science Services	Cat# E22400
Sodium cacodylate	Science Services	Cat# E12300-25
Thiocarbohydrazide	Sigma-Aldrich	Cat# 223220-5G
Triton-X-100	Merck Millipore	Cat# 9036-19-5
DMEM/F12 medium	Gibco	Cat# 11330032
SM1	StemCell Technologies	Cat# 05711
N2B	StemCell Technologies	Cat# 07156

(*Continued on next page*)

Continued

REAGENT or RESOURCE	SOURCE	IDENTIFIER
Penn/Strep	ThermoFisher	Cat# 15140
N-Acetyl-Cysteine	Sigma-Aldrich	Cat# A8199
Forskolin	Calbiochem	Cat# 344270
CNTF	PeproTech	Cat# 450-13
PDGF-AA	PeproTech	Cat# 100-13A
NT-3	PeproTech	Cat# 450-03B
Tri-iodo-thyronine T3	Sigma-Aldrich	Cat# T6397
Thyroxine T4	Sigma-Aldrich	Cat# T1775
Poly-D-lysine	Gibco	Cat# A3890401
UltraPure™ Low Melting Point Agarose	ThermoFisher	Cat# 16520100
Liberate Antibody Binding Solution	Polysciences Inc	Cat# A760231
Aqua Polymount	Polysciences Inc	Cat# 18606-20
ProLong Gold Antifade Mountant	Thermo Fisher Scientific	Cat# P10144
Cas9 protein	PNA Bio	Cat# CP02
Critical commercial assays		
RNeasy Micro Kit	Qiagen	Cat# 74004
RNeasy Mini Kit	Qiagen	Cat# 74104
QIAshredder	Qiagen	Cat# 79654
qScript XLT cDNA SuperMix	Quantabio	Cat# 95161-100
SuperScript III First-Strand Synthesis system	ThermoFisher	Cat# 18080051
PowerUp SYBR Green Master Mix	ThermoFisher	Cat# A25742
Adult Brain Dissociation Kit, mouse and rat	Miltenyi Biotec	Cat# 130-107-677
Neural Tissue Dissociation Kit (T)	Miltenyi Biotec	Cat# 130-093-231
Anti-GLAST (ACSA-1) MicroBead kit	Miltenyi Biotec	Cat# 130-095-826
Anti-ACSA-2 MicroBead kit	Miltenyi Biotec	Cat# 130-097-679
Anti-CD11b MicroBeads	Miltenyi Biotec	Cat# 130-097-142
Anti-CD31 MicroBead kit	Miltenyi Biotec	Cat# 130-091-935
Anti-CD140a MicroBead kit	Miltenyi Biotec	Cat# 130-101-547
Anti-O4 MicroBeads	Miltenyi Biotec	Cat# 130-094-543
Evercode WT Mini Kit	Parse Biosciences	N/A
NEBNext Poly(A) mRNA Magnetic Isolation Module	New England Biosciences	Cat# E7490S
NEBNext Ultra-II Directional RNA Library Prep Kit	New England Biosciences	Cat# E7770S
LR CLonase II Plus Enzyme	Thermo Scientific	Cat# 12538120
RNAscope Multiplex Fluorescent v2 Assay	Advanced Cell Diagnostics	Cat# 323100
Mbp probe (Mm-Mbp)	Advanced Cell Diagnostics	Cat# 451491
Experimental models: Organisms/strains		
Mouse: MOGi-Cre	Hövelmeyer N et al.[40]	N/A
Mouse: R26-LSL-tdTomato (B6;129-*Gt(ROSA)26Sortm1(CAG-COP4*E123T*H134R,-tdTomato)Gfng/J*)	The Jackson Laboratory	Cat# 017455; RRID: IMSR_JAX:017455
Mouse: Hprt$^{LSL-GFP}$ GFP (B6;129-Hprt1tm1(CMV-GFP)Nat/J)	The Jackson Laboratory	Cat# 021427; RRID: IMSR_JAX:021427
Mouse: Tmem63a-EYFP	Tsvilovsky et al.[37]	N/A
Mouse: *Tmem63a*$^{-/-}$	Tsvilovsky et al.[37]	N/A
Mouse: Tmem63a floxed	This study	N/A
Zebrafish: mbp:EGFP-CAAX	Almeida et al.[89]	RRID: ZFIN_ZDB-ALT-120103-2
Zebrafish: sox10:mRFP	Kirby et al.[90]	RRID: ZFIN_ZDB-ALT-080321-3
Zebrafish: Tmem63a knockout	This study	N/A

(*Continued on next page*)

Continued

REAGENT or RESOURCE	SOURCE	IDENTIFIER
Oligonucleotides		
gRNA targeting sequence: ACACTAGTCACGTGACATGA	This study	N/A
Primers for genotyping, zebrafish *T63a*$^{-/-}$ mutant forward: AATTGGATCTTTCCTTTTGGTG	This study	N/A
Primers for genotyping, zebrafish *T63a*$^{-/-}$ mutant reverse: GGATCATCCATGTCTGTGAGAA	This study	N/A
Primers for qPCR, zebrafish *T63a*$^{-/-}$ mutant: Tmem63a exon 19/20 forward; CATCGTCCCCTTCGGTCTG	This study	N/A
Primers for qPCR, zebrafish *T63a*$^{-/-}$ mutant: Tmem63a exon 19/20 reverse; CTTGATTGACAGCTCCCAGGT	This study	N/A
Primers for qPCR, zebrafish *T63a*$^{-/-}$ mutant: Tmem63a exon 10/11 forward; GCCCACCCGTCATGTCAC	This study	N/A
Primers for qPCR, zebrafish *T63a*$^{-/-}$ mutant: Tmem63a exon 10/11 reverse; GGTTCTTTTCAGCCCGTTTTCTAT	This study	N/A
Primers for qPCR: Mbp forward; CCTCAGAGGACAGTGATGTGTTT	This study	N/A
Primers for qPCR: Mbp reverse; AGCCGAGGTCCCATTGTT	This study	N/A
Primers for qPCR: Aqp4 forward; TGGAGGATTGGGAGTCACC	This study	N/A
Primers for qPCR: Aqp4 reverse; TGAACACCAACTGGAAAGTGA	This study	N/A
Primers for qPCR: Cspg4 forward; AGGCTGAGGTAAATGCTGGG	This study	N/A
Primers for qPCR: Cspg4 reverse; GCAGGTGGTGAGGACAGTAG	This study	N/A
Primers for qPCR: Cx3cr1 forward; CGTGAGACTGGGTGAGTGAC	This study	N/A
Primers for qPCR: Cx3cr1 reverse; GGACATGGTGAGGTCCTGAG	This study	N/A
Primers for qPCR: Syt1 forward; CTCAACTGGCATTTGTTAGTCAA	This study	N/A
Primers for qPCR: Syt1 reverse; AGACTGCGGATGTTGGTTGT	This study	N/A
Primers for qPCR: Ocln forward; CCGCCAAGGTTCGCTTATCT	This study	N/A
Primers for qPCR: Ocln reverse; CGGACATGGCTGATGTCACT	This study	N/A
Primers for qPCR: Anpep forward; TACTTCACACTCATGTTCGACCG	This study	N/A
Primers for qPCR: Anpep reverse; GAAGTAGAAGAAGAGGGGCGTA	This study	N/A
Primers for qPCR: Myo5a forward; GATCCTCACATCTTCGCAGTAG	This study	N/A
Primers for qPCR: Myo5a reverse; GCCTGACTCTCCACTTACAATG	This study	N/A
Primers for qPCR: Tmem63a forward; CGGTGGCTCTTTGACAAAAC	This study	N/A

(*Continued on next page*)

Continued

REAGENT or RESOURCE	SOURCE	IDENTIFIER
Primers for qPCR: Tmem63a reverse; GGCGATGACGTAGTTCACAA	This study	N/A
Recombinant DNA		
pTol2-UAS:GCaMP6s	Baraban et al.[45]	N/A
p5E-myrf	Jacob Hines lab	N/A
pME-KalTA4	Kemmler et al.[91]	Addgene plasmid: #195965
pDestTol2GC2	Kawakami[92]	N/A
pTol2-myrf:KalTA4	This paper	N/A
Software and algorithms		
Prism v9.5.1	GraphPad	https://www.graphpad.com/
BioRender	BioRender	https://www.biorender.com/
R version 4.4.0 (2024-04-24 ucrt)	R Core Team	https://www.r-project.org/
R Studio v2024.12.0+467	Posit Software, PBC	https://posit.co/download/rstudio-desktop/
ImageJ v1.54m	Schindelin et al.[93]	https://imagej.net/
Imaris 9.9.0	Oxford Instruments	https://imaris.oxinst.com/
Fiji	Schneider et al.[94]	https://imagej.net/
Rsubread 2.20.0	Liao et al.[95]	https://bioconductor.org/packages/release/bioc/html/Rsubread.html
DESeq2 1.44.0	Love et al.[96]	http://www.bioconductor.org/packages/release/bioc/html/DESeq2.html
Seurat 5.1.0	Hao et al.[97]	https://satijalab.org/seurat/
clusterProfiler 4.12.6	Yu et al.[98]	https://bioconductor.org/packages/release/bioc/html/clusterProfiler.html
EnhancedVolcano 1.22.0	GitHub	https://bioconductor.org/packages/release/bioc/html/EnhancedVolcano.html
7500 software v2.0 (7500 Real-time PCR Systems)	Applied Biosystems	https://www.thermofisher.com/
ParseBiosciences Pipeline v1.1.1	Parse Biosciences	https://www.parsebiosciences.com/
CatWalk XT software 10.6.608	Noldus Information Technology	https://www.noldus.com/
InDelphi	Shen et al.[99]	https://indelphi.giffordlab.mit.edu/
CRISPOR	Concordet and Haeussler[100]	https://crispor.gi.ucsc.edu/
TRUESHARP online deconvolution (Version 1.0)	abberior Instruments GmbH	https://app.truesharp.rocks/
MATLAB (R2024b)	Mathworks	https://www.mathworks.com/products/matlab.html
Spike2 software (Version 7)	Cambridge Electronic Design (CED)	https://ced.co.uk/products/spike2
Adobe illustrator (27.9.6)		https://www.adobe.com
CaSCaDe	Agarwal et al.[47]	https://ars.els-cdn.com/content/image/1-s2.0-S0896627316310078-mmc10.pdf

EXPERIMENTAL MODEL DETAILS

Mouse husbandry

Both female and male animals were used in experiments and were randomly allocated to each experimental group. Mice were maintained on a 12 h light/dark cycle at 22 ± 2°C and a humidity level between 50–60%. Food and water were provided ad libitum. All mouse procedures were carried out at the Heidelberg University, Germany, in strict compliance with the German Animal Protection Law (TierSCHG) and as approved by the Governmental Council Karlsruhe, Germany (G-175/21, G-126/20, G189/20).

Transgenic mice

Generation and genotyping of mouse lines used in this study – MOGi-Cre,[40] *R26-LSL-tdTomato* (Jax# 007914), Hprt$^{LSL\text{-}GFP}$ GFP[101] (Jax# 021427), Tmem63-eYFP,[37] Tmem63a null mutant mice[37] have been previously described (see key resources table).

Generation of Tmem63a flox mice

Tmem63a floxed mice were generated by mating *Tmem63a*$^{+/L3F2}$ mice with EIIa-Cre mice,[102] which results in a mosaic deletion of the sequences between the second and third loxP sequence results in a "flox allele" (*Tmem63a*^{flox}). We confirmed that exons 15, 16 and 17 were floxed by PCR (further details see: Figures S5A–S5D).

Zebrafish husbandry

All zebrafish procedures were performed with approval and according to the regulations by the Government of Upper Bavaria, Germany (ROB-55.2-2532.Vet_02-21-172). Animals were housed at the fish facility of the German Centre for Neurodegenerative Diseases (DZNE) in Munich according to the local animal welfare regulations. We used the standard zebrafish strains mbp:EGFP-CAAX[89] and sox10:mRFP[90] and newly generated a stable Tmem63a knockout line on these backgrounds by CRISPR/Cas9-mediated gene editing. Eggs were obtained by natural spawning and raised in E3 medium at 28.5°C. We used larvae at 3, 4 and 10 dpf for imaging studies. For 10 dpf imaging, larvae were kept in tap water with rotifers from 5 dpf on. Sex differentiation occurs after the developmental stages used in this study.

METHOD DETAILS

Generation of Tmem63a knockout zebrafish line

Prediction tools were used to identify a gRNA with high efficiency, frameshift probability and likelihood of inducing a single indel mutation[99,100] Based on these criteria, we selected the gRNA ACACTAGTCACGTGACATGA, targeting exon 10 of the zebrafish *tmem63a* gene. A 20 bp crRNA with the specific target sequence was annealed with tracrRNA (both from IDT) according to the manufacturer's recommendations to obtain crRNA:tracrRNA duplexes, stored at -80°C. For microinjections, crRNA:tracrRNA duplex (1mM) and Cas9 protein (1.25 mg/ml, PNA Bio) were combined in a 1:1 solution to pre-assemble Cas9-gRNA ribonucleoprotein complexes, which were then injected into one-cell stage Tg(mbp:EGFP-caax) embryos.

Genotyping was performed using a standard protocol described in Hruscha and Schmid.[103] In brief, DNA from fin clips or whole larvae was lysed in 1x Tris-EDTA buffer + 10% proteinase K. Amplification was done with primers 5'-AATTGGATCTTTC CTTTTGGTG-3' (forward) and 5'-GGATCATCCATGTCTGTGAGAA-3' (reverse) using GoTaq G2 polymerase (Promega), followed by a restriction digest with NlaIII (NEB). Loss of the restriction site indicated the presence of indel mutations. Fish carrying the highly abundant del5 were identified by Sanger sequencing and inbred to obtain germline transmission in the F1 generation. Homozygous F1 mutants were incrossed to generate larvae for experiments.

pTol2-myrf:KaLTA4 was generated by Gateway cloning, recombining p5E-myrf (kind gift of Jacob Hines), pME-KalTA4[91] and p3E-polyA into pDestTol2CG2[92] with LR Clonase II Plus enzyme (Thermo Fisher Scientific).

Zebrafish RNA isolation and mRNA expression analysis by quantitative PCR

To analyze Tmem63a mRNA expression, 4 dpf larvae were anaesthetized with MS-222 and snap-frozen in liquid nitrogen after harvesting a portion of the tail for genotyping. For RNA isolation, samples were homogenized in RLT Buffer Plus (Qiagen) on ice, using a 200 µl pipet to further mechanically dissociate the tissue and subsequent centrifugation on QIA shredder columns (Qiagen, 79654). RNA was then isolated using the RNeasy Mini kit (Qiagen, 74104) and retrotranscribed with the SuperScript III First-Strand Synthesis system (ThermoFisher, 18080051) following the manufacturer's recommendations. Quantitative PCRs were performed with PowerUp SYBR Green Master Mix (ThermoFisher, A25742), using a LightCycler 480 system (Roche). Relative mRNA expression was calculated using the $\Delta\Delta C_T$ method. For genotyping primers see the key resources table.

Primary oligodendrocyte culture

Brain cortices from 4-5 days old C57BL/6N pups were dissociated into single cell suspensions using Neural Tissue Dissociation Kit (T) (Miltenyi Biotec; 130-093-231) for MACS according to the manufacturer's instructions. In a 2-step MACS protocol, astrocytes were first removed from the cell suspension by anti-GLAST (ACSA-1; Miltenyi Biotec, 130-095-826) microbeads, and OPCs were subsequently isolated using anti-O4 microbeads (Miltenyi Biotec, 130-094-543). These cells were seeded on poly-D-lysine (Gibco, A3890401) coated glass coverslips at an estimated density of 30000 cells/cm^2. Cultures were maintained in OPC medium composed of DMEM/F12 medium (Gibco, 11330032) supplemented with SM1 (StemCell Technologies, 05711), N2B (StemCell Technologies, 07156), Penn/Strep (50 U/mL, ThermoFisher, 15140), N-Acetyl-Cysteine (5 mg/mL, Sigma-Aldrich, A8199), Forskolin (5 mM, Calbiochem, 344270), CNTF (5 mg/mL, PeproTech, 450-13), PDGF-AA (20 ng/mL, PeproTech, 100-13A), and NT-3 (1 ng/mL, PeproTech, 450-03B). One week (6-7 days) after the start of the culture, the cells were transfected with a lentivirus containing jGCaMP8s-mScarlet Ca^{2+} sensor Capres.[35] 2-3 days after the transfection, OPC differentiation into OLs was induced by removing PDGF-AA from the culture media and adding 40 ng/mL tri-iodo-thyronine (T3, Sigma-Aldrich, T6397) and 40 ng/mL thyroxine (T4, Sigma-Aldrich, T1775) to the culture media 48 hours later. Hormones with media were freshly replaced every second day for one week, after which the OLs were used for electrophysiology and Ca^{2+} imaging.

Mechanical stimulation of cultured oligodendrocytes

Mechanical stimulation during Ca^{2+} imaging experiments was done with 2-4 steps of mechanical indentations in 2-3 μm increments with a fire-polished Borosilicate glass pipette (tip diameter 2-3 μm) that was positioned 1-2 μm away from the cell, at an angle of approximately 30° to the surface of the dish and moved with a velocity of 1 μm/ms by a piezo-driven micromanipulator (Nanomotor© MM3A, Kleindiek Nanotechnik). Responder and non-responder cells were identified based on their somatic Ca^{2+} response immediately after stimulation.

Pharmacological manipulations of cultured oligodendrocytes

Pharmacological manipulations of specific receptors and channels were performed by dissolving drugs in artificial cerebrospinal fluid (ACSF) containing (in mM): 119 NaCl, 2.5 KCl, 2.5 $CaCl_2$, 1.3 $MgCl_2$, 1 NaH_2PO_4, 26.2 $NaHCO_3$ and 11 Dextrose (292-298 mOsm/L) or Ca^{2+}-free ACSF containing (in mM): 119 NaCl, 2.5 KCl, 3.8 $MgCl_2$, 1 NaH_2PO_4, 26.2 $NaHCO_3$ and 11 Dextrose (292-298 mOsm/L). These solutions were then oxygenated with carbogen (95% O_2/5% CO_2) and bath-applied to the cultured OLs through a fast perfusion system at the room temperature. The drugs used to perform pharmacological manipulations: Yoda1 (10μM, Tocris, Catalog # 5586) and TPC2-A1-N (10μM, MedChemExpress, Catalog # HY-131614).

Calcium imaging and analysis in cultured oligodendrocytes

Intracellular Ca^{2+} concentration changes were recorded at the room temperature using a custom-built 2-photon microscope (Bergamo II, ThorLabs) fitted with a 20X (1.0NA, XLUMPLFLN, Olympus) or 16X (0.8NA, LWD, Nikon) water-immersion objective, 8 kHz galvo/resonance scanner, piezo drive for fast z-scanning, and two GaAsP PMT detectors. 2-photon excitation for jGCaMP8s and mScarlet at a single wavelength was achieved using a mode-locked Ti:Sapphire pulsed laser (Chameleon Ultra II, Coherent) tuned at 940 nm. Images were acquired at a resolution of 512 x 512 pixels and 12-bit pixel depth. The resulting time series image stacks were pre-processed using FlowRegistration (ImageJ plugin)[104] to eliminate any potential movement artefacts.

Analysis of Ca^{2+} recordings was performed using our machine-learning based algorithm CaSCaDe,[47] which produces an automatic Ca^{2+} microdomain (CaM) map based on the average intensity projection of the image stacks. The CaM map was then further refined by manually segmenting the soma, which was isolated and analyzed separately. Ca^{2+} activity traces were extracted from the CaMs, and Ca^{2+} events with a minimum amplitude of 5 z-score were automatically identified by the CaSCaDe peak detection algorithm.

Pressure-clamp electrophysiology

Mechanically activated currents were recorded in the cell-attach configuration as previously described[38] on primary cultured OLs. Recordings were performed at room temperature using EPC10 amplifier with Patchmaster software (HEKA Elektronik, Lambrecht, Germany Borosilicate patch pipettes were pulled with a P-97 Flaming-Brown puller (Sutter Instrument Company, Novato, CA) and fire-polished (final resistance 1.5 – 4 MΩ). Pipette buffer contained the following (in mM): 130 NaCl, 5 KCl, 1 $MgCl_2$, 1 $CaCl_2$, 10 HEPES, 10 TEA-Cl (pH7.3 with NaOH). The control bath solution contained: 140 KCl, 1 $MgCl_2$, 2 $CaCl_2$, 10 Glucose, 10 HEPES (pH7.4 with KOH). Cells were held at a holding potential of -60 mV. Mechanical stimuli were applied as negative pressure pulses of 1s in cell-attach configuration with the High-Speed Pressure Clamp device (HSPC; ALA Scientific Instruments, Farmingdale, NY) controlled by Patchmaster, using -10mmHg increments and up to -100mmHg. The evoked cell-attached currents were recorded with a sampling frequency of 50 kHz and passed through a 2.9 kHz low-pass filter. Recordings that displayed excessive leak and unstable baseline were not used for analyses. Positive responders to mechanical stimulation were defined as currents differing significantly from the baseline level, responding before -80mmHg and above stimuli and having precise time-locked response to the mechanical stimulus, thus avoiding false positives due to non-specific membrane perturbation induced by strong mechanical stimuli. Current amplitude for a given stimulus was determined as the maximal amplitude over the mechanical stimulus compared to the previous baseline, defined over the last 500 ms before the stimulus. Half-activation pressure (P50) for a given responding cell was determined on normalized currents (to the maximal amplitude of the current cell) fitted with a sigmoid curve $I = 1 / (1 + 10^{(log\ P50 - X)})^{-a}$), with *P50* being the pressure at half-maximum current and the slope. Activation or deactivation kinetics were determined on currents just before or after the pressure stimulus and were fit to the exponential equation $y = K0+K1*exp^{(-(t - t0\ /\ tinact)}$, t_{inact} is the time constant of activation or deactivation (ms) and *KO* and *K1* are constants.

Compound action potential recordings and analysis

Acute brain slices were prepared following previously described protocols.[35] 7-9 weeks old mice were deeply anesthetized with the general inhalation anesthetic isoflurane (1.5% vol/vol isoflurane in a gas mixture of 70% nitrous oxide and 30% O_2; Isofluran Baxter, Baxter Deutschland GmbH, Unterschleißheim, Germany) and killed by decapitation. The brain was rapidly removed and placed in ice-cold (4°C) N-methyl-D-glucamine (NMDG) based cutting solution containing (in mM): 135 NMDG, 1 KCl, 1.2 KH_2PO4, 1.5 $MgCl_2$, 0.5 $CaCl_2$, 10 D-Glucose and 20 Choline Bicarbonate (~310 mOsm/L). 450 μm thick coronal slices were cut using a vibratome (VT 1200S, Leica Microsystems, Nussloch, Germany). Slices containing midline-crossing segments of the corpus callosum (3 to 4 slices per brain) were transferred to a custom-built recording chamber and kept at the interface of humidified carbogen (95% O_2 + 5% CO_2) and continuously exchanged aCSF containing (in mM): 119 NaCl, 2.5 KCl, 2.5 $CaCl_2$, 1.3 $MgCl_2$, 1 NaH_2PO_4, 26.2 $NaHCO_3$ and 11 D-Glucose (292-298 mOsm/L). Both cutting and recording solutions were saturated with carbogen. Slices were

maintained at 34 ± 1°C for recovery for at least 1 h prior to the start of electrophysiological recordings. Electrophysiological recordings were conducted at room temperature (22–23 °C), which is optimal for separation of electrophysiological (compound) responses originating from myelinated and unmyelinated axons.[41,105]

Compound action potentials (CAPs) were evoked by electrical stimulation of CC using a bipolar platinum/iridium electrode (PI2ST30.1A3, MicroProbes for Life Science, USA). Constant-current pulses (200–700 μA, 100 μs duration) were delivered with an Iso-Flex stimulus isolator triggered by a Master-8 VP stimulator (AMPI, Jerusalem, Israel). Recordings were made with glass electrodes containing a silver-chloride wire and back-filled with recording solution. Glass electrodes (tip diameter 2–3 μm; GB150F-8P, Science Products, Hofheim, Germany) were pulled with a horizontal micropipette puller (DMZ Zeitz-Puller, Zeitz-Instruments Vertriebs GmbH, Martinsried, Germany) and positioned in the contralateral hemisphere over CC fibers, approximately 2 mm from the stimulation site. CAPs were amplified 100x with an EXT 10-2F amplifier (npi electronics, Tamm, Germany). Signals were low-pass filtered at 2 kHz and high-pass filtered at 0.3 Hz, digitized at 20 kHz with an analog-to-digital converter (Cambridge Electronic Design (CED) MICRO 1401 mkII, Cambridge, UK) and saved on a computer using Spike2 software (CED, Cambridge, UK) for offline analysis. Stimulation artifacts were trimmed in the represented traces. Input-output curves were generated by recording the amplitudes of myelinated (N1) and unmyelinated (N2) fibers as a function of stimulation intensity. Latency was defined as the time interval between the onset of the stimulation artifact (time zero) and the peak of each negative deflection (N1 and N2) in the evoked response using Spike2 software (CED, Cambridge, UK).

Immunohistochemistry on mouse tissue

Mice were anesthetized with 100 mg/kg (i.p.) Narcorene and perfused transcardially with phosphate-buffered saline (PBS) followed by 4% paraformaldehyde (PFA). After overnight post-fixation with 4% PFA, brains were sectioned into 35 μm thick slices using a vibratome (Leica VT 1000S). Coronal brain sections containing the motor cortex and corpus callosum were permeabilized in permeabilization buffer (0.3% Triton-X-100 in PBS), followed by epitope blocking with blocking buffer (0.3% Triton-X-100 and 5% donkey serum (Histo prime, END9010) in PBS. Sections were incubated with primary antibodies for 1-2 overnights at 4°C, followed by incubation with secondary antibodies for 3 hours at room temperature, and finally washed with PBS. All antibodies were diluted in blocking buffer. Sections were mounted on superFrost Plus slides (Thermo Fisher Scientific, 4951PLUS) using Aqua Polymount (Poly-science Inc, 18606-20) or ProLong Gold Antifade Mountant (Thermo Fisher Scientific, P10144). ASPA immunostaining antigen retrieval was performed at room temperature for 10 min in L.A.B. reagent (Liberate Antibody Binding Solution; Polysciences Inc, A760231).

Epifluorescence and confocal microscopy on fixed tissue

For myelin and cell number quantification on mouse brain, sections were imaged with a Leica DM600B microscope using an HC PL APO 10x/NA 0.4 (Leica) air objective. Fluorescent antibody labelled nodes and internodes were imaged at a resolution of 1024 × 1024 pixels using a Leica SP8 confocal microscope set at the pinhole of 1 Airy Unit (AU), and equipped with 40x (HC PL APO CS2 Water-immersion, Leica) and 63x (HCX PL APO oil immersion, Leica) objectives, respectively. Example images in the figures are presented as maximum intensity projections.

Stimulated Emission Depletion (STED) microscopy

STED microscopy was performed with Abberior Expert Line microscope (Abberior Instruments GmbH, Germany) equipped with pulsed STED depletion lasers at 775 nm and 595 nm and excitation lasers at 355, 405, 485, 580, and 640 nm. Fluorescence emission was detected using avalanche photodiodes (APDs) with the following spectral detection windows: 505–540 nm (Alexa Fluor 488/YFP/eGFP), 600–630 nm (STAR580) and 650–725 nm (STAR Red). STED images were acquired with the 100x/1.4 NA objective at a pixel size of 30 nm and a pinhole size of 80 μm (0.8 Airy Units). Images were processed with the following parameters: number of iterations: 2; PSF size (FWHM px): 2, background size (px): 16, background weight: 0.5 using TRUESHARP online deconvolution (Version 1.0) software by Abberior Instruments.

Single molecule fluorescent in-situ hybridization (smFISH) with immunohistochemistry

Brains from postnatal day 11 (P11) mice were transcardially perfused with 4% paraformaldehyde (PFA) in PBS. Following overnight post-fixation in 4% PFA at 4 °C, brains were cryoprotected in 10%, 20%, and 30% sucrose (in 1× PBS) at 4 °C. Tissue blocks were embedded in optimal cutting temperature compound (OCT, Tissue-Tek). Coronal sections (15 μm) were cut on a cryostat (Leica CM3050S) and mounted on SuperFrost Plus slides (Thermo Fisher Scientific), stored at -80 °C until use. Co-detection of RNA and protein was performed using the RNAscope Multiplex Fluorescent v2 Assay (Advanced Cell Diagnostics, Cat. No. 323100) following the manufacturer's protease-free co-detection protocol for fixed-frozen tissue. A probe targeting mouse Mbp mRNA (Mm-Mbp, Cat. No. 451491) was applied. After completion of the hybridization and amplification steps, sections were immunostained with antibodies against CNP (to label oligodendrocyte processes) and MYO5A (to visualize the RNA transport machinery). Images were acquired on a Leica SP8 confocal laser scanning microscope using a 40X HC PL APO CS2 water-immersion objective. Confocal z-stacks were imported into ImageJ (NIH) for analysis. Oligodendrocyte internodes were identified by CNP immunostaining, and Mbp mRNA fluorescence intensities were quantified along CNP+ internodes using the Measure (M) function in ImageJ.[93,94]

Zebrafish *in vivo* confocal microscopy

3 dpf larvae were incubated in phenylthiourea (PTU) from ~8 hpf onwards to prevent pigmentation. Prior to imaging, larvae were anesthetized with tricaine and laterally mounted in 1.0-1.5% UltraPure™ Low Melting Point Agarose (ThermoFisher, 16520100) on a glass bottom dish (#1.5 cover glass, IBL, 220.110.012). Larvae were excised from the agarose after imaging and lysed to confirm genotypes. Image acquisition was done on a Leica TCS SP8 confocal laser scanning microscope with 8kHz resonant scanner and automated moving stage inside a tempered chamber (28.5°C). We used a 1.1 NA 40x water immersion objective, 488 nm laser and hybrid detector in photon counting mode (4x line accumulation) to acquire images with 8-bit depth. Images were oriented with the anterior to the left, posterior to the right, dorsal to the top and ventral to the bottom. To obtain static images of 3 dpf spinal cords, we acquired tilescans of 6x1 tiles starting at the anterior end of the spinal cord with an image size of 116.4 x 116.4 μm and a pixel size of 93 x 93 nm, covering a total area of ~ 640 μm x 120 μm. Z-stacks covering entire hemi-spinal cords were taken with the pinhole set to 1 AU and a z-step size of 0.5 μm.

To visualize ongoing myelination, we performed in vivo time lapse imaging of 3 dpf spinal cords over 13 to 18 hours, in which we acquired z-stacks with an image size of 82 x 82 μm and pixel size of 160 x 160 nm every 20 min, with a pinhole of 1.2 AU and z-step size of 1 μm. Images were merged using the LAS X software and time lapse acquisitions were additionally registered using the Correct 3D drift plugin with default settings in Fiji. Images were smoothed in Fiji for presentation. Example images in the figures show maximum intensity projections of confocal z-stack.

Calcium imaging in zebrafish

For mosaic expression of GCaMP6s in early myelinating OLs, a mixture of 12.5 ng/μl pTol2-UAS:GCaMP6s[106] (a kind gift of David Lyons) and pTol2-myrf:KalTA4 (12.5 ng/μl each) and 25-50 ng/μl transposase mRNA was injected into one-cell stage *T63a*$^{+/+}$ and *T63*$^{-/-}$ zebrafish embryos with a transgenic sox10:mRFP background. Ca^{2+} imaging was conducted in 3-4 dpf larval zebrafish without prior PTU treatment to avoid interference with Ca^{2+} activity. Larvae were immobilized by treatment with 1.5 mg/ml of the neuromuscular blocking agent mivacurium chloride (Abcam, ab143667), and embedding in 2% agarose. We used a Leica TCS SP8 microscope with the above-described setup and a 0.95 NA 25x water immersion objective, 488 nm laser and hybrid detector in standard mode (6x line average). For Ca^{2+} imaging, we acquired images at 8-bit depth and a resolution of 80-150 nm in x and y and 1.5 μm in z (pinhole at 1.4 AU) every 2.5 s over a total duration of 20 min. To better resolve the morphology of the myelin sheaths for sheath length measurements, we additionally acquired static dual-color z-stacks (myrf:KalTA4; UAS:GCaMP6s and sox10:mRFP) directly prior to and 3-12h after Ca^{2+} imaging. Example time-series images Figure 7 show average intensity projections.

Oligodendrocyte isolation and single-cell library preparation

Oligodendrocyte lineage cells were isolated from cortices of 10-weeks old transgenic HprtLSL-GFP mice where all neural cells expressed nuclear-targeted EGFP. The tissue was dissociated into a single cell suspension using an Adult Brain Dissociation Kit (Miltenyi Biotec,130-107-677) following the manufacturer's instructions. The cells were resuspended in ice-cold 0.5% BSA in DPBS, and incubated with FcR blocking reagent (1:10, Miltenyi Biotec, 130-092-575) for 10 minutes at 4 °C, followed by incubation with a mixture of CD11b MicroBeads (1:10, Miltenyi Biotec, 130-093-636), ACSA-2 MicroBeads (1:10, Miltenyi Biotec,130-097-678) and CD31 MicroBeads (1:10, Miltenyi Biotec, 130-097-418) for 15 minutes at 4 °C. The cells were washed with 0.5% BSA in DPBS. During washing, the magnetic-activated cell sorting (MACS) columns were equilibrated by applying 500 μl of 0.5% BSA in DPBS. The cell suspension was applied to MS columns (Miltenyi Biotec, 130-042-201) and passed through the resin by gravity flow. The columns were washed thrice with 0.5% BSA in DPBS. The eluted CD11b-, ACSA2- and CD31- cells were then incubated with anti-O4-APC antibody (1:50, Miltenyi Biotec, 130-119-155) for 10 minutes at 4 °C, washed with 0.5% BSA in DPBS and Fluorescence-activated cell sorted (FACS) with a BD Aria system (BD Biosciences) to separate GFP+O4+ oligodendrocytes. Sequencing libraries were generated using the Evercode WT Mini Kit (Parse Biosciences) according to the manufacturer's protocol. Samples were sequenced on a NovaSeq6000 SP flow cell (paired end, 100bp) at a sequencing depth of 50000 reads per cell.

Bulk RNA sequencing of oligodendrocytes

Cortices were dissected from 11-days old and 5-weeks-old mice, and processed into single-cell suspensions using the Adult Brain Dissociation Kit (Miltenyi Biotech, 130-107-677), according to the manufacturer's protocol. Astrocytes and OPCs were depleted using ACSA-2 (Miltenyi Biotech, 130-097-679) and CD140a (Miltenyi Biotech, 130-101-547) microbeads, respectively. OLs were subsequently enriched using O4+ microbeads (Miltenyi Biotech, 130-094-543). RNA was extracted from enriched OLs using the RNeasy Mini Kit (Qiagen, 74004), and complementary DNA (cDNA) was synthesized using the qScript XLT cDNA SuperMix (Quantabio, 95161-100). RNA integrity (RIN > 7) was verified using the Bioanalyzer 2100 (Agilent), and RNA amount was quantity with the Qubit 4 Fluorometer (Thermo Fisher Scientific, Q33226). The purity of MACS-isolated OLs was confirmed by real-time PCR using cell-type specific marker genes: Mbp and Mog (OLs), Aqp4 (astrocytes), Cspg4 (OPCs), Cx3cr1 (microglia), Syt1 (neurons), and Ocln and Anpep (endothelial cells). Polyadenylated mRNA was isolated from high-quality RNA samples using the NEBNext Poly(A) mRNA Magnetic Isolation Module (NEB, E7490S). Libraries were prepared using the NEBNext Ultra-II Directional RNA Library Prep Kit (NEB, E7770S). Multiplexed cDNA libraries were sequenced on a NovaSeq6000 (paired end, 100bp) at a depth of 22M reads/sample.

Transmission electron microscopy (TEM)

Sample preparation was performed as previously described.[107] In brief, mice were fixed by transcardial perfusion with 2.5% glutaraldehyde, 4% formaldehyde and 0.5% NaCl in phosphate buffer pH 7.3. After dissection, the tissue was further fixed with the same fixing solution overnight at 4°C. After postfixation with 2% OsO4 in 100 mM phosphate buffer pH 7.3 at 4°C, samples were dehydrated with acetone and embedded in Epon (Serva, Heidelberg, Germany). Ultrathin sections were prepared with a diamond knife (35°, Diatome, Biel, Switzerland) and an FC7 Ultramicrotome (Leica Microsystems, Wetzlar, Germany). For g-ratio analysis, 10 random micrographs covering an area of approx. 440 μm^2 each were taken at a magnification of 5000x using a LEO912 transmission electron microscope (Carl Zeiss Microscopy, Oberkochen, Germany) with an on-axis 2k CCD camera (TRS, Moorenweis, Germany).

Immunoelectron microscopy

Sample preparation was performed as previously described.[107] In brief, for tissue collection, mice were transcardially perfused with 4% formaldehyde and 0.2 % glutaraldehyde in 0.1 M phosphate buffer containing 0.5% NaCl. After tissue dissection, the samples were stored at 4°C in the same fixation solution overnight. Subsequently, vibratome sections of the brains were prepared using a VT1200S (Leica Microsystems, Wetzlar, Germany) and infiltrated overnight with 2.3 M sucrose in 0.1 M phosphate buffer. Pieces of optic nerve were then mounted on aluminium pins for ultramicrotomy and frozen in liquid nitrogen. Ultra-thin cryosections were prepared with a UC6 cryo-ultramicrotome (Leica Microsystems, Wetzlar, Germany) using a 35° cryo-immuno-diamond knife (Diatome, Biel, Switzerland). For immunolabelling, sections were incubated with antibodies directed against GFP (polyclonal, Invitrogen, RRID AB_221569) and carbonic anhydrase II (CAII, Rabbit polyclonal; a kind gift from Said Ghandour). Subsequently with protein A-gold (10 nm and 15 nm) obtained from the Cell Microscopy Center, Department of Cell Biology, University Medical Center Utrecht, The Netherlands. The sections were then analysed using a LEO EM912AB (Carl Zeiss Microscopy, Oberkochen, Germany), and digital micrographs were taken using a 2048x2048 CCD camera (TRS, Moorenweis, Germany).

Scanning electron microscopy

Zebrafish larvae were anaesthetized and a ~3 mm piece of the trunc posterior to the heart was instantly fixed in fixative (2.5% glutaraldehyde, 4% paraformaldehyde, 3.5% mannitol, 2 mM $CaCl_2$ in 0.15 M cacodylate buffer at pH 7.4) in a microwave (BioWave Pelco, with vacuum). The larvae were incubated in fixative at 4°C for one week and washed in 0.15 M cacodylate buffer with 3.5% mannitol. A BioWave microwave was used for further EM processing using a variation of the Hua et al. protocol.[108] The tissue was postfixed in 2% osmium tetroxide (Sciences Services), 2 mM calcium chloride in 0.15 M sodium cacodylate followed by a reducing step in 2.5% potassium hexacyanoferrate (Sigma). After impregnation with thiocarbohydrazide (1% in water, Sigma), the tissue was further contrasted by 2% aqueous osmium. 1% uranylacetate (EMS) was added over night at 4°C and for two hours at room temperature. Samples were dehydrated at increasing ethanol concentrations and embedded in LX112. For SEM imaging, ultrathin sections at 100 nm thickness were generated on a Leica UC7 ultramicrotome and attached to carbon nanotube (CNT) tape strips (Science Services). SEM imaging for the spinal cord samples was performed on a Crossbeam 340 (Zeiss). Images were taken at 4 x 4 nm resolution and analyzed using ImageJ/TrakEM23.[109]

Mouse motor behavioral phenotyping

Balance Beam Test

The balance beam test was conducted twice the same day, with a 1-hour interval between trials. The apparatus consisted of seven beams of varying diameters (32 mm, 25 mm, 20 mm, 15 mm, 12 mm, 8 mm, and 6 mm), each 50 cm in length and 20 cm in height. Mice were first placed on the widest (32 mm) beam and progressively tested on narrower beams. A trial was scored as successful and given a score of one if the mouse crossed the beam without falling or remained on the beam for 10 seconds. The balance beam score was calculated as the total number of successful trials, with a maximum score of 8 for successfully completing all beams.

Rotarod Test

Motor coordination and performance were assessed using an accelerating Rotarod apparatus (Ugo Basile, Gemonio, Italy, model 47600). Mice were initially trained over two consecutive days with three trials per day. The experimental session consisted of three trials conducted on the same day, with a 10-15-minute recovery period between trials. During each trial, the rod accelerated from 4 to 40 rpm over 8 minutes. The time each mouse remained on the rod before falling (latency to fall) was recorded and averaged across the three trials.

Catwalk Test

Gait analysis was performed using the CatWalk XT system (Noldus Information Technology, Netherlands).[110] Mice were habituated to the system one day before the experiment. The system consists of an enclosed tunnel with a glass walkway illuminated by green fluorescent light and a high-speed camera positioned underneath the walkway. The trial is considered successful and compliant if the mice run through the walkway in under 12 seconds, and a run maximum variation under 60%. For each mouse, 3 trails are taken for the analysis. The automated footprint recognition feature of CatWalk XT software (version 10.6.608) was used to analyse the runs, and all data were manually reviewed to correct for misclassified footprints or exclude unwanted contacts (e.g., nose, abdomen, or tail). The following parameters were evaluated: swing speed, stride length, base of support, and print areas of the front and hind paws. Data were exported and analysed using GraphPad Prism.

QUANTIFICATION AND STATISTICAL ANALYSIS

Cell number and myelin geometry quantification

Analysis of mouse brain immunohistochemistry was performed using ImageJ software (NIH). For quantification of OL number in mice, ASPA+ cells were manually counted using the ImageJ Cell Counter plugin. Myelin basic protein (MBP) intensities were measured after background subtraction using a rolling ball radius of 50 pixels, and intensity values were recorded through the ROI Manager measurement tool. Internode lengths were calculated in 3D confocal image stacks using the Simple Neurite Tracer plugin in ImageJ (Arshadi et al.).[111] On the max-intensity projected confocal z-stacks, nodes of Ranvier were located by Nav1.6 staining, and were selected for quantification when flanked by Caspr+ paranodes. A line was drawn through Caspr+ paranodes to measure the staining intensity changes, and the full-width half-maximum (FWHM) of pixel intensity was calculated to determine node and paranode lengths. The FWHM macro was taken from GitHub (Olivier Burri from EPFL, Zurich). For all quantifications two consecutive coronal brain sections for each mouse was used.

Myelin g-ratio analysis

For g-ratio quantifications on electron micrographs, axons were randomly selected and the diameters of myelinated axons and corresponding g-ratios were measured using ImageJ software. Electron micrographs were calibrated by setting the scale based on the provided scale bar. Axon and myelinated fiber boundaries were manually marked using the ROI tool, with areas added to the ROI manager after each selection. The areas of the axon, inner membrane, and outer membrane were measured. Axon diameter (D_A) and the diameter of the myelinated fiber including myelin (D_{A+M}), were calculated from the measured area, and the ratio estimated as D_A/D_{A+M}. Myelin area was calculated by subtracting the cross-sectional area of the myelinated fiber from the area of the axon. Data were analyzed and plotted using GraphPad Prism.

Analysis of myelin sheath growth and dynamics

Quantifications of zebrafish spinal cord imaging were done in Imaris 9.9.0 and Fiji 1.53. To quantify white matter volume, we reconstructed surfaces of 3 dpf mbp:EGFP-CAAX-positive hemi-spinal cords from tilescans using Imaris. Surfaces were smoothed with a 0.1 μm-wide Gaussian filter and manual thresholding was applied such that the shape of the white matter was fit most accurately. We used the split touching objects function with a seed points diameter of 1.0 μm to enable manual removal of any surface beyond the hemi-spinal cord. Quantifications represent the total volume of ventral and dorsal white matter reconstructions.

Stabilized and retracting internodes per OL were quantified from 13-to-18-hour in vivo time lapse acquisitions using Imaris. Stabilized internodes represent the total number of internodes minus the number of internodes that were retracting throughout the acquisition. Retracting internodes were defined by the complete collapse of >3 μm long internodes into ~ 1 μm large retraction bulb that either remained or were completely retracted in to the OL cell body during the rest of the acquisition. Retraction bulbs that were visible at the beginning of an acquisition and later removed were as well counted as retractions.

Internode growth was quantified from 13-to-18-hour in vivo time lapse acquisitions. The length of individual internodes at first appearance and every 4th or 5th subsequent time frame was measured in Fiji. Internode growth was calculated as the difference between maximum and initial length, divided by the respective time interval.

Ensheathed cell bodies presented as cap-like, mbp:EGFP-CAAX-positive structures connected to OL cell bodies[72] and were identified by inspecting tilescans spinal cords in 3D using Imaris. Quantifications include the percentage of fish that showed cell body ensheathment and the total number of ensheathed cell bodies in these acquisitions.

Analysis of Ca^{2+} imaging in zebrafish

Region of Interests (ROIs) that exhibited calcium activity were detected using the average projection as previously described.[47] Ca^{2+} traces were extracted and detrended[112] to eliminate any possible drift movement. Ca^{2+} signals were automatically detected using CaSCaDe algorithm. Ca^{2+} signals that have an amplitude of 4z-score and a duration of 4 frames were considered. Ca^{2+} signals were subsequently classified using previously trained SVM.[47] To eliminate any false positive Ca^{2+} signals, all Ca^{2+} events that had passed the previous criteria were manually evaluated on the basis of the image stacks and the corresponding traces, using a custom-made Graphical User Interface (GUI). This enabled us to identify and dismiss motion artefacts. For better representation in this paper, we substituted individual frames with motion artefacts by the immediately preceding frame in the movie and corrected the traces accordingly. To account for the mosaic expression of the GCaMP6s sensor, the number of Ca^{2+} events in each acquisition was normalized by the area in average projections. For the correlation of Ca^{2+} events and myelin sheath growth, we determined positive and negative sheath growth before-and-after dual color acquisitions in sheaths displaying Ca^{2+} events as well as a random selection of those sheaths, in which no events were detected during the acquisition time.

Sc-RNA sequencing bioinformatic analysis

Sequencing reads were demultiplexed using ParseBiosciences Pipeline v1.1.1 (Parse Biosciences) and aligned to the mouse genome GRCm39. The 'split-pipe' pipeline was used to generate a cell-by-gene count matrix, which was further processed with Seurat 5.1.0.[97,113–115] Cells which fulfilled the following quality control metrics were selected for further analysis: between 100 to 7000 genes per cell, <5% mitochondrial gene expression and between 1422 to 50,000 total RNA counts per cell. Normalization,

variable feature selection and scaling were performed using default Seurat parameters. Principal component analysis was modified from the default pipeline by describing the parameter *features* with a list of 627 oligodendrocyte lineage genes obtained from Zhang et al.[116] Genes in the database were identified as oligodendrocyte lineage genes if they had an expression level >100 FPKM in any of the oligodendrocyte stages. This was followed by cell clustering and resulting cell clusters were visualized using uniform manifold approximation and projection (UMAP). OL lineage cell clustering was performed with *FindAllMarkers* function from Seurat and further classified based on cell-type specific markers identified by others.[117]

Bulk RNA-seq bioinformatic analysis

Demultiplexed reads were mapped to the mouse genome (GRCm39) and counted using Rsubread.[95] Count matrices were further analysed with DESeq2 (v1.44.0)[96] for differential gene expression analysis. Significant differentially expressed genes (DEGs) were defined by a p-adjusted value of <0.01. To increase the specificity of our bulk RNA-seq analysis and a consider gene to be highly expressed in OLs, the RNA-seq data from[116] was used for further filtering DEGs fulfilling the following criteria: (1) expression in either newly formed OLs or mature OLs was more than 10% of FPKM value in microglia, and (2) expression level >10 FPKM in either newly formed OLs or mature OLs. Filtered DEGs were evaluated for affected Gene Ontology Biological Processes using ClusterProfiler 4.12.6[98,118]

Statistical Analysis

All statistical analyses were performed using the software GraphPad Prism (v8.0). D'Agostino–Pearson method was used to test if the data are normally distributed. For normal distributed datasets, comparisons between groups were conducted using unpaired two-tailed t-test (when datasets had similar standard deviation) or unpaired two-tailed t-test with Welch's correction (when were standard deviation not same). If the datasets were not normally distributed, then non-parametric Mann-Whitney U test was used to compare statistical significance between the groups. Kolmogorov–Smirnov (KS) test was used to compare the statistical significance between frequency distributions of two datasets. If multiple datasets were included in the analysis, a one-way ANOVA or mixed effect analysis test (to account for missing values) was used. Statistical significance thresholds and exact p-values are reported in the figure legends. The statistical tests used for each comparison (and their significance level) are indicated in the figure legends. Data are described in the results as Mean ± SD and presented in figures as Mean ± SEM, if not stated otherwise. $p < 0.05$ was considered significant. Violin plots show the data distribution with median (middle line; blue/red), and 25% (lower line; black) and 75% (top line; black) interquartile ranges. N represents the number of animals and n the number of cells (electrophysiology and Ca^{2+} imaging) or brains slices (histology).

Data presentation

All the main and supplementary figure panels were assembled in Adobe Illustrator 2024, and cartoons were modified from graphical elements available at BioRender.